UNIVERSITY OF CALIFORNIA

Los Angeles

Topics in High Intensity Laser Plasma Interaction

A dissertation submitted in partial satisfaction of the requirements for the degree

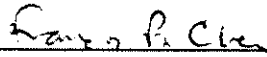Doctor of Philosophy in Electrical Engineering
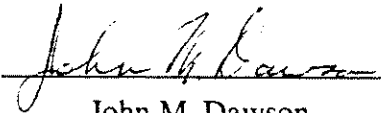
by

Wim Pieter Leemans

1991

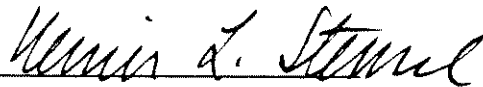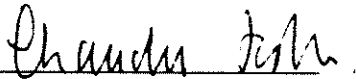The dissertation of Wim Pieter Leemans is approved.

Francis F. Chen

Neville C. Luhmann, Jr.

John M. Dawson

Reiner L. Stenzel

Chan Joshi, Committee Chair

University of California, Los Angeles

1991

Dedication

To Frans and Betty, my parents, and Clémence, my grandmother.

For Annette.

Contents

List of Figures

viii

F. F. Chen, C. E. Clayton, C. B. Darrow, J. M. Dawson, C. Joshi, T. Katsouleas, W. Leemans, K. Marsh, W. Mori, J. Su, D. Umstadter, S. Wilks, 'Particle Acceleration by Plasma Waves', Proceedings of the International Conference on Plasma Physics, Kiev, USSR, pp. 797-801, April, 1987.

C. Joshi, C. E. Clayton, K. Marsh, R. Williams, W. Leemans, 'Experimental Work at UCLA on the Plasma Beat Wave Accelerator', Text of Invited Talk, Proceedings of Workshop on New Developments in Particle Acceleration Techniques, Orsay, France, pp. 1-10, July 1987.

C. Joshi, C. E. Clayton, K. Marsh., W. Leemans, R. Williams, M. T. Shu, 'Test Particle Injection in Relativistic Plasma Waves Excited by Two Co-Propagating Laser Beams', Proceedings of SPIE's Symposium on O-E LASE '88, Los Angeles, California, 6 pages, January 10-17, 1988.

W. P. Leemans, C. Joshi, C. E. Clayton ' Detection of Trapped Magnetic Fields in a θ-Pinch Plasma Using a Relativistic Electron Beam', Rev. Scientific Instruments, 59, p 1641, August, 1988

C. E. Clayton, C. Joshi, W. P. Leemans, K. A. Marsh, M. T. Shu, R. L. Williams, 'Beat Wave Acceleration Experiments', Proceedings of the 1988 Linear Accelerator Conference, Williamsburg, Virginia, October 2-7, 1988

C. E. Clayton, C. Joshi, W. P. Leemans, K. A. Marsh, M. T. Shu, R. L. Williams, 'Beat Wave Development Work', Advanced Accelerator Concepts AIP Conf. Proceedings, No. 193, pp. 37-49, ed. C. Joshi, AIP, New-York, 1989

C. Joshi, C. E. Clayton, W. P. Leemans, K. A. Marsh, M. T. Shu, R. L. Williams, 'Beat Wave Acceleration Experiments at UCLA', Proceedings of the 1989 IEEE Particle Accelerator Conference, Chicago, IL, March 20-23, 1989

W. P. Leemans, C. Joshi, 'On the Eulerian Analysis of Large Amplitude Relativistic Plasma Waves, 'Proceedings of the Topical Conference on 'Relativistic and Non-Linear Effects in Plasma", San Diego, CA, 13 pages, February 5-8, 1990.

W. P. Leemans, C. E. Clayton, K. A. Marsh, A. Dyson and C. Joshi, 'Suitability of Tunneling Ionization Produced Plasma for the Plasma Beat Wave Accelerator', Proceedings of the 1991 IEEE Particle Accelerator Conference, San Francisco, May 20-23, 1991

W. P. Leemans, W. B. Mori, J. M. Wallace, 'PIC-code simulation of Ionization Induced Refraction in a Tunneling Ionization Produced Plasma', Proceedings of the CECAM Workshop on Interaction and Transport in Laser-Plasmas, September 17-28, 1990 Orsay, France.

W. P. Leemans, C. E. Clayton, K. A. Marsh, C. Joshi, 'Stimulated Compton Scattering from Pre-formed Underdense Plasmas', accepted for publication in Physical Review Letters.

W. P. Leemans, C. E. Clayton, K. A. Marsh, W. B. Mori, C. Joshi and A. Dyson, ' Plasma Physics Aspects of Tunnel-Ionized Gases', submitted to Physical Review Letters

W. P. Leemans, W. B. Mori, C. E. Clayton, K. A. Marsh, C. Joshi, J. M. Wallace, 'Experiments and Simulations of Tunnel-Ionized Plasmas', Phys. Fluids, in preparation

W. P. Leemans, C. Joshi, C. E. Clayton and W. B. Mori, 'Non-linear Dynamics of Relativistic Electron Plasma Waves Excited through Collinear Optical Mixing', Phys. Rev. A, in preparation

ABSTRACT OF THE DISSERTATION

Topics in High Intensity Laser Plasma Interaction

by

Wim Pieter Leemans

Doctor of Philosophy in Electrical Engineering

University of California, Los Angeles, 1991

Professor Chan Joshi, Chair

The interaction of high intensity laser pulses with pre-formed and laser-produced plasmas is studied. Through experiments and simulations we have investigated stimulated Compton scattering in pre-formed plasmas and the plasma physics aspects of tunnel-ionized gases. A theoretical study is presented on the non-linear dynamics of relativistic plasma waves driven by colinear optical mixing.

The electron density-fluctuation spectra induced by stimulated Compton scattering have been directly observed for the first time. A CO_2 laser was focused into pre-formed plasmas with densities n_e varied from 0.4—6×10^{16} cm^3. The fluctuations corresponding to backscatter were probed using Thomson scattering. At low n_e, the scattered spectra peak at a frequency shift $\Delta\omega \approx kv_e$ and appears to be in a linear regime. At the highest n_e, a nonlinear saturation of the SCS instability is observed due to a self-induced perturbation of the electron distribution function.

Tunnel-ionized plasmas have been studied through experiments and particle simulations. Experimentally, qualitative evidence for plasma temperature control by varying the laser polarization was obtained by the measurement of stimulated Compton

scattering fluctuation spectra and X-ray emission from such plasmas. A higher parallel temperature than expected from the single-particle tunneling model was observed. Simulations indicate that stochastic heating and the Weibel instability play an important role in plasma heating in all directions and isotropization.

The non-linear dynamics associated with beatwave ($\Delta\omega$, Δk) excited long wavelength plasma waves in the presence of strong, short wavelength density ripple have been examined, using the relativistic Lagrangean oscillator model. This model shows period doubling that roughly follows Feigenbaum scaling, and a transition to chaos. However, wavebreaking is found to occur after the first bifurcation, thereby limiting the applicability of the Lagrangean model. It is found that the origin of this bifurcation is linked to the stability of an equivalent Mathieu equation to 1/2 subharmonic resonances. Finally, a PIC-code simulation shows spatial wavenumber peaks displaced $\Delta k/2$ on both sides of the driver frequencies, giving support to the idea that the bifurcation behaviour may be experimentally observable.

Chapter 1

Introduction

Although the interaction of lasers with matter has been studied since the discovery of the laser, the recent availability of extremely high laser intensities has made it possible to study many new phenomena in this area of physics. In this dissertation we will study three different topics in the interaction of a very high intensity CO_2-laser (peak intensity around 5×10^{14} W/cm^2) with plasmas. We begin with an experimental study of the stimulated Compton scattering instability (Drake et al. 1974, Litvak & Trakhtengerts 1971, Lin & Dawson 1975, Albritton 1975) that can be excited when such a laser interacts with a preformed underdense plasma. Next we investigate the plasma physics aspects of the tunneling ionization (Keldysh 1965, Landau & Lifshitz 1967) of gaseous targets. Finally we present a theoretical study of a laser-plasma based non-linear system that offers the possibility of observing a classical route to chaos (Feigenbaum 1978).

When a high intensity laser interacts with a pre-formed plasma many non-linear processes can take place. One class of such processes involving wave-wave interactions is called the parametric instabilities. The stimulated Raman scattering instability (SRS) and the stimulated Brillouin scattering instability (SBS) in a plasma were predicted in the early 70's (Drake et al. 1974, Forslund et al. 1975) and had been observed experimentally and studied in detail by the middle of the 80's (Bobin et al. 1973, Watt et al. 1978, Walsh et al. 1984). Although stimulated Compton scattering (SCS) had been predicted in the early theoretical work, the fact alone that the instability is heavily damped can explain the lack of early experimental observation of this instability. It was

only recently (Drake et al. 1990) that the first observation of SCS was reported. This is because through progress in laser performance and a continued increase in sensitivity of the diagnostics, SCS has become experimentally observable. However, the detailed characteristics and evolution of the instability were not studied. Using Thomson scattering of a probe beam as a diagnostic we were able to directly measure for the first time the frequency spectrum of the density fluctuations driven by SCS (Leemans et al. 1991) in a pre-formed plasma. By time resolving the spectra, a linear convective saturation was observed for very low density plasmas. At high densities a non-linear saturation was observed and attributed to a self-induced modification of the electron distribution function. Fitting the experimental spectra with the theoretically predicted spectra, we obtained a local estimate for the plasma temperature and density.

Another consequence of the continued increase in available laser intensity of short pulse lasers is the possibility of creating a dense plasma through tunneling ionization (Keldysh 1965, Landau & Lifshitz 1978). For a high intensity laser the associated electric fields can become on the order of the atomic field which binds an electron to the nucleus, allowing the laser to ionize the atom. In principle this optically induced ionization must be modelled taking into account the quantum nature of the atom and the time variation of fields. According to Keldysh's theory however, in the limit where the Keldysh parameter $\kappa = \sqrt{\dfrac{E_{ion}}{\Phi_p}} \ll 1$, one can model the ionization as a process in which the electron tunnels through the suppressed Coulomb barrier of the nucleus. Here E_{ion} is the ionization potential and Φ_p the ponderomotive potential associated with the laser fields. The probability of tunneling through this suppressed barrier becomes significant when the electric field of the laser normalized to the atomic unit of the electric field is larger than 0.01. Once the electron is free, it is assumed to

start at rest and its subsequent motion can be determined by solving the equation of motion in the presence of plane wave electromagnetic fields (Landau & Lifshitz 1962, Kaw & Kulsrud 1973, Corkum et al. 1989). In the plane wave limit, conservation of the canonical momentum requires that the velocity is composed of the usual quiver velocity v_{osc} in the laser field and a drift velocity. The magnitude and direction of the drift velocity is dependent on the polarization of the ionizing laser, which suggests that plasmas with negligible longitudinal temperature $T_{\parallel}$ and controllable $T_{\perp}$ can be produced (Corkum et al. 1989, Burnett & Enright 1990).

In a recent experiment, Corkum et al. have shown that in the single particle regime and long wavelength (10.6 μm laser) regime the above description is indeed valid (Corkum et al. 1989). Although "tunneling ionization" of single atoms has been studied with both 10 μm (Corkum et al. 1989, Yergeau et al. 1987) and 1 μm laser pulses (Perry et al. 1988, l'Huillier et al. 1983), most of the work on tunneling ionization of gases has been conducted in a very low pressure gas, i.e. in the single particle regime. No detailed study of macroscopic plasmas produced using this mechanism has been made. These plasmas may be unique because the laser intensity profile I($\underline{r}$,t) and polarization could be used to determine the initial parallel and perpendicular temperature ($T_{\parallel}$,$T_{\perp}$) of the electrons, the density n_e and the ionization state Z. Such plasmas have applications in the areas of recombination X-ray lasers (Burnett & Enright 1989, Amendt et al. 1991) and various collective accelerator schemes (Tajima & Dawson 1979, Joshi et al. 1984, Leemans et al. 1991b). Furthermore, the possibility of tailoring the initial 3-D distribution functions may allow the study of basic kinetic and parametric instability theory issues in plasma physics.

For an X-ray recombination laser, plasmas need to be produced with densities n_e up to 10^{20} cm^{-3} and temperatures below 20 eV. In plasma based accelerator schemes it is desirable to have long regions of homogeneous plasma at fairly high densities (10^{16} -

10^{18} cm^{-3}). It is our goal to check the validity of extrapolating the predictions of the tunneling ionization model, from a single particle to a space-charge dominated plasma regime, and to address the plasma physics aspects of tunneling ionization of gases.

Our experimental work shows that in the "plasma regime" the longitudinal temperatures are higher than those expected from the single particle tunneling model and that ionization induced refraction clamps the density to $n < 10^{-3}$ n_c. Here n_c is the critical density. Simulations indicate that stochastic heating (Forslund et al. 1985, Bardsley et al. 1989, Mendonça 1985) and the Weibel instability (Weibel 1959) play a crucial role in plasma heating and isotropization. To analyze the effect of a time varying density and/or temperature on SRS and SCS, we have used an approach similar to the one used by Rosenbluth (Rosenbluth 1972) for inhomogeneous plasmas, to recalculate the growth rate of these instabilities in a time dependent plasma.

As a third topic in the interaction of high intensity lasers with plasmas we have studied the non-linear dynamics of a plasma based driven oscillator system. The behavior of driven non-linear oscillators has received much interest in the last decade and many different physical systems have been identified exhibiting such phenomena as bistability leading to hysteresis loops, and the occurrence of subharmonics followed by a transition to chaos. The behavior of driven relativistic large amplitude electron plasma waves can indeed be described by model equations essentially reducible to a non-linear oscillator equation. Such a plasma wave can be resonantly excited by colinear optical mixing (Rosenbluth & Liu 1972).

We have studied the nonlinear dynamics associated with beatwave ($\Delta\omega$, Δk) excited long wavelength plasma waves ($\Delta k \approx \omega_p/c$), in the presence of a strong ($\delta n/n$ - 0.15 to 0.75), short wavelength density ripple (k_i - (5 to 130) Δk). The equation describing the plasma wave generation is the relativistic Lagrangean oscillator model

(Tang et al. 1985, Horton & Tajima 1985). The goal is to determine the experimental conditions necessary to observe the different non-linear phenomena. Results are presented which show period doubling roughly following Feigenbaum scaling (Feigenbaum 1978), and a transition to chaos, characterized by a strange attractor resembling a Duffing oscillator strange attractor. However, wavebreaking occurs before the second bifurcation, thereby limiting the applicability of the Lagrangean oscillator. To understand the origin of the first bifurcation we have approximated the Lagrangean oscillator equation as a driven Mathieu equation and carried out a perturbation analysis (Szemplinska-Stupnicka & Bajkowski 1986). It is found that the origin of this period doubling is linked to the stability of the Mathieu equation 1/2 subharmonic resonances. Finally, a PIC-code simulation shows spatial wavenumber peaks displaced $\Delta k/2$ on both sides of the driver frequencies, giving support to the idea that the bifurcation behavior observed in this simple model may be experimentally observable.

Chapter 2

Stimulated Compton Scattering from Pre-formed Underdense Plasmas

2.1 Introduction

The induced scattering of electromagnetic waves by resonant electrons in a plasma, known as stimulated Compton scattering (SCS) (Drake et al. 1974, Litvak & Trakhtengerts 1971, Lin & Dawson 1975, Albritton 1975) is a problem of fundamental importance in plasma physics and has applications in laser fusion, laser driven accelerators (Joshi et al. 1984), free-electron lasers and tunnel ionization of gases. Historically, SCS has been of interest as a plasma heating mechanism for low density plasmas where other mechanisms such as inverse bremsstrahlung may be ineffective. The spectrum of SCS induced fluctuations can provide both density and temperature information about the plasma. In this chapter we discuss the first direct observation of the the electron density fluctuation spectra induced by SCS. We show that at low densities this kinetic instability stays in the linear convective regime. However, as the density is increased a non-linear saturation is seen to occur.

2.2 Stimulated Compton Scattering

The SCS instability (off electrons) is the low-density or high-temperature—or large $k\lambda_{De}$—limit of stimulated Raman scattering (SRS) (Drake et al. 1974). Here k is the wavenumber of the density fluctuation responsible for the scattered light, $\lambda_{De} = [(KT_e)/(4\pi n_e e^2)]^{1/2}$ is the plasma Debye length, KT_e is the electron temperature and n_e is the electron density. In the SRS instability, the pump electromagnetic wave, with wavevector $\mathbf{k_0}$ and frequency ω_0, scatters off an instability-generated electron plasma wave, which satisfies the Bohm-Gross dispersion relation

$$\Delta\omega^2 = \omega_p^2 + \frac{3}{2}k^2 v_{th}^2 \tag{2.1}$$

In the SCS case, the electron plasma wave is heavily Landau damped and the pump and scattered light waves interact directly with the resonant thermal plasma electrons rather than through a collective mode of the plasma. Another consequence of the plasma mode being heavily damped is the experimental inaccessibility of this instability. One needs a very strong pump and sensitive diagnostics to observe significant levels of SCS density fluctuations. This alone explains the lack of experimental data on the SCS instability. The only previous experimental observation was by Drake et al. (Drake et al. 1990). In their experiment exploding foil plasmas were used. The Compton instability was studied by monitoring a *single* wavelength of the scattered light close enough to the pump-laser wavelength to ensure that the radiation was emitted by a low density plasma (high $k\lambda_{De}$). This is in contrast to the experiment reported here where it is precisely the details of the scattered *spectrum* that allow us to draw conclusions regarding the physics of the interaction. In this experiment an intense CO_2 laser drives SCS in a low density, pre-formed plasma. The density fluctuations are probed using Thomson scattering of a visible probe laser beam.

In a finite length plasma, Compton scattering can be described as the convective amplification, by the Compton instability, of some noise-level spectrum. The noise spectrum is taken to be thermal Thomson scattering (Sheffield 1975) off the pre-formed plasma

$$P_N(\omega, t{=}0) = C\, n_e \left\{ \left| 1 - \frac{\chi_e}{\varepsilon} \right|^2 f_e\left(\frac{\omega}{k}\right) + \left| \frac{\chi_e}{\varepsilon} \right|^2 f_i\left(\frac{\omega}{k}\right) \right\}, \tag{2.2}$$

where ω is the frequency shift of the scattered light, $\varepsilon = (1 + \chi_e)$, f_e (f_i) is the electron (ion) velocity distribution function and C is a constant dependent upon geometrical factors. The spatial growth rate $\kappa(\Delta\omega, k\lambda_{De})$ for backscattering modes with $\mathbf{k} \approx 2\mathbf{k_0}$ is given by (Drake et al. 1974)

$$\kappa(\Delta\omega, k\lambda_{De}) = 2(v_0/c)^2\, \frac{\omega_0}{c}\, \mathrm{Im} \frac{\chi_e(\Delta\omega, k\lambda_{De})}{1 + \chi_e(\Delta\omega, k\lambda_{De})} \tag{2.3}$$

where v_0/c is the normalized electron quiver velocity in the electric field of the pump and $\chi_e(\Delta\omega, k\lambda_{De})$ is the usual electron susceptibility. Equation (2.3) is valid away from the strongly driven regime which for our densities and laser intensities is satisfied (Drake et al. 1974, Forslund et al. 1975). Also, since the SCS fluctuations propagate in a direction normal to the incident laser electric field, i.e. $\mathbf{k} \cdot v_0 = 0$, the expression for $\chi_e(\Delta\omega, k\lambda_{De})$ is thought not to be affected for the case where $v_0 > v_e$, where $v_e = (KT_e/m)^{1/2}$ is the electron thermal velocity (Bernard et al. 1989). However, this issue clearly needs further theoretical attention. The scattered CO_2 power $P_S(\Delta\omega, L)$ is just $P_S(\Delta\omega, L) = P_N \exp(\kappa\, L)$ where P_N is the noise spectrum, taken to be due to thermal Thomson scattering off the pre-formed plasma (Sheffield 1975) and L is the length of the convective amplifier. Since the Thomson scattering probe measures the density fluctuations associated with the CO_2 laser backscatter at one point in space z', the spectrum is then of the form

$$P_{TS}(\Delta\omega, t) = A\ P_N(\Delta\omega, k\lambda_{De}, t{=}0)\ \exp[\kappa(\Delta\omega, k\lambda_{De})\ c\ t]\ \text{for } t < T \qquad (2.4a)$$

$$= A\ P_N(\Delta\omega, k\lambda_{De}, t{=}0)\ \exp[\kappa(\Delta\omega, k\lambda_{De})\ cT\ ]\ \text{for } t > T \qquad (2.4b)$$

where we have assumed the group velocity of the light wave to be c for the underdense plasmas, T is the transit time of the scattered wave to the point z'and A is a fitting parameter.

As can be seen in Fig.(2.1), the effect of increasing $k\lambda_{De}$ beyond about 0.3 in Eqs.(2.4a) and (2.4b) is to significantly broaden the range of frequency shifts $\Delta\omega$ which have significant growth, leading to scattered spectra with widths becoming on the order of the maximum shift.
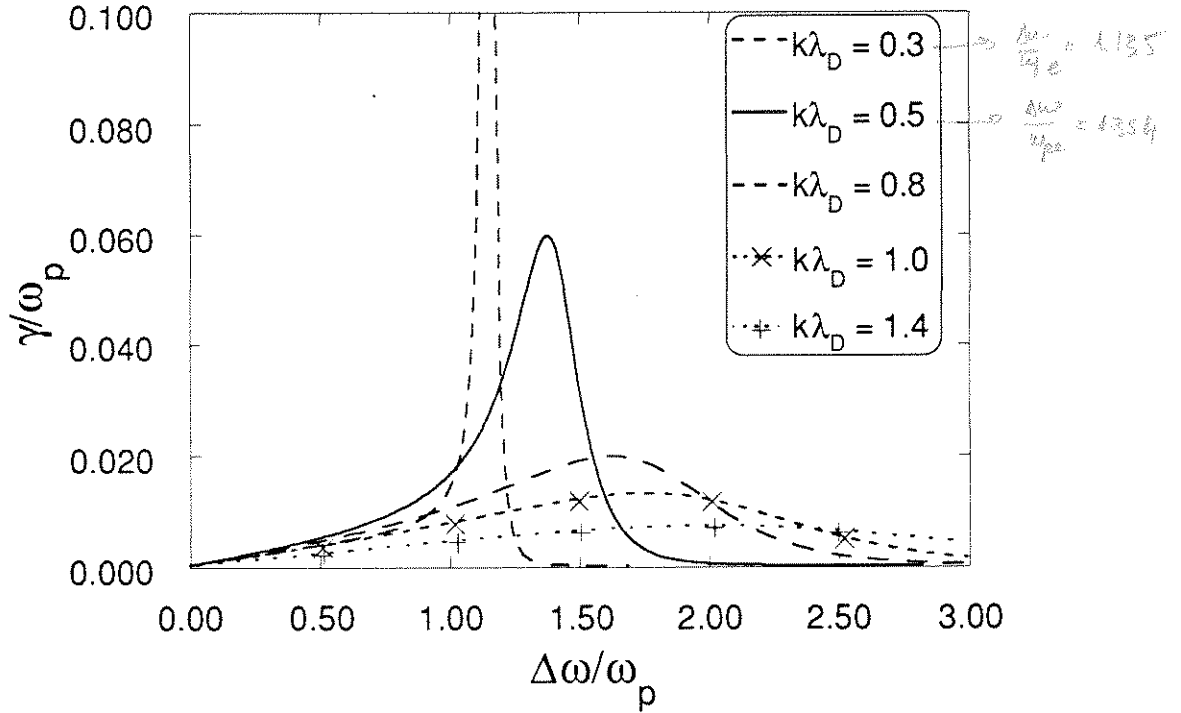
Figure 2.1: Stimulated Compton scattering growth rate $\gamma/\omega_p = c\ \kappa/\omega_p$ vs. $\Delta\omega/\omega_p$ for different values of $k\lambda_D$

9

For small $k\lambda_{De}$ the wavelength of the ponderomotive potential, resulting from the beat between the pump and the scattered light, is longer than the Debye length so that the "beat" can see a high frequency resonance in the Debye cloud, at the Bohm-Gross frequency. Hence, the growth rate is large and the spectrum narrow. However, as $k\lambda_{De}$ increases the interaction of the "beat" with the plasma is now heavily damped and dominated by resonant thermal electrons rather than the resonance in the dielectric function. As a consequence the growth rate is low and the spectrum is broad.

A second consequence of $k\lambda_{De}$ increasing is that the ratio of phase velocity of the "beat" to the thermal velocity reduces Fig.(2.2). If the wave amplitude is large enough to trap background electrons, a self-induced modification of the distribution can occur, which as we will show, can be the main saturation mechanism of the instability.
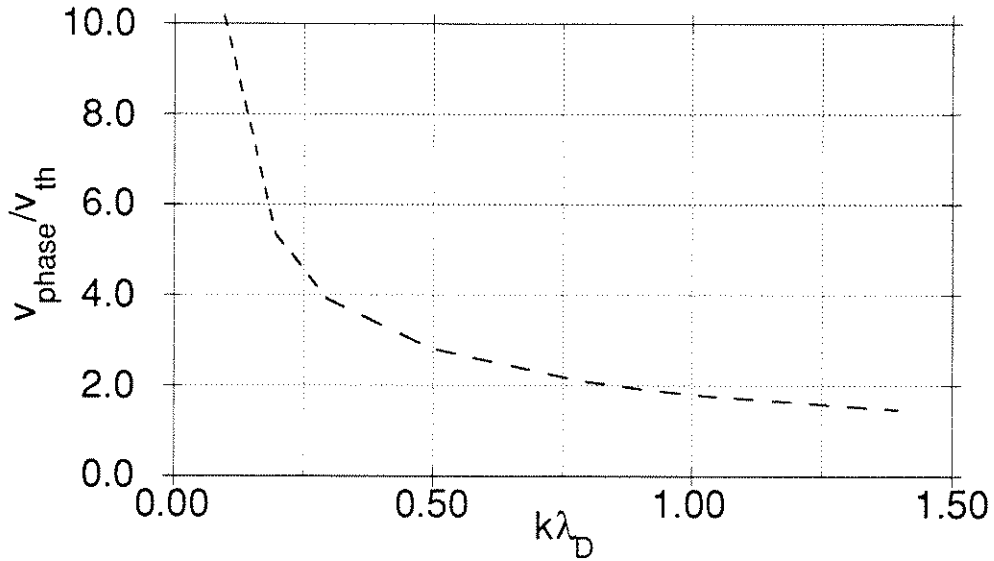
Figure 2.2: Ratio of phase velocity of SCS driven plasma wave and thermal velocity v_{th} vs. $k\lambda_D$.

2.3 Experimental Results

2.3.1 Experimental Set-up

The experimental apparatus is as follows. The laser driving the instability is a CO_2 laser operating at 10.6 μm with a measured output pulse rise time of about 100 ps and a full width at half maximum of about 270 ps. For these experiments the peak power is varied up to about 150 GW giving a focused intensity of about 10^{14} W/cm^2 in a measured spot size of 340 μm diameter. The plasma source is a 1 cm long, multiple-cathode, pulsed (10 μs), high-current (2.5 kA) arc discharge in hydrogen [Fig.(2.3) and (2.5)] or argon [Fig.(2.4)] gas. The resulting electron density can be varied from less than 10^{15} to more than 10^{17} cm^{-3} by varying the fill pressure of the gas, the peak discharge current, and the elapse time between the start of the discharge and the CO_2 laser pulse. For elapse times larger than 10 μs, the arc plasma is fully ionized to $Z=1$. In the Thomson scattering setup, the frequency-doubled Nd:YAG laser probe beam (150 mJ, 5 ns) and the scattered light collection optics are arranged to phase match to density fluctuations with wavenumber $(2 \pm 0.2)k_0$. The scattered light is sent through a spectrograph, with a spectral dispersion of 8 Å/mm, to the 10 mm long slit of a streak camera. The temporal (spectral) resolution of the system is 10 ps (0.2 Å). For time-integrated measurements, a linear detector array replaces the streak camera. A spectrometer and pyroelectric linear array are used to record the spectrum of the CO_2 backscatter signal.

2.3.2 Observation of Linear Convective Saturation

To access a parameter space which is unambiguously in the Compton regime, we reduced the arc-plasma density until the scattered signals appeared broad on the linear array detectors indicating, as described by Eq.(2.3), that $k\lambda_{De}$ is larger than 0.3. In Figs.(2.3a) and (2.3b) time-integrated CO_2 backscatter and Thomson scatter spectra, respectively, are shown from low plasma densities.
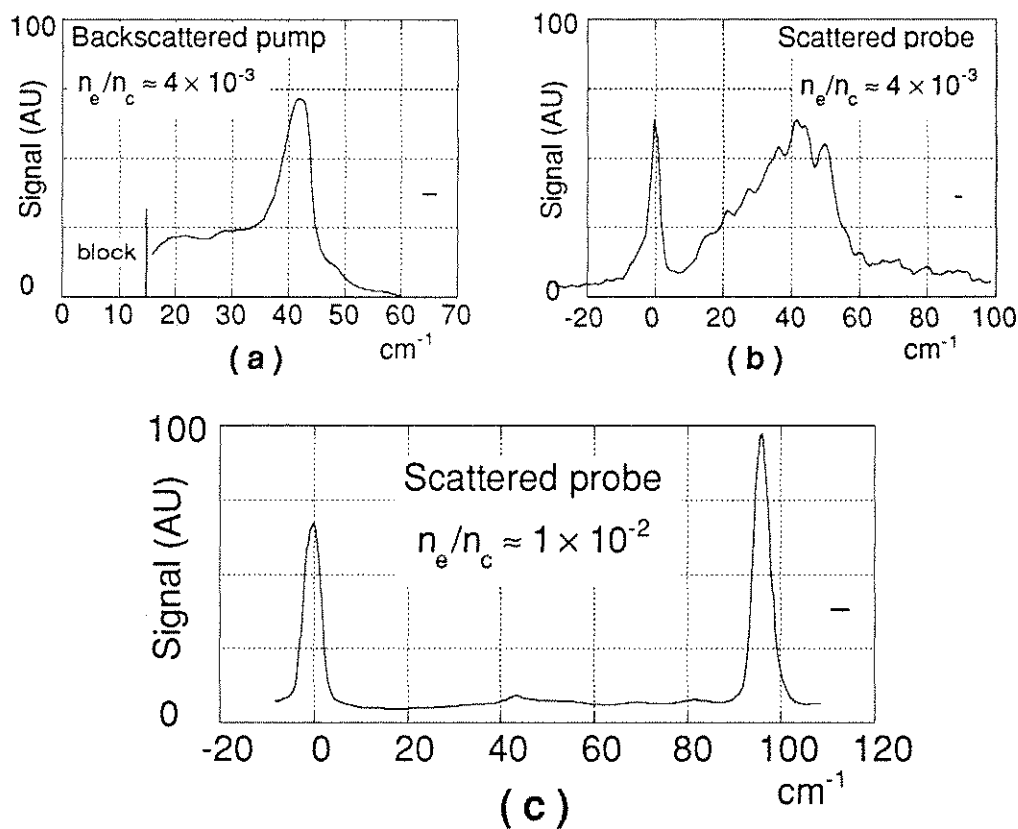
Figure 2.3 Time-integrated CO_2 backscatter spectrum (a) and probe beam Thomson scatter spectrum (b) from a low density hydrogen plasma and time-integrated probe beam Thomson scatter spectrum from a high density plasma (c). The three spectra are from different laser shots. The peaks at zero shift are from SBS [physically blocked in (a)]. The horizontal bars indicate the instrument width.

12

Both spectra exhibit a sharp edge on the high-frequency side and a gradual reduction on the low frequency side as expected from the frequency-dependence of the growth rate. This is in contrast to the scattered signals from high density plasmas with $k\lambda_{De} < 0.3$ which show a sharp, instrument-limited peak characteristic of the Bohm-Gross frequency shift [Fig.2.3(c)].

To quantitatively compare the experiment with the linear theory, we time resolved the Thomson scattering data. Figure 2.4(a) shows the frequency spectrum of the Thomson-scattered light versus time.

Figure 2.4 (a) Streak camera image of the Thomson-scattered probe beam in an argon plasma. Although not shown here, there was no blue-shifted spectral feature visible in the original data. The white bar indicates the location of a $100 \times$ attenuator for SBS. The peak intensity is 1.5×10^{14} W/cm^2. (b) Line-out of streak data (solid curve) taken along the direction of the arrow and best fit from Compton theory (dashed curve).

13

We see a feature with an approximately 8 Å red-shift (28 cm^{-1}) from the 5320 Å probe light which we identify as light scattered by electron density fluctuations associated with SCS. This feature is followed in time by an essentially unshifted feature due to stimulated Brillouin scattering (SBS) (Forslund et al. 1975) driven ion acoustic waves. Note that the lack of a blue-shifted feature verifies that these are laser-driven density fluctuations (non-thermal) propagating in the same direction as the CO_2 laser beam.

To fit the data to a linear SCS theory, line-outs were taken at a time before convective saturation, as shown in Fig.(2.4a). Equation (2.4a) is used to fit the data. An enhanced noise level about 5 times nominal thermal level was used as it produced a better fit to the data. Values for $k\lambda_{De}$ and n_e are adjusted to fit the shape and scale of the theoretical spectrum to the experimental spectrum. Using Eq.(2.4a) with T=25 ps (the transit time for the scattered light wave), v_o/c is adjusted to scale the peak amplitude of the theoretical spectrum to that of the measured spectrum. Effectively, v_o/c is some average value over the growth time. The parameters which best fit the data are $v_o/c \approx$ 0.08, $n_e \approx 4 \times 10^{15}$ cm^{-3} and $k\lambda_{De} \approx 1.5$ so that $T_e \approx$ 120 eV. The inferred plasma density agrees roughly with line-average interferometric density measurements made under similar arc discharge conditions. We do not expect the density to change due to collisional or tunneling ionization since the rates for these processes are too slow (see Chapter 3 for details). Since $k\lambda_{De}$ is about 1.5, the phase velocity v_ϕ for the strongest mode is $v_\phi \approx 1.0 v_e$ putting it right in the bulk of the electron distribution function. The ponderomotive potential from the beating of the pump and scattered electromagnetic waves is thus at a velocity where it can directly manipulate the electron distribution function. However, for this very low density case, the SCS reflectivity is too low to allow, through the Manley-Rowe condition, much transfer of power to the plasma. The

scattered spectrum does not show a pronounced variation with time indicating that the electron distribution function is not being significantly altered.

2.3.3 Observation of Non-linear Saturation

2.3.3.1 Experimental Results

The situation is quite different at higher densities and higher reflectivities. Figure 2.5(a) shows a streak camera image of the $2k_o$ density fluctuation spectrum for a ten times higher density plasma and a three times higher laser intensity than in Fig.(2.4a). We see the instability start off at a 23 Å red-shift (78 cm^{-1}). From a line-out through the spectrum, taken at a time when the signal has reached about 60% of the peak level (25 ps into the scattered pulse), we infer the parameters $v_o/c \approx 0.02$, $n_e \approx 6 \times 10^{16}$ cm^{-3} and $k\lambda_{De} \approx 0.6$ so that $T_e \approx 200$ eV and $v_\phi/v_e \approx 2.2$.

Examination of the inner or more intense contours of Fig.(2.5a) shows that the spectrum makes a fairly sudden turn towards lower frequency and the lower frequencies become suddenly enhanced at about the same time that the original 23 Å feature saturates. Line-outs of Fig.(2.5a) representing the time histories of four frequencies (as marked by arrows on the streak image) are shown in Fig.(2.5b). We see the enhancement of the growth rate of the 22 Å-shifted light coincident with the saturation of the 23 Å feature. Also, we see the smaller frequency shifts peaking progressively later in time. The 16 Å-shifted light peaks well after the 23 Å feature saturates indicating that the saturation of the 23 Å feature was not due to an absence of the pump. The frequency spectrum during the final state of the instability is similar to the large $k\lambda_{De}$ spectrum of

Fig.(2.4a) in that it extends down to $\Delta \omega = k\, v_\phi \approx 1.1\, k v_e$. That is, the instability involves particles in the bulk of the distribution function.
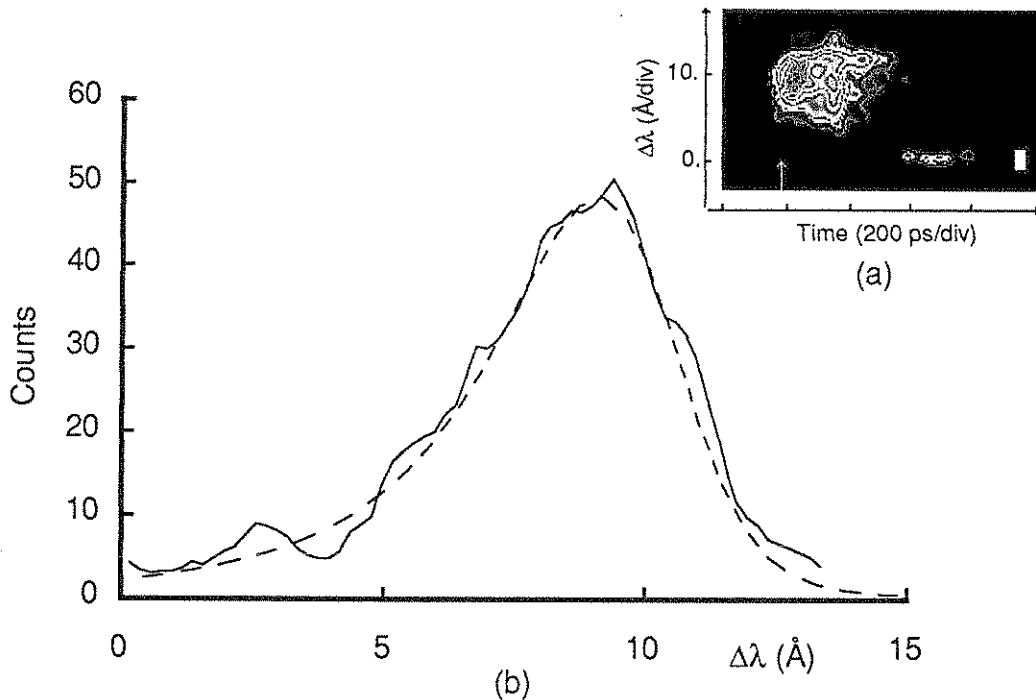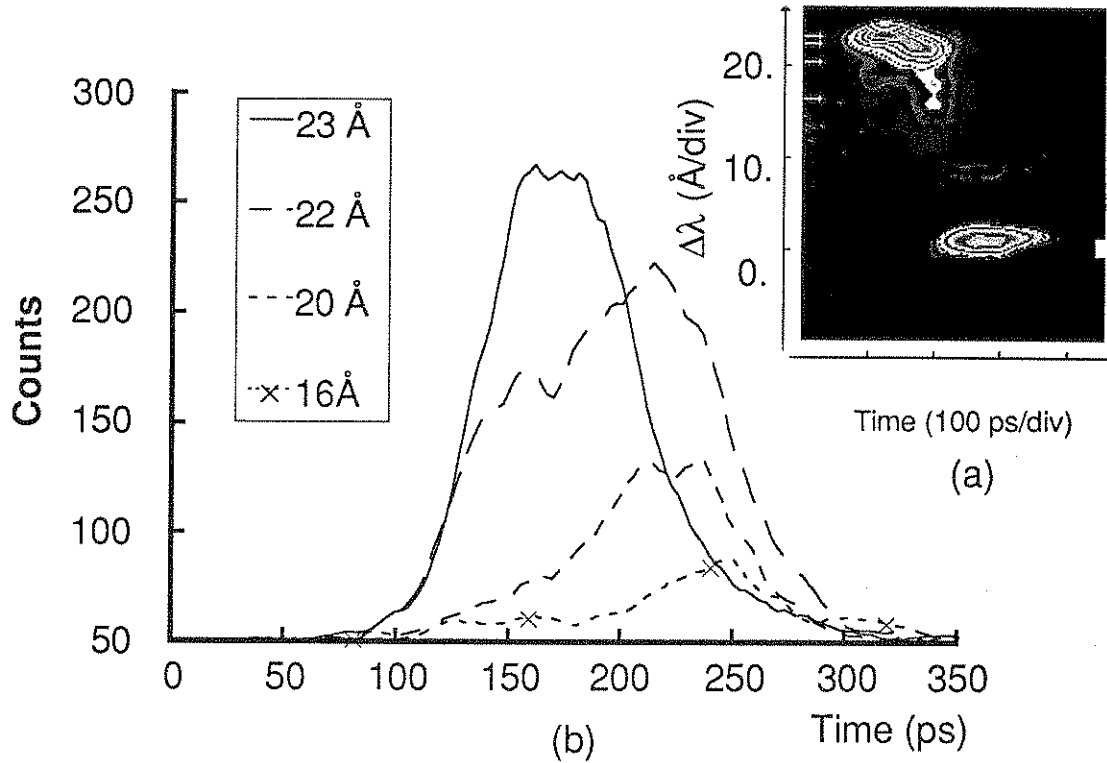

Figure 2.5: (a) Streak camera image of the Thomson scattered probe beam in a hydrogen plasma. Although not shown here, there was no blue-shifted spectral feature near 20 Å visible in the original data. (The feature at 8 Å of red-shift, which does have a blue-shifted counterpart, is due to mode coupling of driven fluctuations with the SBS acoustic wave (Darrow et al. 1985) due to the presence of a weak second frequency in the laser pulse for this particular data shot). The white bar indicates the location of a $100 \times$ attenuator. The peak intensity is 5×10^{13} W/cm^2. (b) Line-outs taken along the direction of the four arrows in (a).

It should be noted that while Compton scattering is occurring in the experiment the ratio v_o/v_e is typically 3 and therefore filamentation may also be operative. Any density reduction due to self-focusing will shift the Thomson spectrum from Compton induced density fluctuations towards lower frequencies [Fig.(2.5)].

However the simultaneous broadening of the spectrum as the higher frequencies saturate cannot be accounted for by invoking self-focusing and one is led to look for another saturation mechanism.

2.3.3.2 Saturation Mechanism

Equation (2.3) suggests that one way to saturate the instability is to change the electron distribution function $f(v)$ and therefore the electron susceptibility χ_e such that the growth rate $\gamma(\Delta\omega, f(v))$ no longer has a resonance at the original 23 Å shift but perhaps at a lower frequency shift. This could account for both the saturation of the scattered light signal at the original frequency shift and the appearance of signal at new frequency shifts at later times, as seen in Fig.(2.5). To test this idea we ran the electromagnetic particle-in-cell computer code WAVE to simulate the experiment. A one spatial-dimensional simulation with $k\lambda_{De} = 0.6$ was run. The backscattered frequency spectrum was monitored as was the longitudinal electron distribution function . In this simulation, the peak backscatter signal built up and saturated while at the same time, the longitudinal distribution function became asymmetric, with a tail being pulled out on the side moving along k_o [Fig.(2.6)]. This is due to momentum deposition to electrons with a velocity near v_ϕ from the reflecting pump photons. The detailed time-evolution of the scattered light spectra looked very similar to the experimental data of [Fig.(2.5a)]. The signal started out narrowband at a frequency corresponding to that of the maximum

17

growth rate for the unperturbed, Maxwellian plasma. As this frequency component saturated, the peak moved to lower frequency shifts (shifting by a factor of about 0.85) and the bandwidth became broader ($\Delta\omega/\omega \approx 30$ %). The power at the original frequency fell after saturation, as it did in the experiment. This could be due to phase mixing of the bunched electrons contributing to that particular mode, once that mode is no longer driven. The reason that the mode is no longer driven can be seen from the theoretical growth rate of Eq.(2.3). When the electron distribution function is perturbed, the poles of the function move to new frequencies. In fact, when we numerically solve for χ_e using the final electron distribution function from WAVE as an input and use the result in Eq.(2.3), we find that the growth rate peak has indeed shifted towards lower frequency and has become broader. Thus, it seems that Compton scattering is self-limiting in low density plasmas because the momentum absorbed in the instability is typically enough to perturb the distribution function and thereby turn the instability off at any particular frequency (Albritton 1975). Although SRS could grow in the flattened region of $f(v)$, phase space turbulence associated with particle trapping can account for the absence of SRS in both experiment and simulation. The SCS induced CO_2 reflectivity was 10^{-4}.

We should note that, with the very short 100 ps rise time for the laser pulse, the electron-time-scale processes occur before SBS has a chance to grow, thus experimentally decoupling the two instabilities . Typically, SBS comes up late in the SCS pulse or even well after the SCS has shut off and is not thought to terminate SCS.
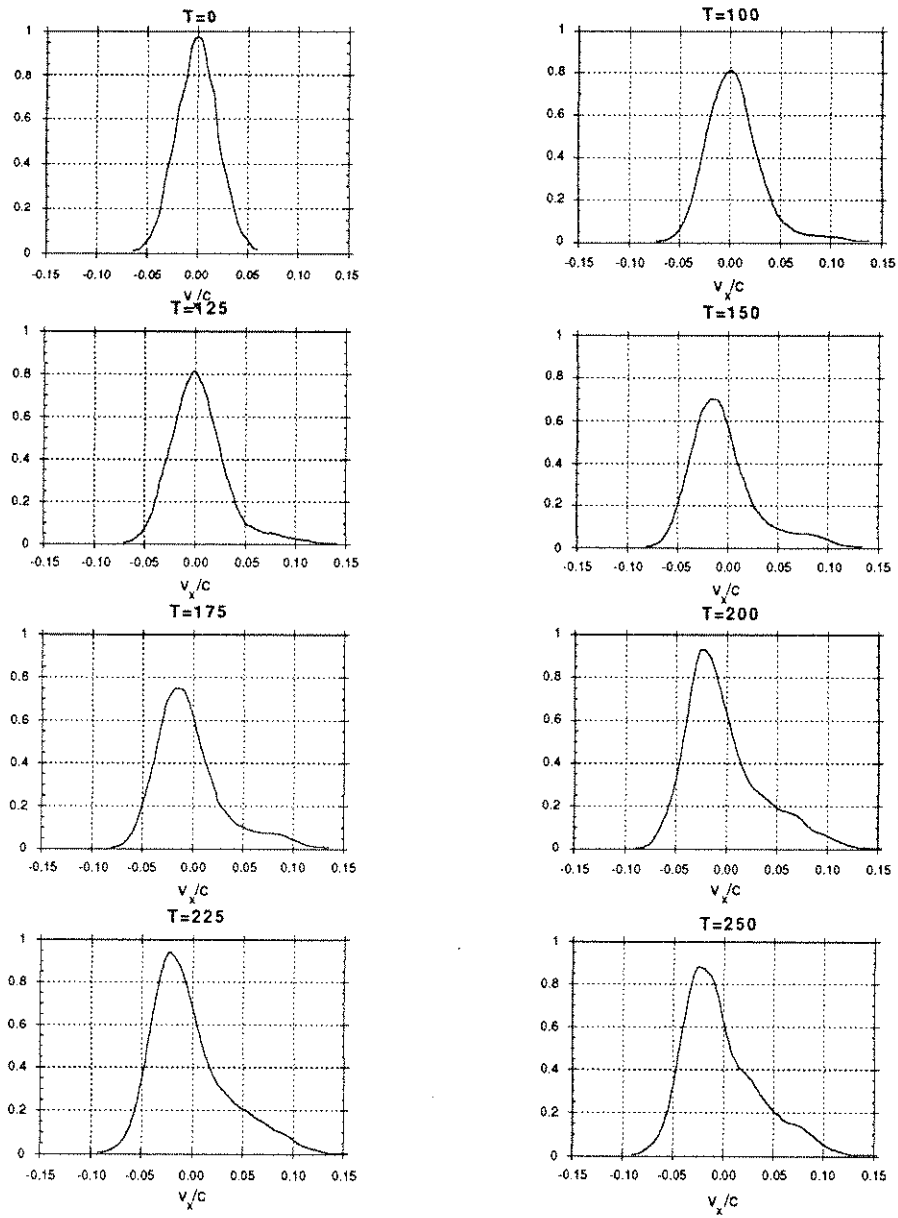
Figure 2.6: Longitudinal distribution function resulting from a 1 D WAVE simulation at different instances in time. The pre-formed density was equal to $n/n_c = 0.01$ and the initial thermal electron velocity was $v_{th} = 0.028c$. The laser driver strength was equal to $v_{osc}/c = 0.1$.

19

2.4 Conclusion

We have made the first detailed spectral measurements of stimulated Compton scattering from a pre-formed plasma. For low density, the observed density fluctuation spectra seem to be convectively saturated and have the predicted large spectral bandwidth throughout the time of interaction. The scattered light peaks at a frequency shift $\Delta \omega$ corresponding to a phase velocity about equal to the electron thermal velocity. For higher density, an initially narrow spectrum is seen to saturate and evolve into broadband Compton scattering with frequency shifts once again near kv_e. Using the code WAVE as a guide, we suggest that the saturation is due to a reflectivity-induced modification of the electron distribution function.

As we have shown in this chapter, the characteristics and evolution of the SCS instability are determined by the plasma properties. By measuring the complete frequency spectrum of the density fluctuations associated with SCS, one can obtain a local estimate of both the plasma density and temperature. In the next chapter we will look into the plasma physics aspects of tunnel-ionized gases. Based on the insights gained in the study of SCS in a pre-formed plasma, Thomson scattering of SCS driven fluctuations will now be used as a diagnostic for, and provide information on the properties of plasmas produced through tunnel-ionization.

Chapter 3

Plasma Physics Aspects of Tunnel-Ionized Gases

3.1 Introduction

In this Chapter we explore the plasma physics aspects of gases ionized via tunneling ionization through experiments and supporting particle-in-cell computer simulations. Most of the work on tunneling ionization of gases has been conducted in a very low pressure gas, i.e. single particle regime. High density plasma production using tunneling ionization has recently become of interest for X-ray recombination lasers and plasma based accelerators as discussed in Chapter 1. In such plasmas space-charge effects cannot be neglected thereby complicating a simple extrapolation of the single particle results to predict the properties and behavior of macroscopic plasmas. Plasma physics issues need to be considered in determining both the initial plasma characteristics and the evolution of such a plasma.

As shown in Fig.(3.1) we divide the interaction of the laser with the gas target into three different phases. In the first phase, the ionization phase, the laser intensity has exceeded the ionization threshold and the gas becomes ionized. We calculate the time evolution of the plasma density and the electron distribution functions using the Keldysh model of tunneling ionization. In this model the electron tunnels through the suppressed Coulomb barrier of the nucleus and then interacts classically with the applied electromagnetic fields. The key predictions from this model are that a plasma can be

obtained with a fully ionized density (controlled by the fill pressure) and a polarization dependent, anisotropic distribution function. The transverse distribution is much hotter than the longitudinal distribution. Furthermore, when using linear polarization harmonics of the laser frequency will be generated through the stepwise ionization process.
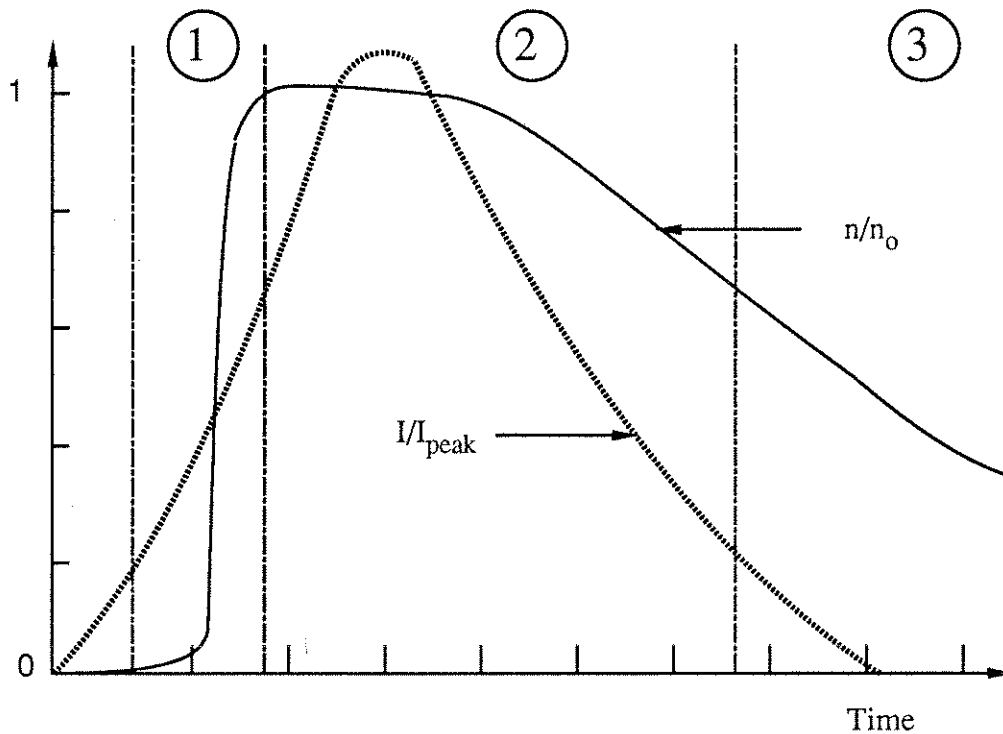
Figure 3.1: Hypothetical plot of the plasma density n normalized to the neutral gas fill density n_0 (solid line) and the laser intensity I normalized to the peak intensity I_{peak} (dashed line) vs. time. The three different phases in the interaction of a high intensity laser beam with a gas are denoted by the point-dash lines.

In this ionization phase, the laser-plasma parametric instabilities such as SRS and SCS are strongly affected by the rapidly varying plasma density and rapidly

evolving anisotropic plasma temperature. Also the maximum density of the plasma can be clamped due to beam refraction. Refraction occurs as a consequence of the highly non-linear tunneling ionization rate which can lead to steep plasma density gradients in the transverse or radial direction.

In the second phase, plasma physics issues resulting from the continued interaction of the high intensity laser beam with the space-charge dominated plasma have to be considered. When electrons are born into fields which have a longitudinal component (such as in a focusing or refracting beam), they will have a longitudinal drift velocity leading to a high $T_\parallel$. Also, electrons born at the same longitudinal but different radial position will end up with a different drift velocity magnitude due to the radial field dependence and cause a smearing of the resulting distribution function. Furthermore the electrons, retained by the space-charge, keep interacting with the radial and longitudinal space dependent electromagnetic fields. Both effects give rise to an effective stochastic heating.

If the plasma density changes on a slow enough time scale, the parametric instabilities can start growing. For small $k\lambda_D$ (high plasma density, low $T_\parallel$) SRS will grow while for large $k\lambda_D$ SCS will grow. At the same time the anisotropic distribution function will relax due to instabilities such as the Weibel instability, causing a continued increase of $T_\parallel$ which in turn influences the evolution of SRS/SCS. On the longer time scales SBS will grow and hydro-dynamic effects such as plasma expansion and/or ponderomotive blow out will become important.

In the third phase, the laser intensity drops below the threshold for the parametric instabilities but the isotropization due to the Weibel instability can continue. Eventually the plasma will recombine.

In this Chapter we describe some of the first experiments which explore the physics issues unique to tunnel-ionized plasmas as discussed above. Understanding of these plasmas has been aided by particle simulations in which the plasma is created via the tunneling ionization process.

3.2 Theoretical Considerations

3.2.1 Tunneling Ionization Model

The characteristics of a plasma, produced through ionization of a gas by an intense laser are calculated using the tunneling model (Keldysh 1965). First we calculate the plasma density evolution during the ionization phase and next we calculate the resulting electron distribution functions at the end of the ionization phase. In tunneling ionization, the rate at which the plasma density increases is given by

$$\frac{dn(t)}{dt} = w(t)(N - n(t)) \tag{3.1}$$

where $n(t)$ is the time dependent plasma density, N is the initial neutral gas density and $w(t)$ is given by (Landau 1978)

$$w(t) = \frac{4m_e e^4}{\hbar^3} \left(\frac{E_i}{E_h}\right)^{5/2} \zeta \exp\left[-\frac{2}{3}\left(\frac{E_i}{E_h}\right)^{3/2} \zeta\right] \tag{3.2}$$

Here E_h and E_i are the ionization potential of hydrogen and the atom in question, $\zeta = E_a/E(t)$ where $E_a = m_e^2 e^5 / \hbar^4$ is the atomic unit of electric field, and $E(t)$ is the amplitude of the applied electric field. In the "plasma regime" we expect that a small fraction of electrons will leave the focal volume and build-up a space charge potential. A simple estimate, based on Gauss' law, shows that the space charge potential reaches a

large enough value to confine the bulk of the remaining electrons when a charge imbalance δn exists larger than

$$\delta n = \frac{\Phi_p}{2\pi e^2 \sigma^2} \tag{3.3}$$

Here σ is the radius of the plasma cylinder, defined as the position where the laser intensity is at its threshold value for ionization and Φ_p is the ponderomotive potential of the laser field. For our experimental parameters δn needs to exceed 10^{12} cm^{-3} for space charge to retain the electrons. The rate equation for the plasma density has been verified experimentally and found to adequately model the time evolution of the plasma density (Downer et al. 1990).

As an example, using a CO_2-laser with a peak intensity of 3×10^{14} W/cm^2 and pulse rise time of 150 ps focused in hydrogen gas we find from Eq.(3.1) that the density builds up rapidly in 20 ps once the ionization threshold of 6×10^{13} W/cm^2 is exceeded. For a given intensity, the ionization onset occurs later with circular than with linear polarization since the field strength is $\sqrt{2}$ lower.

In the absence of plasma effects, the evolution of the electron energy distribution can be calculated assuming classical interaction of the newly born electrons with the ionizing electromagnetic fields (Landau 1962, Corkum et al. 1989). Assuming that the electron is born at rest in a specific phase of the electric field, given by $\mathbf{E} = E\sin\omega_o t \, \mathbf{x} + \alpha E\cos\omega_o t \, \mathbf{y}$, one finds that its energy in the laser field is comprised of the usual quiver energy,

$$E_{osc} = \frac{1}{2}m v_{osc}^2 = \frac{1}{2}\frac{e^2 E^2 \cos^2 \omega_o t}{m\omega_o^2} \tag{3.4}$$

plus translational energy

$$E_{trans} = m\frac{v_x^2 + \alpha v_y^2}{2} \tag{3.5}$$

where v_x, v_y are the DC-drift velocity component in the x and y direction respectively, and α is the degree of ellipticity of the incident polarization. Here e and m are the usual electron charge and mass respectively, and ω_0 is the laser frequency. This drift velocity arises because the transverse canonical momentum of the electron in a plane wave is a constant of the motion. This model has been shown to predict the correct values of laser polarization dependent anisotropic drift energy distributions in an experiment in the single atom regime by Corkum et al. (Corkum et al. 1989). 1-D calculations show that , for previously considered laser parameters, an anisotropic quasi - Maxwellian with a
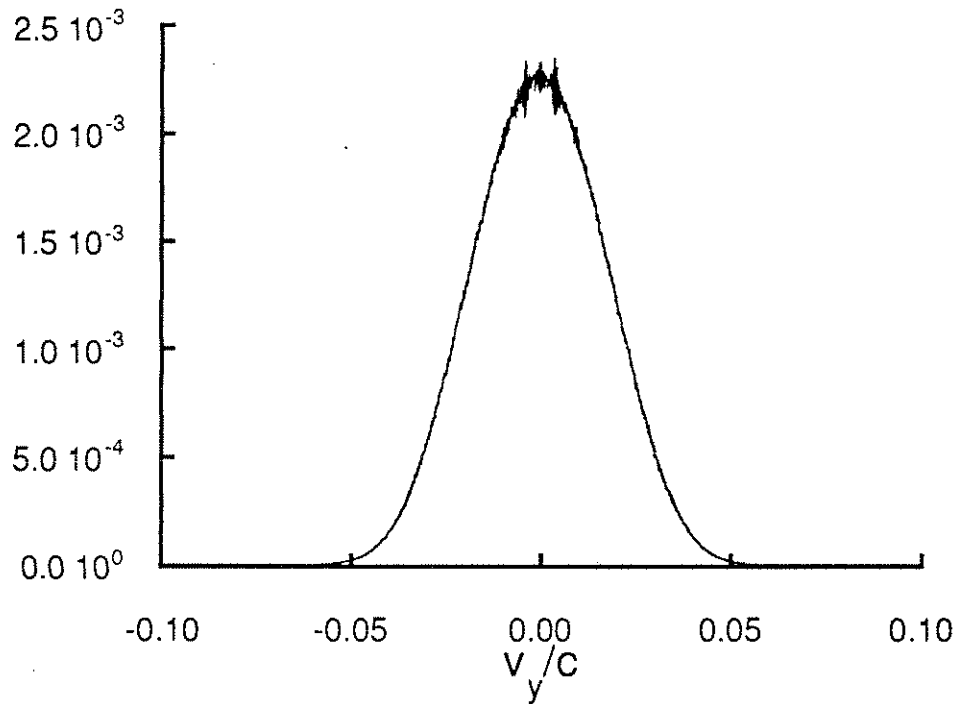
Figure 3.2: Calculated (single particle regime) transverse electron drift velocity distribution $f(v_y)$ produced by a linearly polarized laser with an intensity of 1.2 x 10^{14} W/cm^2, in argon gas. This quasi Maxwellian distribution has a temperature $T_\perp$ of about 150 eV. The longitudinal drift velocity distribution (not shown) is also quasi Maxwellian with $T_\parallel$ << 1 eV.
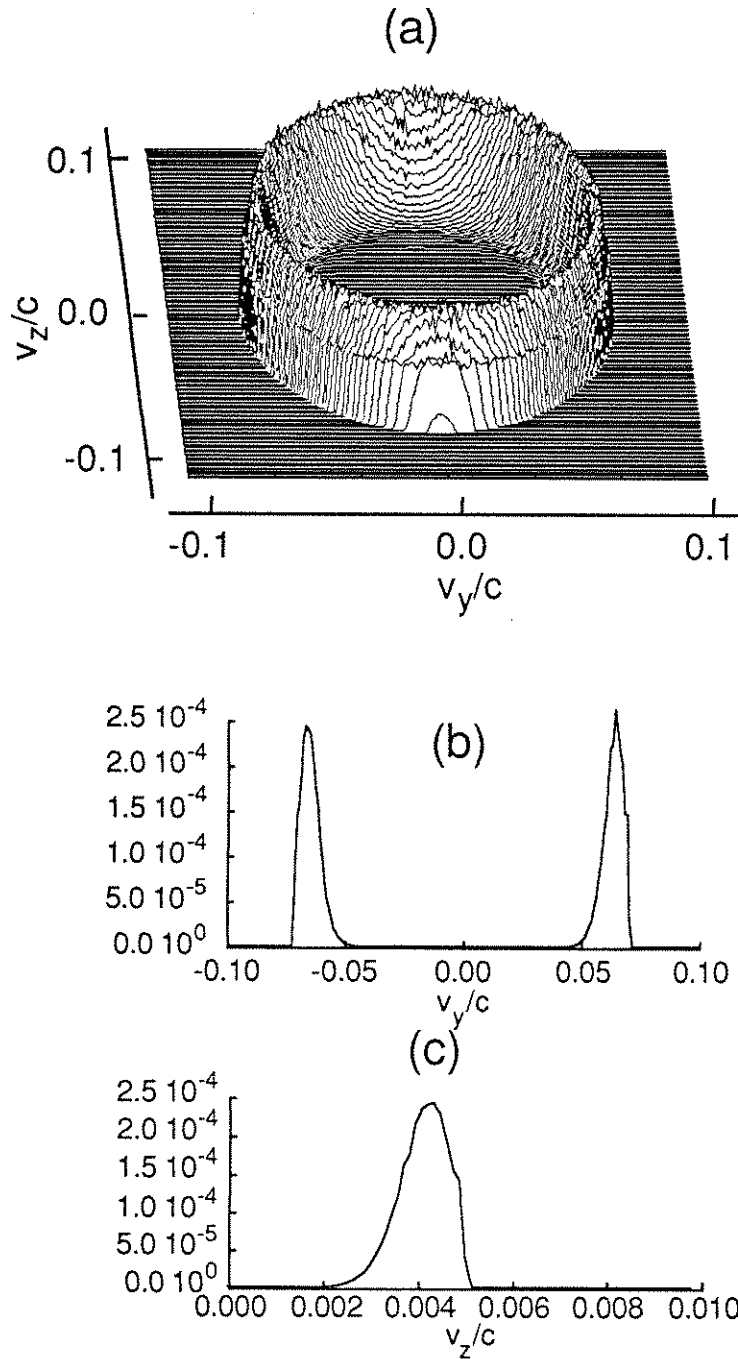
Figure 3.3: (a) The calculated (single particle regime) 2D transverse electron drift velocity distribution f(v_y, v_z) produced by a circularly polarized laser with an intensity of 1.2 x 10^{14} W/cm², in argon gas. (b) Slice through (a) at $v_z = 0$, showing a major radius of 0.065 c and a minor radius of 0.006 c. (c) Associated longitudinal drift velocity distribution (10 times expanded velocity scale).

transverse temperature $T_\perp \approx 150$ eV and and a longitudinal temperature $T_\parallel \ll 1$eV is produced for linearly polarized light upon completion of ionization. This is shown in Fig.(3.2).

For circularly polarized light, a ring distribution with a major radius (transverse to the incident laser beam wave vector k_0) of 2.5 keV and a minor radius of 1 keV with $T_\parallel$ of only 4 eV is generated. This is shown in Figs.(3.3a,b,c).

To summarize, from the tunneling ionization model one expects that fully ionized plasmas with controllable $T_\perp$ and negligible $T_\parallel$ can be produced. Next we will investigate the validity of these predictions through experiments and simulations.

3.2.2 Stimulated Raman Scattering in a Time Varying Plasma

In the experiment coherent Thomson scattering of SRS and/or SCS driven high frequency density fluctuations will be used to provide information on the evolution of the plasma density and temperature. In a seminal paper by M. N. Rosenbluth the theory of the three-wave parametric instabilities for weakly inhomogeneous media was derived (Rosenbluth 1972). Following a similar analysis we consider the effect of time varying plasma conditions on the growth of electron density fluctuations excited through stimulated Raman or Compton scattering. The time dependence comes about through ionization and/or plasma heating. First we will analyze Raman scattering in a cold plasma with a time dependent density and/or pump strength. Next we will include the effect of a time dependent temperature for the case of Compton scattering.

Let $E_0(\omega_0, k_0)$ be the pump wave, $E_1(\omega_1, k_1)$ the scattered electro-magnetic wave and $E(\omega, k)$ the electrostatic plasma wave. The plasma density n is assumed to be spatially uniform but to vary as a function of time. In the case of tunneling ionization the rate at which n changes, is given by Eq.(3.1) whereas for collisional ionization the rate is given by

$$\frac{dn}{dt} = \lambda\, n[N - n] = \lambda\, n\, N\left[1 - \frac{n}{N}\right] \qquad (3.6).$$

The equation of continuity is modified for an ionizing plasma through the addition of a source term $S(t)$:

$$\frac{\partial n}{\partial t} + \nabla \cdot (nv) = S(t) \qquad (3.7).$$

Assuming that electrons are born at rest $S(t)$ is equal to the ionization rate. Denoting the fluctuating density by ñ we write the density as $n = n_0 + ñ$ where n_0 is the background electron density. Since the rate of plasma production due to tunneling ionization only depends on the available amount of neutrals $N - n(t)$, there is no change in the equation of continuity for the fluctuations. However, for collisional ionization the rate is proportional to the amount of free electrons. If there is an electron density fluctuation present in the plasma it would naively imply that at local density maxima a higher ionization rate could enhance the desnity fluctuations. For a propagating fluctuation however this local enhancement smears out and since the new born electrons do not oscillate the wave is actually damped. The equation of continuity for ñ is then

$$\partial_t ñ + n_o \nabla \cdot \tilde{v} = 0 \qquad (3.8).$$

The equation of motion of the density fluctuations is modified by the ionization through the addition of a damping term (Appendix B)

$$\partial_t v + \frac{e}{m} E = -\nabla\left(v_o \cdot v_1^*\right) + \lambda\left(1 - \frac{N}{n_o}\right) v \qquad (3.9).$$

Taking the divergence of Eq.(3.9) and the time derivative of the equation of continuity and using Poisson's equation

$$\nabla \cdot E = -4 \pi \tilde{n} e \tag{3.10},$$

we obtain

$$\partial_t^2 \tilde{n} + \nu \partial_t \tilde{n} + \omega_p^2(t)\tilde{n} = n_o \nabla^2 \left(v_o \cdot v_1^* \right) \tag{3.11}$$

describing the driven density fluctuations in an ionizing plasma. Here ν is the phenomenological damping rate and

$$v_j = \frac{e\, E_j}{m\omega_j} \tag{3.12},$$

where E_0 is the applied electro-magnetic field at frequency ω_0 and E_1 is the backscattered electro-magnetic field at frequency ω_1. From Maxwell's equations we can also derive the equation governing the behavior of the scattered E.M. wave :

$$\left(\partial_t^2 + c^2 \nabla^2 + \omega_p^2 \right) E_1 = -\omega_p^2 \tilde{n}^* E_o \tag{3.13}$$

where we have assumed $\omega/\omega_0 \ll 1$ which is valid for underdense plasmas.
We now write

$$\begin{cases} \tilde{n} = \hat{n} e^{i\left(kx - \int \omega\, dt\right)} \\ E_o = \hat{E}_o e^{i\left(k_o x - \int \omega_o dt\right)} e_o \\ E_1 = \hat{E}_1 e^{i\left(k_1 x - \int \omega_1 dt\right)} e_1 \end{cases} \tag{3.14}$$

and will assume that $\hat{n}, \hat{E}_0, \hat{E}_1$ are slowly varying amplitudes, i.e.

$$\begin{cases} \partial_t^2 \hat{n} \ll \omega\, \partial_t \hat{n} \\ \partial_t^2 \hat{E}_j \ll \omega\, \partial_t \hat{E}_j \end{cases} \tag{3.15}$$

where j=0,1.

Applying the Fourier tranform in space and using Eq.(3.15) we can rewrite the coupled equations (3.11), (3.13), in the slowly varying envelope approximation :

$$\begin{cases} (v - 2i\omega)\partial_t \hat{n} - i\omega v\, \hat{n} = -\dfrac{e^2 k^2 \hat{E}_o}{m\omega_o \omega_1} n_o \hat{E}_1^* e^{-i\int \Delta\omega\, dt} = -A\, E_1^* e^{-i\int \Delta\omega\, dt} \\ (v_1 + 2i\omega_1)\partial_t \hat{E}_1^* + i\omega_1 v_1 \hat{E}_1^* = -\omega_p^2 \hat{n}\, \hat{E}_o^* e^{i\int \Delta\omega\, dt} \end{cases} \qquad (3.16a,b)$$

Here v_1 is a phenomenological damping rate of the electromagnetic wave, $\Delta\omega = \omega_o - \omega_1 - \omega$ and $A = \dfrac{e^2 k^2 \hat{E}_o}{m\omega_o \omega_1} n_o$. Since the plasma is assumed to be homogeneous there is no wavevector mismatch, i.e. $\Delta k = k_o - k_1 - k = 0$. Eliminating E* from Eqs.(3.16a,b) we obtain the following equation for n*:

$$\partial_t^2 \hat{n} + \partial_t \hat{n}\left[i\Delta\omega - \frac{\dot{A}}{A} - \frac{i\omega v}{v - 2i\omega} + \frac{i\omega_1 v_1}{v_1 + 2i\omega_1} + \frac{\dot{v} - 2i\dot{\omega}}{v - 2i\omega} \right] +$$

$$\hat{n}\left[\frac{\left(\Delta\omega + i\frac{\dot{A}}{A}\right)\omega v}{v - 2i\omega} + \frac{\omega\omega_1 vv_1 - \Gamma_o^2}{(v_1 + 2i\omega_1)(v - 2i\omega)} - \frac{(\dot{\omega}v + \omega\dot{v})}{v - 2i\omega} \right] = 0 \qquad (3.17)$$

where $\Gamma_o^2 = A\omega_p^2 \hat{E}_o^* = \dfrac{e^2 k^2 E_o^2}{m\omega_o \omega_1}\omega_p^2$ is the homogeneous growth rate for the time independent case. Let $\overline{\Delta\omega} = \Delta\omega + i\dfrac{\dot{A}}{A}, \dfrac{\overline{v}_1}{2} = \dfrac{v_1}{2} + \dfrac{\dot{\omega}}{\omega}, v_{eff} = \dfrac{v}{2} + \dfrac{\overline{v}_1}{2}$ and $\gamma_o^2 = \dfrac{\Gamma_o^2}{4\omega\omega_1}$.

Assume $v \ll \omega_1, \omega$ then we can rewrite Eq. (3.17) as

$$\partial_t^2 \hat{n} + \partial_t \hat{n}\left[i\overline{\Delta\omega} + v_{eff} \right] + \hat{n}\left[i\frac{\overline{\Delta\omega}v}{2} + \frac{v\overline{v}_1}{2} - \gamma_o^2 \right] = 0 \qquad (3.18).$$

Using

$$\hat{n} = n' e^{-\frac{1}{2}\int \left(i\overline{\Delta\omega} + v_{eff}\right)dt} \qquad (3.19)$$

Eq. (3.18) can be reduced to

$$\partial_t^2 n' + n' \left[-\frac{i}{2}\overline{\dot{\Delta\omega}} - \frac{1}{4}\left(i\overline{\Delta\omega} + \frac{\overline{v_1} - v}{2} \right)^2 - \gamma_o^2 \right] = 0 \qquad (3.20).$$

In general, the detuning $\Delta\omega$ can be a complicated function of time. Since the electromagnetic waves satisfy the dispersion relation, the rate at which their frequency changes due to a change in the plasma frequency is given by $\dfrac{d\omega_j}{dt} = \dfrac{\omega_p}{\omega_j}\dfrac{d\omega_p}{dt}$ where

$j=0,1$. For an underdense plasma we therefore find that

$$\frac{d\Delta\omega}{dt} = \frac{d\omega_0}{dt} - \frac{d\omega_1}{dt} - \frac{d\omega}{dt} \approx -\frac{d\omega_p}{dt} \qquad (3.21),$$

and $\omega = \omega_p$. To obtain an analytic expression for the amplification of the density fluctuations due to Raman scattering we now linearize the detuning $\Delta\omega$ in time around the point where $\Delta\omega = 0$, i.e. $\Delta\omega = -B\ t$. From Eq.(3.22) this then implies that the density is assumed to increase quadratically with time around $t = 0$. We next assume that the pump strength varies on a slower time scale than the density and that the effective damping $v_1 - v$ is small. Normalizing time to $t = t'/B^{1/2}$, Eq.(3.20) becomes

$$\partial_t^2 n' + \frac{t'^2}{4}n' + \left[\frac{i}{2} - \frac{\gamma_o^2}{B} \right]n' = 0 \qquad (3.22).$$

An approximate solution for $\dfrac{\gamma_o^2}{B} > 0$ is then

$$n' = n'_o \ \sinh \int_{-t_c}^{t_c} \left(\frac{\gamma_o^2}{B} - \frac{t'^2}{4} \right)^{\frac{1}{2}} dt' \qquad (3.23),$$

where we have neglected "i" in Eq.(3.22) since we assume finite amplification larger than 1. The integration is carried out to the turning points $t_c = 2\dfrac{\gamma_o}{\sqrt{B}}$. The net e-folding is then

$$K = \int_{-t_c}^{t_c} \left(\frac{\gamma_o^2}{B} - \frac{t'^2}{4} \right)^{1/2} dt' = \pi \frac{\gamma_o^2}{B} \tag{3.24}$$

and hence $n' = n_o' \exp\left[\pi \frac{\gamma_o^2}{B} \right]$ (3.25)

or $\hat{n} = n_o' \exp\left[\pi \frac{\gamma_o^2}{B} - \frac{\gamma_o}{B} v_1 \right]$ (3.26)

The effect of the time dependent density is therefore equivalent to reducing the effective growth rate to $\dfrac{\gamma_o}{\sqrt{B}}$ and allowing the growth to occur only during a time $\Delta t = 2 \dfrac{\gamma_o}{\sqrt{B}}$.

3.2.3 Stimulated Compton Scattering in a Time Varying Plasma

To model stimulated Compton scattering in a plasma with a time dependent density due to tunneling ionization, we start from the Vlasov equation (Krall and Trivelpiece 1973) to which we add a source term S(t) given by

$$\frac{\partial f}{\partial t} + v \cdot \nabla f - \left(\frac{e}{m} E + \frac{\nabla v_o \cdot v_1^*}{m} \right) \cdot \frac{\partial f}{\partial v} = S(v, t) \tag{3.27}$$

where

$$S(v, t) = w(t)(N - n)\delta(v) \tag{3.28}$$

The time evolution of the zeroth order distribution function is then determined by

$$\frac{\partial f_o}{\partial t} = -w(t)n_o \left(1 - \frac{N}{n_o} \right) \delta(v) \tag{3.29}$$

and the first order perturbation $\hat{f}$ satisfies the equation

$$\frac{\partial \hat{f}}{\partial t} + i\,\mathbf{k}\cdot\mathbf{v}\,f_1 - \left(\frac{e}{m}\mathbf{E} + i k\frac{\mathbf{v}_o\cdot\mathbf{v}_1^*}{m}\right)\cdot\frac{\partial f_o}{\partial \mathbf{v}} = 0 \tag{3.30}$$

Letting

$$\begin{cases} \tilde{f} = \hat{f}\,e^{ikx - i\int \omega\,dt} \\ \tilde{n} = \hat{n}\,e^{ikx - i\int \omega\,dt} \end{cases} \tag{3.31}$$

and applying a spatial and temporal Fourier transform to Eq. (3.30) we obtain

$$\hat{f} = i\left(\frac{e}{m}\mathbf{E} + i k\frac{\mathbf{v}_o\cdot\mathbf{v}_1^*}{m}\right)\frac{\dfrac{\partial f_o}{\partial \mathbf{v}}}{\omega - kv_x} \tag{3.32}$$

and, integrating with respect to v, we find the fluctuating density $\hat{n}$ to be given by

$$\hat{n} = i\frac{\mathbf{k}\,e}{km}\cdot\left(\mathbf{E} + \frac{i}{e}\mathbf{k}\cdot(\mathbf{v}_o\cdot\mathbf{v}_1^*)\right)\int \frac{\dfrac{\partial f_o}{\partial \mathbf{v}}}{\omega - kv_x}d^3v \tag{3.33}$$

We now define the plasma susceptibility χ_e as

$$\chi_e = \frac{4\pi\,e^2}{km}\int \frac{\partial_v f_o}{\omega - kv_x}dv \tag{3.34}$$

The time dependence of both the density and temperature are contained in the expression for χ_e through its dependence on f_o. Fourier transforming Poisson's equation [Eq.(3.10)] we get

$$\hat{n} = -i\frac{\mathbf{k}\cdot\mathbf{E}}{4\pi\,e} \tag{3.35}$$

and using Eqs.(3.11) and (3.34) we can rewrite Eq.(3.33) as

$$\hat{n} = -\frac{\chi_e}{1 + \chi_e}E_o A_1 E_1^* \tag{3.36}$$

where $A_1 = \dfrac{k^2}{4\pi\,m^2\omega_o\omega_1}$. In the weakly damped limit Eq.(3.16b) can be rewritten as

$$\partial_t E_1^* + \frac{v_1}{2} E_1^* = i \, \hat{n} E_o^* \omega_p^2$$

(3.37).

Finally, combining Eqs.(3.36) and (3.37) and integrating with respect to time we obtain

$$E_1^* = E_{10}^* \exp\left[-\int\left(\frac{v_1}{2} - iE_o^2 A_1 \omega_p^2 \frac{\chi_e}{1+\chi_e} \right) dt \right]$$

(3.38).

The density fluctuations will therefore have an amplification factor given by

$$\exp\left\{ \int\left[A_1 \omega_p^2 E_o^2 \operatorname{Im}\left(\frac{\chi_e}{1+\chi_e} \right) - \frac{v_1}{2} \right] dt \right\}$$

(3.39).

The integration has to be carried out up to a time which is the shorter of the laser pulse length and the time it takes for the light wave to convect from the location of the source (usually right hand boundary of the plasma) to the location of the observer. The convection velocity for the Compton waves can be neglected since these waves are heavily damped.

If the plasma conditions and pump are time independent then Eq.(3.39) reduces to the usual time independent Compton growth rate (Drake et al. 1974)

$$\gamma_C = 2\left(\frac{v_o}{c} \right)^2 \omega_o \operatorname{Im} \frac{\chi_e(\omega, k\lambda_{De})}{1 + \chi_e(\omega, k\lambda_{De})}$$

(3.40)

The associated spatial growth rate is then given by

$$\kappa_C = 2\left(\frac{v_o}{c} \right)^2 \frac{\omega_o}{c} \operatorname{Im} \frac{\chi_e(\omega, k\lambda_{De})}{1 + \chi_e(\omega, k\lambda_{De})}$$

(3.41)

3.2.4 Ionization Induced Refraction

Because the ionization rate [Eq.(3.2)] has a strong non-linear dependence on the applied field, a plasma with strong radial density gradients is formed when a Gaussian transverse intensity profile is used. This plasma can then act as a negative lens, refract

35

the laser beam which clamps the intensity close to the ionization threshold suppressing thereby further ionization.

A simple estimate for the scale lengths associated with refraction can be obtained as follows. In an inhomogeneous medium one can calculate the path taken by a light ray from the paraxial ray equation

$$d\theta = \frac{\partial}{\partial r} \frac{\Delta\eta}{} ds \tag{3.42}$$

where $\Delta\eta = \eta_{vac} - \eta_{med}$ with η_{vac} and η_{med} the index of refraction of vacuum and the medium respectively. The index of refraction for electromagnetic waves in an underdense plasma can be approximated as

$$\eta_p = \frac{ck}{\omega} = (1 - \omega_p^2/\omega^2)^{1/2} \approx 1 - \frac{1}{2}\frac{n(r)}{n_c} \tag{3.43}$$

where n_c is the critical density and $n(r)$ is the radial density profile.

Substituting Eq.(3.43) into Eq.(3.42) we obtain

$$d\theta = \frac{1}{2}\frac{\partial n/n_c}{\partial r} ds \tag{3.44}$$

The total bending angle after traveling a distance L is given by

$$\theta = \frac{1}{2}\int \frac{\partial(n/n_c)}{\partial r} ds \approx \frac{1}{2}\frac{L}{L_D}\frac{z_0}{w_0}\frac{n}{n_c} \tag{3.45}$$

where L is the path length normalized to z_0 and L_D is the density gradient scale length normalized to w_0.

We next derive a scaling law for intensity clamping due to refraction, by incorporating the paraxial ray equation into Gaussian beam optics. Initially, as the laser intensity increases above the ionization threshold, plasma will be produced in a small volume. Subsequent light rays entering the plasma and converging towards the focus will now be bent due to refraction. If the slope of the rays is zero, at the location were

3 6

the laser intensity is just below threshold, then further ionization will be prevented and the plasma density will cease to increase.

The intensity profile for a Gaussian beam is given by

$$I(s,\rho) = I_{peak} \frac{e^{-2\left(\frac{\rho}{v}\right)^2}}{v^2} \qquad (3.46)$$

where $v(s) = \frac{w(s)}{w_0} = (1 + s^2)^{1/2}$, $s = \frac{z}{z_0}$ and $\rho = \frac{r}{w_0}$ $\qquad (3.47)$

with w_0 the beam size at the waist, $2 z_0 = \frac{2\pi w_0^2}{\lambda}$ the Rayleigh range, λ the wavelength

of the laser and I_{peak} the peak laser intensity. The rate at which the intensity changes as a function of s is given by

$$\frac{\partial I(s,\rho)}{\partial s} = -2 I_{peak} \frac{e^{-2\left(\frac{\rho}{v}\right)^2}}{v^3} [1 - 2\left(\frac{\rho}{v}\right)^2] \frac{dv}{ds} \qquad (3.48)$$

and

$$\left(\frac{dv}{ds}\right)_{Gauss} = \frac{s}{\sqrt{1 + s^2}} \qquad (3.49)$$

Geometrically, $\left(\frac{dv}{ds}\right)_{Gauss}$ is just the beam convergence (for s<0) or expansion angle

(s>0) due to Gaussian focussing. Refraction is going to change the spot size by an amount

$$\left(\frac{dv}{ds}\right)_{Refrac} = \frac{z_0}{w_0} d\theta = \frac{1}{2} \left(\frac{z_0}{w_0}\right)^2 \frac{\partial(n/n_c)}{\partial \rho} ds \qquad (3.50)$$

Therefore the total rate of change of the spot size is proportional to

$$\left(\frac{dv}{ds}\right)_{Total} \equiv \left(\frac{dv}{ds}\right)_{Gauss} + \left(\frac{dv}{ds}\right)_{Refrac} \qquad (3.51)$$

The intensity remains constant, or reduces, when $(\frac{dv}{ds})_{Total} \geq 0$ which gives

$$n/n_c \, ds \geq 2 \left(\frac{w_o}{z_o}\right)^2 \frac{s L_D}{\sqrt{1 + s^2}} \qquad (3.52)$$

where ds is the path length in the plasma. Ionization will be suppressed if the rate of beam size change is larger than zero at a location $s = s_{thresh}$ where the intensity reaches the ionization threshold. In the absence of refraction, s_{thresh} is equal to [Eq.(3.47)]

$$s_{thresh} = \sqrt{\alpha - 1} \qquad (3.53)$$

where $\alpha = \frac{I_{peak}}{I_{thresh}}$. The radial density gradient scale length is roughly set by the width of the ionization threshold intensity contour. To find the maximum width of the ionization threshold contour we rewrite Eq.(3.46) as

$$\rho = v \sqrt{\frac{1}{2} \ln \left(\frac{\alpha}{v^2}\right)} \qquad (3.54)$$

and take the derivative with respect to s:

$$\frac{\partial \rho}{\partial s} = \frac{\partial v}{\partial s} \left\{ \sqrt{\frac{1}{2}\ln\left(\frac{\alpha}{v^2}\right)} - \frac{1}{\sqrt{\frac{1}{2}\ln\left(\frac{\alpha}{v^2}\right)}} \right\} = 0 \qquad (3.55)$$

Equation (3.55) is satisfied when $\frac{\partial v}{\partial s} = 0$, which is true for s=0 i.e. the beam waist location, or when $\frac{1}{2} \ln \left(\frac{\alpha}{v^2}\right) = 1$, which implies $v = \frac{\sqrt{\alpha}}{e}$. Therefore a second extremum is only possible when $v > 1$. The radial scale length L_D is then given by $L_D = \sqrt{\frac{1}{2} \ln \alpha}$ for $\alpha < e^2$ and $L_D = \frac{\sqrt{\alpha}}{e}$ for $\alpha > e^2$. Equation (3.52) then becomes

$$n/n_c \, ds \geq 2 \left(\frac{w_o}{z_o}\right)^2 \sqrt{\frac{\alpha-1}{2\alpha} \ln \alpha} \qquad \text{for } \alpha > e^2 \qquad (3.56)$$

3 8

and

$$n/n_C \ ds \geq 2 \ (\frac{w_0}{z_0})^2 \ \sqrt{\frac{\alpha-1}{e^2}} \qquad \text{for } \alpha > e^2 \qquad (3.57)$$

The path length ds after which refraction competes with the focusing of the beam depends on the experimental setup: for a static gas fill ds depends only on the laser intensity while for a gas jet both laser intensity and length of the gas target are important.
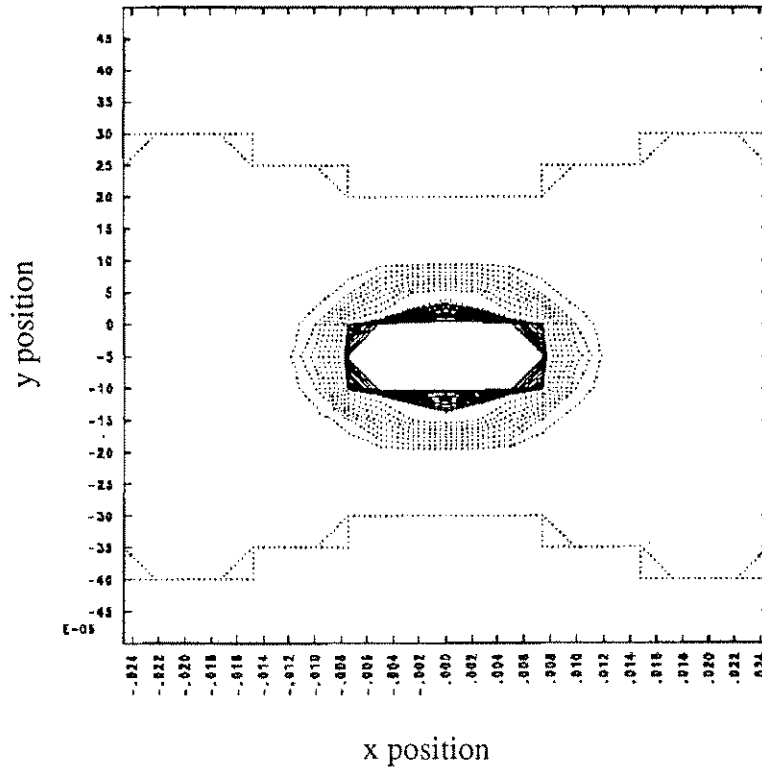
Figure 3.4: Plasma density contours for a CO_2-laser ($I_{peak} = 1.2 \times 10^{14}$ W/cm^2) produced plasma. The box goes from -3 z_0 to 3 z_0 in the horizontal direction and from -3 w_0 to 3 w_0 in the vertical direction. The highest density contour is 1 (normalized to the neutral gas density). The dashed contours increase by 10% while the solid contours increase by 1%. The total plasma length with $n/n_0 = 1$ is approximately z_R.

To estimate the path length for a static fill, we used a simple 2D code to calculate the density profile produced through ionization by a travelling laser pulse. Again, the ionization rate is given by Eqs.(3.1) and (3.2). The spatial beam profile is prescribed by

39

Gaussian optics and remains unchanged in the calculation. In Fig.(3.4) the density contours are shown for the case of a CO_2 - pulse ($I_{peak} = 1.2 \times 10^{14}$ W/cm^2) shot into hydrogen gas. It is found that for the CO_2 - case the plasma size is on the order of z_R while for the Nd-YAG case it is 16 z_R. In order for the intensity to be below the ionization threshold at the vacuum focus, the plasma needs to be dense enough along a path length of roughly 1/4 the size of the plasma.
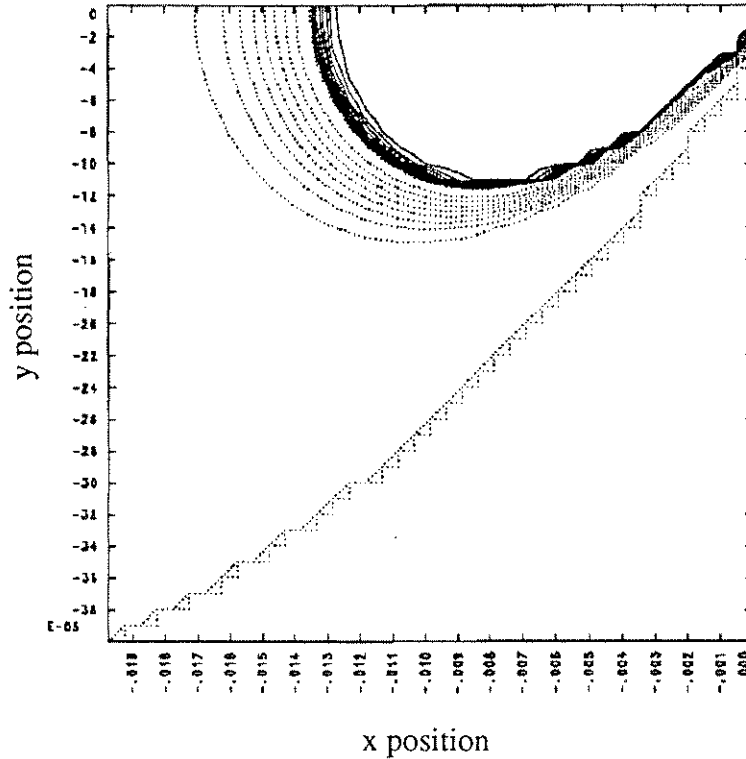
Figure 3.5: Plasma density contours for a YAG-laser ($I_{peak} = 2 \times 10^{17}$ W/cm^2) produced plasma. The box goes from -24 z_O to 0 in the horizontal direction and from -24 w_O to 0 in the vertical direction. The highest density contour is 1 (normalized to the neutral gas density). The dashed contours increase by 10% while the solid contours increase by 1%. The total plasma length at $n/n_O = 1$ is approximately 16 z_R.

Taking therefore ds to be on the order of $\dfrac{\text{Sthresh}}{2} z_O$ we finally obtain

$$n/n_c \leq \frac{4\lambda}{\pi z_o} \sqrt{\frac{\ln\alpha}{2\alpha}} \qquad\qquad \text{for } \alpha < e^2 \qquad\qquad\qquad (3.58)$$

and

$$n/n_c \leq \frac{4\lambda}{\pi e z_o} \qquad\qquad \text{for } \alpha > e^2 \qquad\qquad\qquad (3.59)$$

as the maximum plasma density that can be generated due to ionization induced refraction. It is obvious that reducing the length of gas through which the laser has to propagate will increase the maximum obtainable density.

3.3 Experiment

In the experiment, a CO_2-laser beam (up to 100 J, 150 ps rise time and 350 ps fall time) was focused into a vacuum chamber containing up to 5 Torr of Ar or H_2 gas. The measured spot size in vacuum was 2 $w_o = 340$ μm and the peak laser intensity in vacuum was around 3 x 10^{14} W/cm^2. At this intensity, an estimate based on Eq.(3.3) shows that, for fill pressures exceeding 1 mTorr, the space charge potential is large enough to confine most of the electrons against the ponderomotive potential of the laser. The space-charge dominated plasma was produced over approximately two Rayleigh lengths, 2 z_o, and was diagnosed by (a) viewing the forward laser harmonic emission; (b) collective Thomson scattering of a 0.5 μm beam to probe $2k_o$ density fluctuations; and (c) by measuring the X-ray emission from the plasma. Using the tunneling ionization rate equation [Eq.(3.1)] and neglecting any pump depletion, we found that in Ar-gas full ionization (to Z=1) is attained for our experimental parameters in approximately 25 ps once the threshold of 6 x 10^{13}W/cm^2 is exceeded. As in the case of single atoms (Yergeau et al. 1987, Corkum et al. 1989), no significant plasma

formation was detected either visually or on any of the above diagnostics, below an average laser intensity of 6 x 10^{13} W/cm^2. Above this threshold both line and continuum emission were observed but always in the recombination phase of the plasma, almost 5 ns after the laser pulse was over. This supports the notion that collisional excitation and ionization are relatively unimportant in our work.

3.3.1 Harmonic Generation

The evidence for plasma formation by tunneling comes from odd harmonic emission from the plasma. When linear polarization is used the ionization proceeds in stepwise fashion at twice the laser frequency generating a non-linear current $J(l\omega_0, l k_0) = -e \mathrm{v}\, n_e$, $l = 3,5,7,..$ which acts as a source term for odd harmonic emission (Brunel 1990). The frequency spectrum of the transmitted or forward scattered laser light was measured through bandpass filters. The energy in the second harmonic was measured using a spectrograph/pyro-array detector combination allowing a direct measurement of the line width of the radiation. The energy in other harmonics was measured through bandpass filters using a spectrograph and a liquid helium cooled Cu:Ge detector. The spectrum was found to contain discrete lines at the second ($\Delta\lambda/\lambda < 10^{-3}$), third ($\Delta\lambda/\lambda < 10^{-3}$) and fifth harmonic of the laser frequency [Fig.(3.6)].
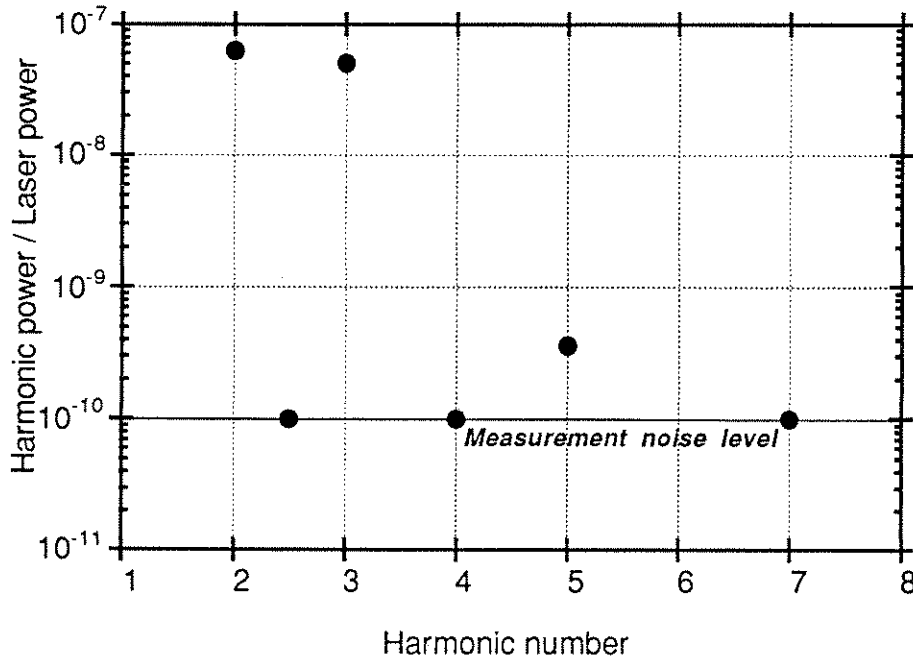
Figure 3.6: Ratio of harmonic power to laser power for different harmonic numbers. To convert the measured amount of energy into power we have assumed the light to be emitted in a 50ps long pulse for all the different harmonics.

In Fig.(3.7) the harmonic signal level as a function of the ellipticity α is plotted for the second and the third harmonic. As expected from the tunneling mechanism, the third and the fifth harmonic (not plotted) were found to decrease in magnitude as the ellipticity of the beam α was increased. The second harmonic signal however was found to be independent of polarization

Since the infra-red pulses could not be time resolved we can only put an upperbound on the pulse length τ_{pulse} needed to convert the measured amount of energy into power. If the harmonics were generated by the tunneling mechanism they will only be emitted during the time it takes to ionize the gas, i.e. $\tau_{pulse} \approx 10$ ps.

4 3
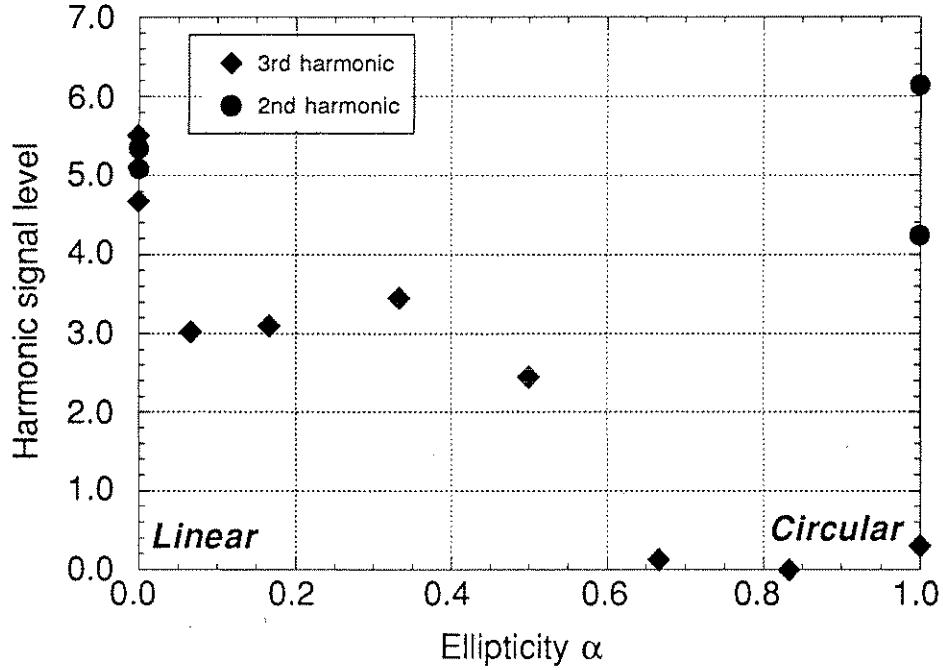
Figure 3.7: Measured second and third harmonic signal level as a function of the ellipticity α of the polarization of the ionizing laser beam.

The maximum theoretical efficiency P_{2r+1}/P_1 is given by (Brunel 1990)

$$\frac{P_{2r+1}}{P_1} = \frac{3\left(\frac{\omega_a}{\omega_o}\right)^2 \zeta \exp\left(-\frac{4}{3}\zeta\right)k_o^2}{\pi \ \ r^2(2r+1)^2}\left(\frac{\omega_{pg}}{\omega_o}\right)^4\left\{\exp(-3r^2\zeta)+\frac{r}{r+1}\exp\left[-3\left(\frac{r+1}{\zeta}\right)^2\right]\right\}^2 D \ (3.60)$$

where 2r+1 is the order of the harmonic, ω_{pg} is the plasma frequency at full ionization. The value for ζ is calculated using the laser field strength at the moment where the density is half its final value. For our experimental parameters the theoretical ratio P_3/P_1 was a factor of 5 above the measured value but the difference may be due to the uncertainty in the pulse length and in estimating the detuning factor D for a collimated beam

$$D = \frac{\sin^2(\Delta k L / 2)}{(\Delta k / 2)^2} \qquad (3.61)$$

since the length L of the medium is not well known. Here Δk is the wavevector mismatch between fundamental and third harmonic given by (Brunel 1990)

$$\Delta k = -rk_o \frac{\omega_p^2}{\omega_o^2} \qquad (3.62)$$

In addition to stepwise ionization, odd harmonics can be generated through the non-linear susceptibility $\chi^{(3)}$ of the media (Ward and New 1969) through which the laser beam propagates and through relativistic effects inside the plasma (Sprangle et al. 1990). Harmonic emission due to the $\chi^{(3)}$ process will follow the laser pulse while relativistic effects can only be important close to the peak of the pulse. The background signal level, with the chamber evacuated, can indeed be accounted for by non-linear processes in the NaCl windows and SF_6-gas (Weber 1982) which is used to suppress self-lasing. Although the beam traverses neutral gas inside the target chamber, it is well known that no third harmonic will be generated for a strongly focussing beam when the medium is infinitely long (Ward and New 1969). When the non-linear medium is finite in length but still much longer than Rayleigh range and extends symmetrically on both ends of best focus, the ratio P_3/P_1 is given by (Lehmeier et al. 1985)

$$\frac{P_3}{P_1} = \frac{\omega_3^2 |\chi^{(3)}|^2}{3^{3/2} n_3 n_1^3 c^4 \varepsilon_0^2} I_1^2 D \qquad (3.63)$$

Here $\chi^{(3)}$ is the non-linear third order susceptibility of the medium; n_1 and n_3 are the index of refraction of the medium at the fundamental and third harmonic respectively; ω_3 is the frequency of the third harmonic; b is the confocal parameter; z_b is the offset of the center of the non-linear medium with respect to the Gaussian beam waist position (z=0); and I_1 is the peak laser intensity. The detuning factor D for a Gaussian beam is given by

$$D = \left| \int_0^L \frac{1}{[1 + i\, 2\frac{(z_b + z)}{b}]^2}\, \exp(-i\Delta kz)dz \right|^2 \qquad (3.64)$$

In Fig.(3.8) we show the factor D as a function of the length of the medium, from which it is obvious that $\chi^{(3)}$ - effects are only becoming important when the Rayleigh range is longer than the length of the non-linear medium (e.g. in a gas-jet experiment).
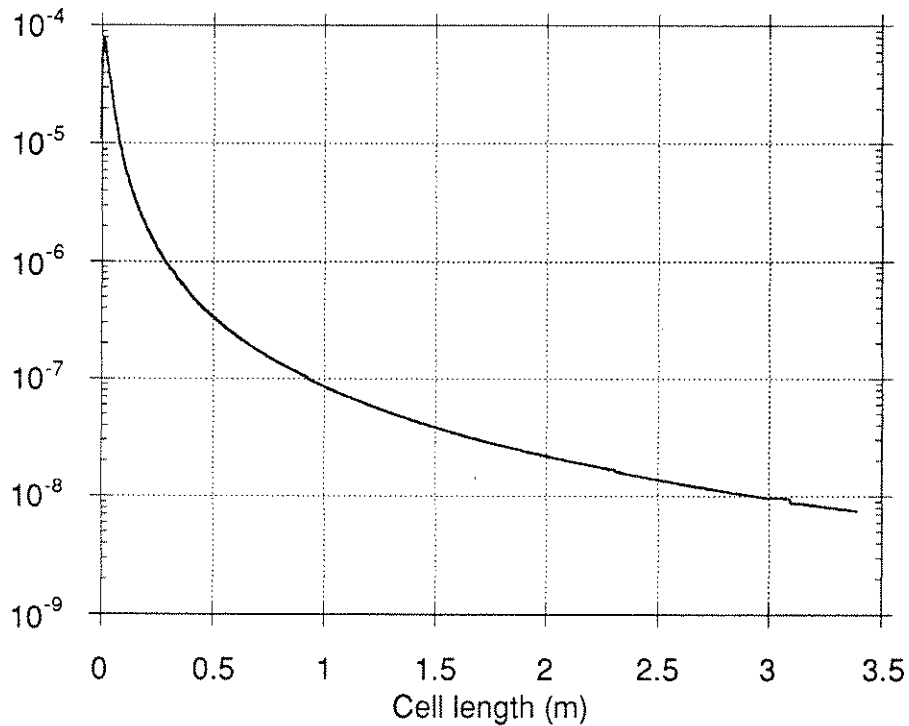
Figure 3.8: Detuning factor D for a Gaussian beam, using the parameters b = 1.7 cm, $\Delta k = 0.000115$ for argon gas @ 500 mTorr and $z_b = 0$.

The magnitude of $\chi^{(3)}$ was measured in argon gas at relatively low laser intensity ($I \leq 10^{11}$ W/cm^2) using a 1.06 µm YAG-laser, and atmospheric pressures (Lehmeier et al. 1985). To first order, $\chi^{(3)}$ and the indices of refraction n_1, n_3 can be extrapolated to other wavelengths and pressures using the relations given by Lehmeier et

al.. Since the laser enters the experiment as a collimated (i.e. Rayleigh range much longer than L), low intensity ($I<10^{11}$ W/cm^2) beam before being focused, the contribution to the third harmonic signal along this path is given by Eq.(3.63) where the detuning factor D is given by Eq.(3.61). For our experimental parameters we then obtain $P_3/P_1 = 1.04$ x 10^{-19} and $P_3/P_1 = 1.53$ x 10^{-13} as contributions of the high intensity focusing beam and the collimated beam respectively. Here we have taken a neutral argon gas density of 1.8 x 10^{16} atoms/cm^3 and a fundamental power P_1 of 100 GW. Even if we assume the harmonic emission to occur for the entire laser pulse, i.e. $\tau_{pulse} = 500$ ps, it is clear from Fig.(3.6) that the measured third harmonic efficiency is much higher than the theoretical contribution to harmonic generation due to $\chi^{(3)}$ in the neutral gas.

Relativistic effects are also unimportant for the parameter regime of this experiment. Using Sprangle et al.'s formalism (Sprangle et al. 1990) to calculate the efficiency of third harmonic generation we obtain (Mori 1991)

$$\frac{P_3}{P_1} = \left(\frac{3}{256}\right)^2 \left(\frac{\omega_p}{\omega_o}\right)^4 a_o^4 \left(1 + \frac{a_o^2}{2}\right)^{-3} \tag{3.65}$$

Here a_o is equal to v_{osc}/c. As shown in Fig.(3.9) the calculated efficiency is more than 6 orders of magnitude below the measured level, and therefore this can also not explain our observations. Furthermore, the theoretical ratio of fifth and third harmonic power scales roughly like third to fundamental which is in even larger discrepancy with the measured efficiency for the fifth harmonic. Both of these effects are therefore relatively unimportant in our experiment.
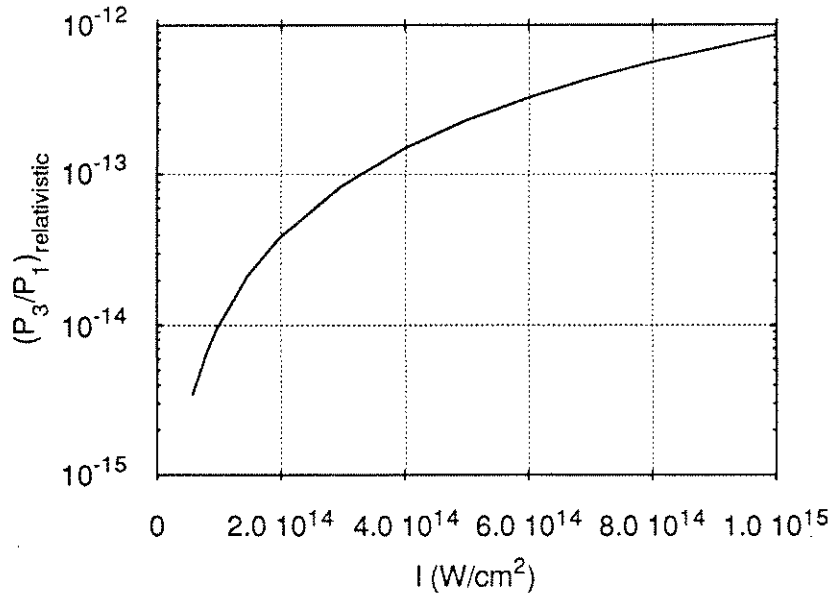
Figure 3.9: Theoretical efficiency of third harmonic generation as calculated from Eq.(10). The plasma density was assumed to be 10^{-3} n_c.

The second harmonic emission, observed in the experiment was found to be nearly independent of polarization, but cannot be explained by any of the above mechanisms. Simulations show that the second harmonic emission originates from the edges of the plasma, where the density gradients are the steepest, suggesting that the source for the even harmonics is the non-linear current $J_2 = -en_e v_2 = -\dfrac{1}{4}\dfrac{e^2}{m\omega}n_e \nabla E^2$

(Meyer and Zhu 1987).

3.3.2 Time Resolved Thomson Scattering

Our main density and $T_{\parallel}$ diagnostic is based on the detection of electron density fluctuations with $k_p = 2 k_0$ excited by the laser beam through either stimulated Raman (SRS) (Walsh et al. 1984) or Compton (SCS) (Leemans et al. 1991a) scattering. If the

48

tunnel plasmas have very low values of $T_{\parallel}$ as the single particle model suggests, then $k\lambda_D \ll 1$ and SRS should have a very large growth rate, whereas for large $T_{\parallel}$ and $k\lambda_D$ on the order of 1, SCS may occur. Here λ_D is the usual plasma Debye length. The scattered light from $2\,k_0$ density fluctuations was wavelength (0.2 Å resolution) and time resolved (10 ps resolution) with a spectrograph/streak camera combination. However, it is not possible to follow the time evolution of the ionization process using this technique since the ionization rate is comparable to the homogeneous, time independent growth rate for the Raman/Compton instability (Drake et al. 1974). In Section 3.2.3 it was found that the homogeneous growth rate for SRS γ_0 is effectively reduced to $\gamma_{\textit{eff}} = \dfrac{\gamma_o}{\sqrt{B}}$ and that the growth time is limited by the smaller of the convection time or the "detuning time" $\Delta t = 2\dfrac{\gamma_o}{\sqrt{B}}$. Here B is the rate with which the plasma frequency varies as a function of time. For our experimental conditions the amplification factor for the Raman instability equals two e-foldings of gain, which is below our detection threshold.

Experiments show that the high frequency density fluctuations have a broad frequency spectrum consistent with Compton rather than Raman scattering. The evolution of one such spectrum from a plasma produced in a static fill of 1.1 Torr of Argon is depicted in Fig.(3.10a). At early times [Fig.(3.10b)], the spectrum can be fitted quite well applying the stimulated Compton scattering theory (Drake et al. 1974). In this second phase of the interaction of the laser with the plasma we assume that the density and temperature are evolving on a slow enough time scale justifying the use of the time independent growth rate for the stimulated Compton scattering instability. The fitting procedure is similar to the one described and used in Section 2.2.. Fitting the theoretical spectrum [Eqs.(2.2)-(2.4)] to the first line-out from Fig.(3.10b) gives $n \approx 6 \times 10^{15}\,cm^{-3}$ and $T_{\parallel} \approx 75$ eV [Fig.(3.11)]. This temperature is already much higher and
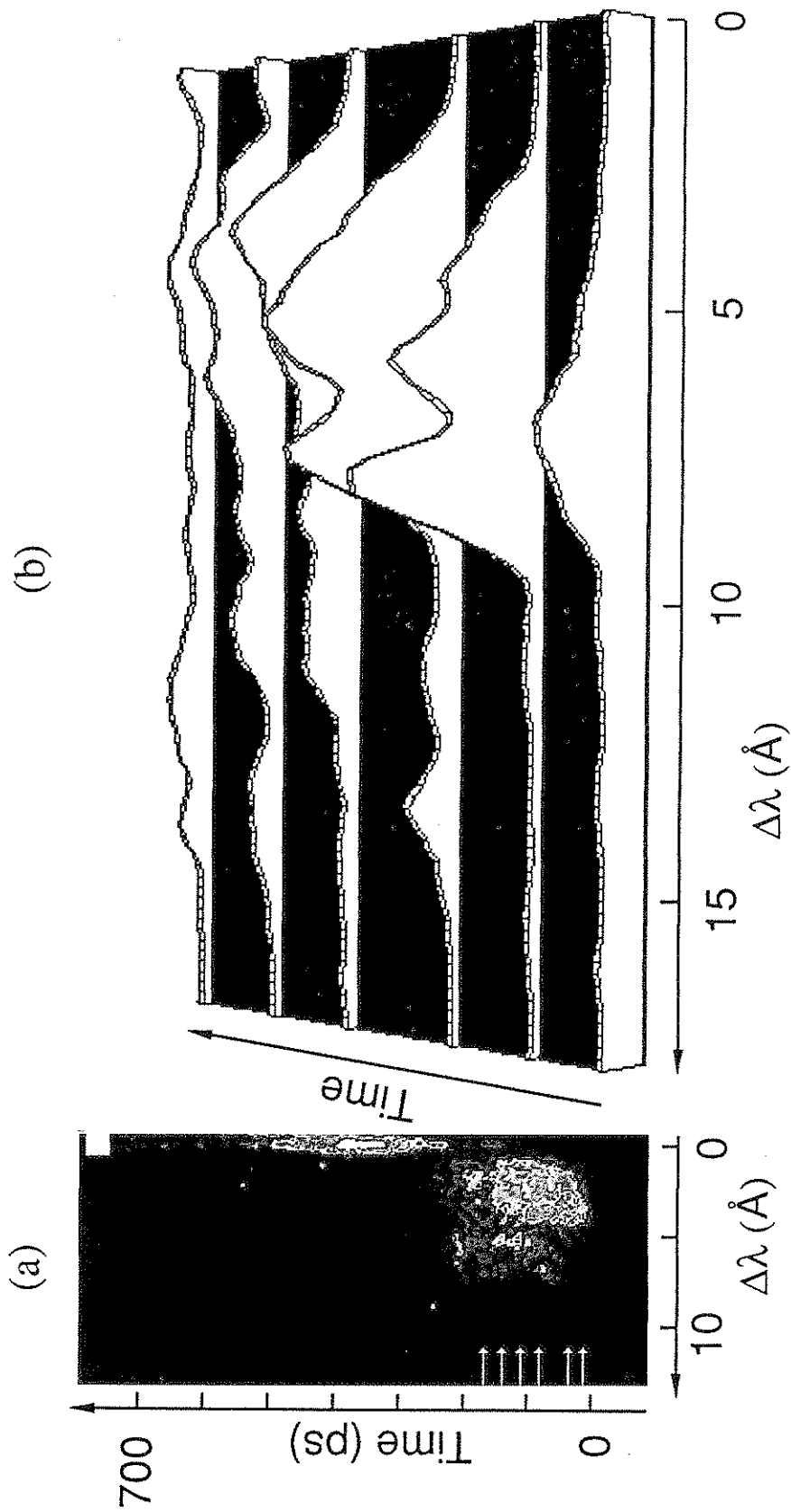
Figure 3.10: (a) Streak camera image of the Thomson scattered probe beam in a hydrogen plasma. The fill pressure was 1 Torr. Although not shown here, there was no blue shifted spectral feature visible in the original data. The white bar at the top indicates the location of a 100x attenuator for SBS. (b) Line-outs of the streak data taken along the direction of the arrows in (a).

the density much lower than that predicted by the single particle model. At later times the spectrum develops structure and broadens to both higher and lower frequencies. Applying the same fitting procedure at these times does not result in a good fit to the data [Fig.(3.11)].
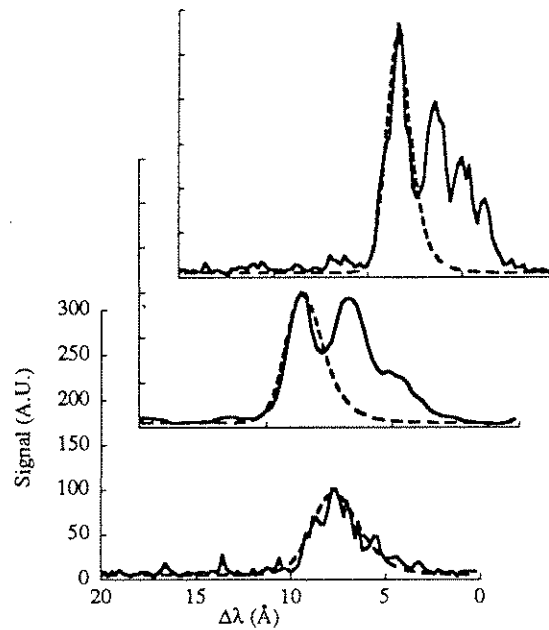
Figure 3.11: Plot of first three line-outs and fitted curves calculated by using convective amplification of thermal fluctuations through the stimulated Compton scattering instability [Eqs(2.2)-(2.4)].

About 140 ps after the onset of SCS, the spectrum resembles incoherent Thomson scattering from a thermal plasma rather than from a collective mode. These are still driven fluctuations (albeit in the strongly driven regime) as evidenced from the absence

51

of scattered light on the blue side. The most probable cause of the frequency broadening of the spectrum is a continued increase of $T_\parallel$ of the plasma. As will be seen later, this is believed to be due to the Weibel instability. Even at higher fill pressures, the SCS spectra indicated very low peak densities with $n \le 10^{-3} \ n_c$. At these low densities, collisional processes should be relatively unimportant on the time scales of the laser pulse. Also, at the higher pressures a significant amount of the laser energy was found to be refracted out of the original cone angle of the laser beam, which will be discussed in Section 3.3.4.

As an independent density diagnostic we have also attempted to excite a plasma wave using a laser beam containing two different frequencies. This process is known as beat wave excitation (Rosenbluth and Liu 1972, Tajima and Dawson 1979) and relies on
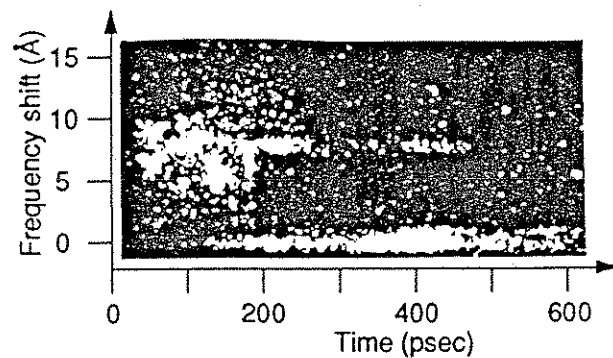
Figure 3.12: Time-resolved frequency spectrum of 2 k_0 electron density fluctuations. Wavelength shift increases upwards and time increases to the right. The feature near zero shift is from ion waves. The electron plasma wave feature due to SCS ranges from 0-15 Å. The feature at around 8 Å is the beat wave response of the plasma. The laser beam contained a 10.3 μm and a 10.6 μm line requiring a resonant density of $8 \times 10^{15} \ cm^{-3}$.

the fact that if the difference frequency of the two laser lines is close to the plasma frequency a plasma wave will be resonantly excited. When the CO_2 - laser was made to oscillate simultaneously on a 10.6 μm and a 10.3 μm line, requiring a plasma density on the order of 8 x 10^{15} cm^3, a signature of the long wavelength plasma wave mode-coupled to an SBS excited ion wave (Darrow et al. 1986) was seen on the Thomson scattering diagnostic [Fig.(3.12)]. However, when using the line pair 10.6 μm-9.6 μm which requires a plasma density of 1.2 x 10^{17} cm^{-3}, this feature was never seen. This confirms independently that the density is much lower than 10^{17} cm^{-3}.

We also explored the possibility of laser-plasma instability control by varying the polarization of the laser beam. The main effect of changing the laser polarization is to drastically alter the initial transverse distribution of electron energies. If these distributions isotropize rapidly then $k\lambda_D$, and therefore the damping rate for high frequency electron fluctuations, can be varied. As we increased α the fluctuations due to stimulated Brillouin scattering (SBS) were unaffected whereas the high frequency fluctuations became weaker and were eventually completely suppressed for $\alpha \geq 0.6$ [Fig.(3.9)]. These observations are consistent with an increase in $T_{\parallel}$ in going from linear to circularly polarized light. However, the inferred values for $T_{\parallel}$ are still anomalously higher than the single-particle predictions.
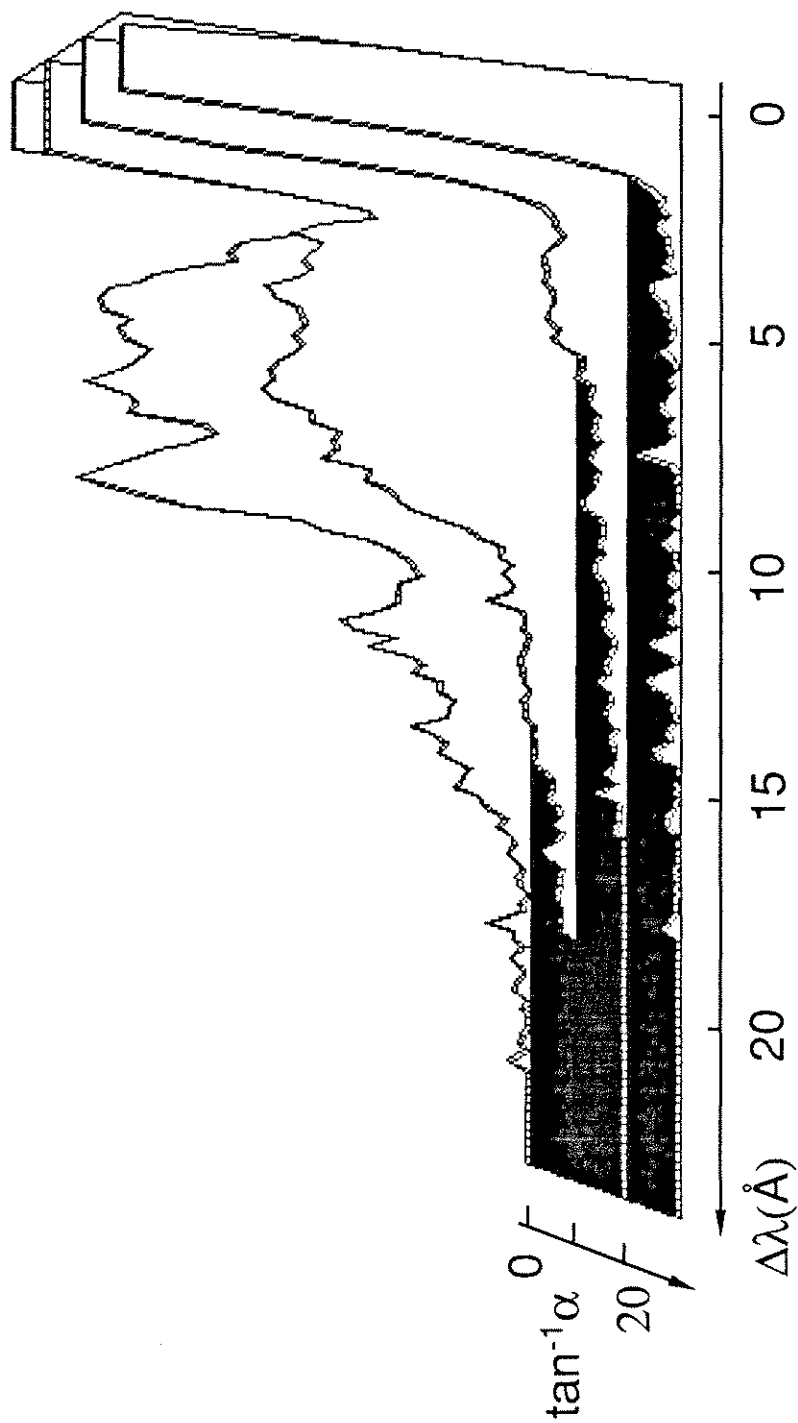
Figure 3.13: Time integrated streak camera images of the Thomson -scattered probe beam in hydrogen plasmas (fill pressure of 1 Torr) for different degrees of ellipticity α of the laser polarization ($\tan^{-1}\alpha = 45$ for circular polarization).

3.3.3 X-ray Emission

To obtain an independent estimate of the plasma temperature and to explore the possibility of plasma temperature control through polarization of the ionizing laser light, soft X-ray emission above 800 eV was measured using a silicon surface barrier detector with Be and Mylar filters. Figure (3.14) shows three sets of data: linear polarization with the detector looking (i) along and (ii) transverse to the electric field, and (iii) circular polarization. A significant difference in X-ray flux was seen between linear and circular polarization, as expected from the tunnel-ionization model. However, no significant difference was seen between looking transverse and along the electric field for the linear polarization.
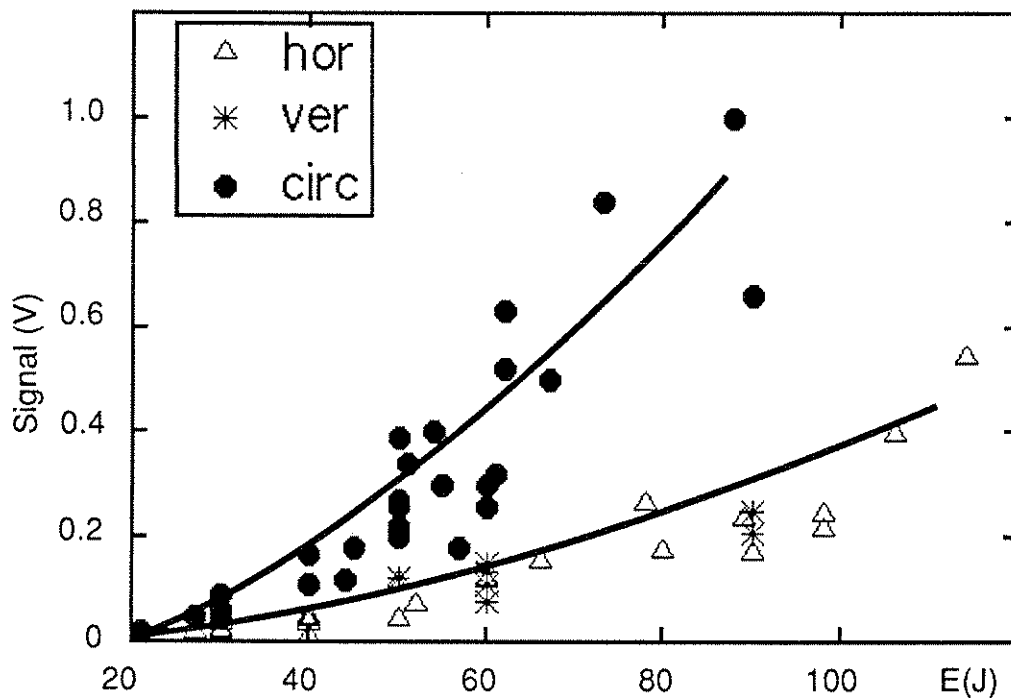
Figure 3.14: The X-ray emission from argon plasmas (fill pressure of 280 mTorr), as a function of laser energy for different polarizations.

To model the X-ray data we have assumed that the X-rays are emitted by an isotropized Maxwellian, for both linear and circular polarization. The spectral distribution of the Bremsstrahlung intensity from a Maxwellian distribution is given by (Shkarofsky et al. 1966)

$$S(\omega) = n \, S_O \, e^{-\frac{h\omega}{KT}} G \qquad (3.66)$$

with

$$nS_0 = \frac{n_+ nZ^2}{m^2 c^3} \left(\frac{e^2}{4\pi\varepsilon_o} \right)^3 \frac{16}{3} \left(\frac{2\pi m}{3KT} \right)^{\frac{1}{2}} \qquad (3.67)$$

and G is the Maxwell averaged Gaunt factor. The increase of X-ray flux with laser energy can simply be attributed to the increase of plasma volume at higher laser intensity. As seen from Eq.(3.67) the X-ray emission is proportional to the amount of ions and electrons. Using a 2D numerical ionization code we calculated the amount of electrons and ions produced through ionization for different laser intensities. The result is shown in Figs.(3.15) and (3.16).
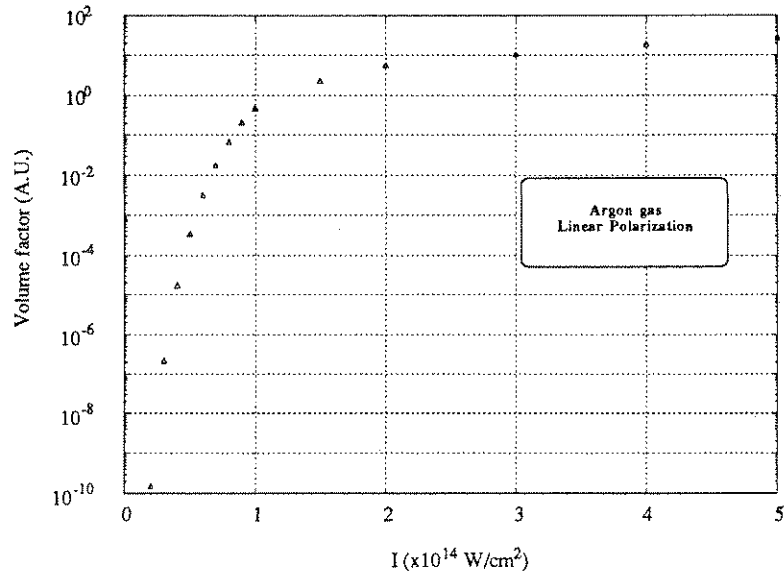
Figure 3.15: Calculated volume factor as a function of laser intensity for calculating X-ray yield from an argon plasma produced with a linearly polarized beam.
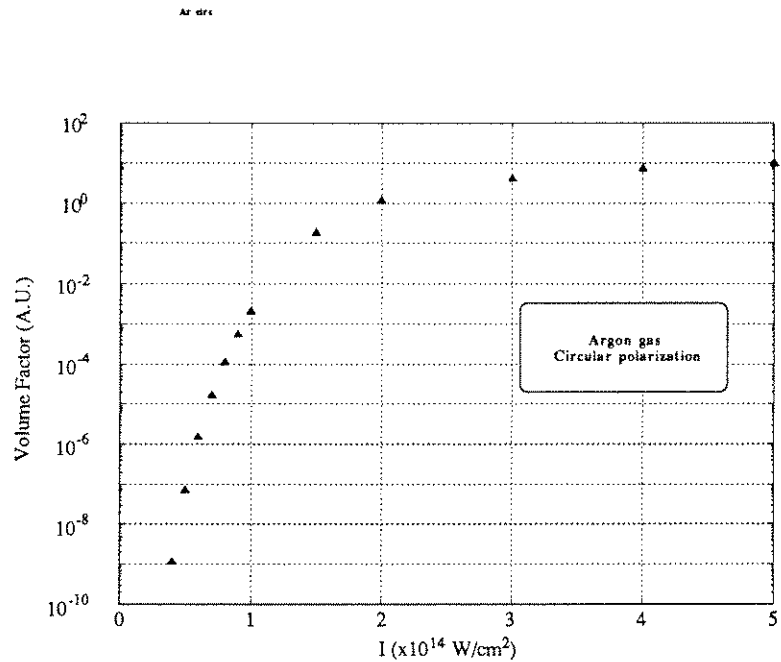
Figure 3.16: Calculated volume factor as a function of laser intensity for calculating X-ray yield from an argon plasma produced with a circularly polarized beam.

Taking this factor into account for the experimental data we found the X-ray signal to become independent of laser energy as shown in Fig.(3.17). The spread in the data for circular polarization is mainly due to the uncertainty in the peak laser intensity. Since the exact pulse shape varies from shot to shot and a low intensity pedestal can be present, an uncertainty in the peak laser intensity is introduced when converting the measured energy to power. As seen in Fig.(3.11b) the slope of the volume factor curve for circular polarization is very steep in the range of 1 to 2 x 10^{14} W/cm^2 thereby magnifying the uncertainty in the X-ray yield.
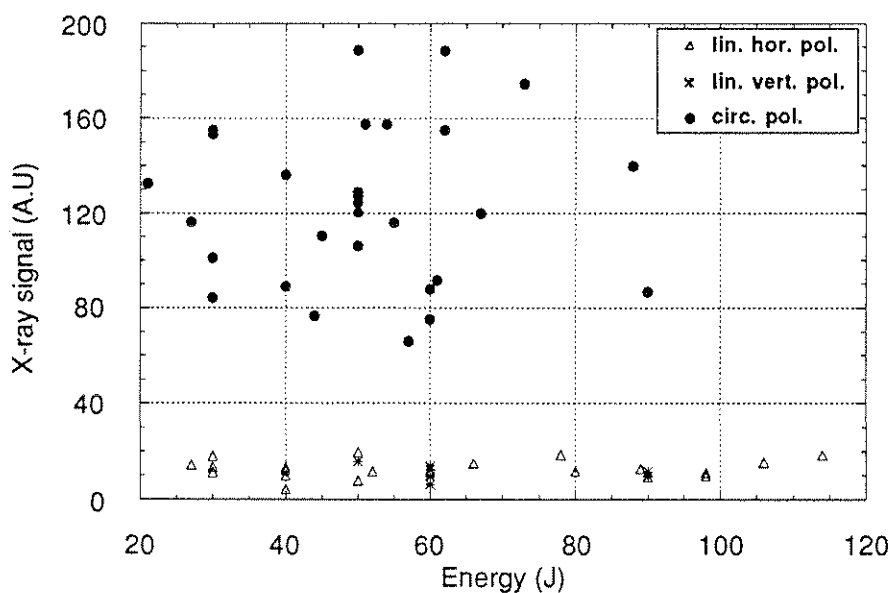
Figure 3.17: X-ray yield adjusted for the volume factor as a function of laser energy for linear polarization (detector looking horizontally and vertically) and circular polarization.

The Bremsstrahlung-spectrum from a Maxwellian plasma, with T as parameter, is then multiplied by the filter transmission spectra and the detector sensitivity curve. Integrating the resulting spectra gives the total amount of energy captured by the SSB-

detector. Experimentally we measured the X-ray flux through two different filter combinations (25 μm Be only and 25μm Be plus 6.3 μm Mylar foil), keeping the laser energy and gas pressure constant. From the ratio of the x-ray yield for the two filters we obtain a plasma temperature for circular polarization of around 450±150 eV. Plasmas produced with a linearly polarized laser produced on average ten times less signal (taking the volume factor into account) so that their temperature is typically about 180±50 eV. These temperatures are within a factor of two with what might be expected from a laser beam which has it's intensity clamped close to the ionization threshold due to refraction.

3.3.4 Ionization Induced Refraction

The clamping of the maximum density due to refraction was investigated by measuring the amount of laser light outside the original cone angle of the beam, as a function of fill pressure [Fig.(3.18)]. In Ar, as the fill pressure was raised beyond 200 mT, a sudden onset of refraction was seen. This corresponds to a density of around 0.7 $\times$ 10^{16} cm^{-3}. In H_2 refraction was found to be a more gradual function of pressure. On the laser pulse time scale the Ar ions are relatively immobile and the radial density gradients are "frozen-in", whereas in H^+ plasmas the ions can radially move during the laser pulse and relax the density gradients and thus reduce the defocusing. This conjecture was supported by the observation that the refraction effects could be reduced by using circularly polarized light (presumably higher $T_\perp$) instead of linearly polarized light [Fig.(3.19)].
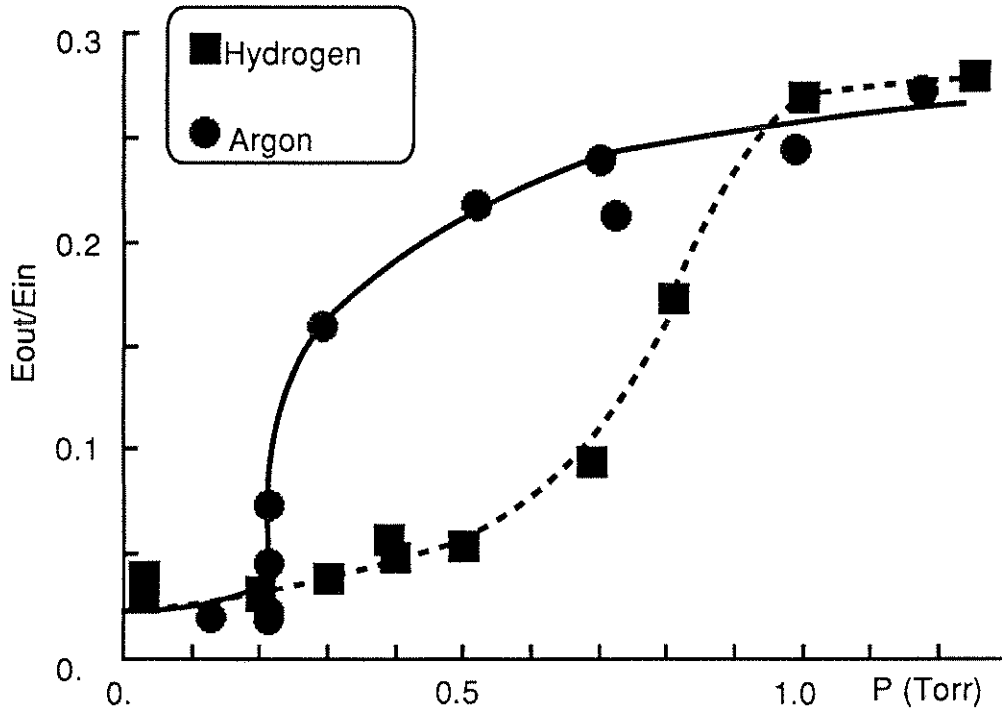
Figure 3.18: Ratio of the laser energy refracted outside of the original cone angle of the beam to the incident laser energy, in H_2 and in Ar plasmas, as a function of neutral gas fill pressure. The energies are measured by two cross calibrated calorimeters. The saturation of the refracted energy at 30% of the incident laser energy is consistent with the solid angle of detection of the calorimeter measuring the refracted beam energy.

In the experiment the ratio α of laser intensity to threshold intensity was varied from 2 to 10, 2 z_0 = 1.7 cm and 2 w_0 = 340 μm. Using Eq.(3.56) we obtain n/n_c ds $\geq$ 3 x 10^{-4} (8 x 10^{-4}) for α = 2 (10). From the density scaling law [Eq.(3.58)] we find that the maximum obtainable density for our experimental conditions is below 1.3 x 10^{-3} n_c which is in good agreement with the experimental observations.
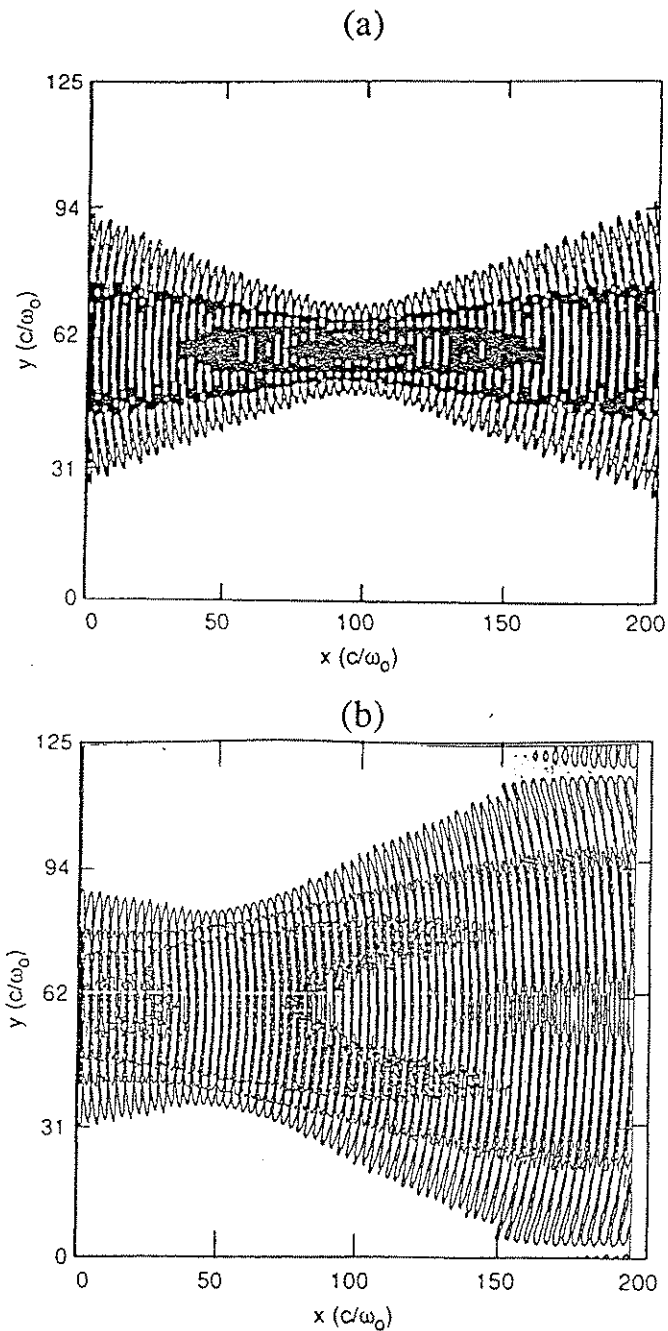
Figure 3.20 a,b: Contour plot of the transverse E_z - field from a WAVE-simulation. The simulation box is (200 c/ω_0 x 125 c/ω_0). The incident laser field is launched from the left-hand boundary into vacuum. In (a) the beam propagates in vacuum and is focused into the middle of the box. In (b) the beam propagates through a plasma with peak density of 0.1 n_c and is strongly refracted. The plane of highest intensity has moved backwards. Notice also that at x = 150 the E-field peaks of axis.
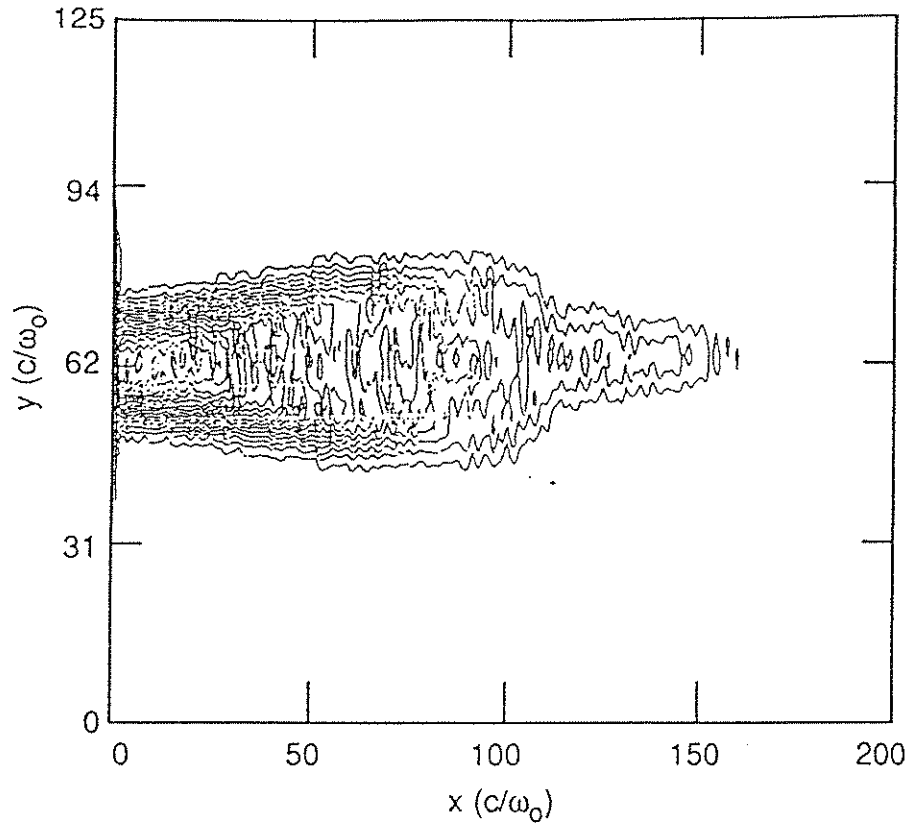
Figure 3.21: Calculated plasma density contours at $T = 900 \, \omega_0^{-1}$ using the PIC-code WAVE. The peak density equals $n/n_c = 0.1$. The box is (200 c/ω_0 x 125 c/ω_0). Notice how the location of the plasma is not centered on the box.
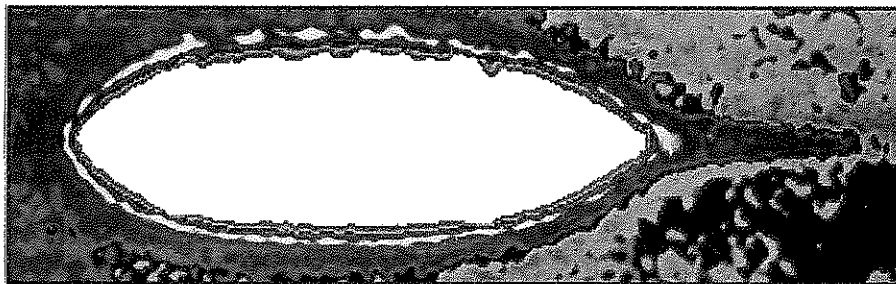
1 mm

Figure 3.22: CCD camera image of the visible radiation given off by the plasma. The colors are artificial and denote different intensities.

As seen in Figs.(3.20)-(3.21), rays entering the simulation box at $y = 72$ c/ω_0 (edge of plasma) make an angle of about 0.22 rad; the radial density gradient scale length is approximately 10 c/ω_0 and the peak density is $0.1 \frac{n}{n_c}$. From Eq.(3.45) we then find that the ray propagates parallel to the axes after a distance $L \approx 44$ c/ω_0 which agrees remarkably well with the simulation.

To verify the scaling law for the density clamping due to refraction we carried out a simulation in which the laser intensity was chosen so that the density should stay below 0.9 n_0, where n_0 is the neutral gas density. The peak density was found to be 0.92 n_0 which is in good agreement with the prediction from Eq.(3.58).

3.4.2 Stochastic Heating

To understand the origin of the initial $T_{||}$ and its further increase with time, simulations were carried out using WAVE. Simulations were designed to isolate the roles of parametric instabilities, space charge effects and refraction, and the Weibel instability (Weibel 1959). In all cases a circularly polarized beam was launched from the left hand boundary with a peak $v_{osc}/c = 0.1$, where v_{osc} is the oscillatory velocity of the electron in the laser field. The laser propagates in the x-direction. Time is normalized to ω_0^{-1} and space to c/ω_0. When a new electron and ion are created they are injected with an isotropic velocity of 10^{-5} c. For extremely low densities, $n/n_c = 10^{-8}$, the electron distribution functions obtained were in excellent agreement with those expected from the single particle model [Fig.(3.23 a,b)].
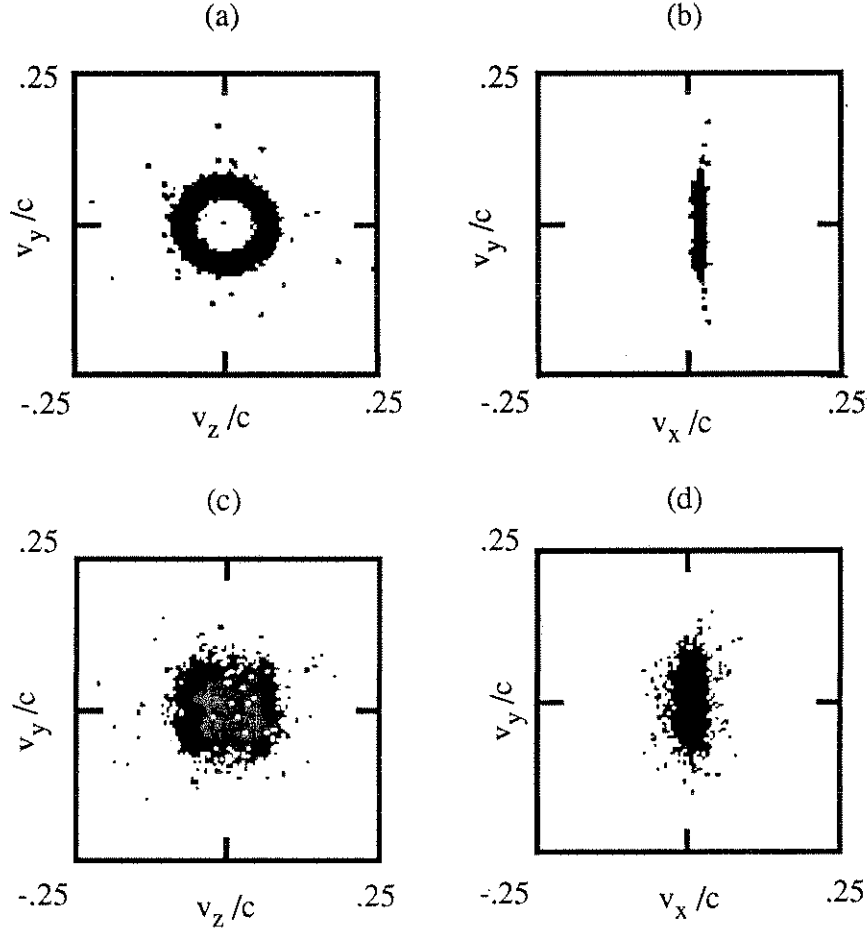
Figure 3.23: Transverse (v_y, v_z) and longitudinal (v_y, v_x) velocity space without [(a) and (b)] and with "plasma" effects [(c) and (d)]. In (a) and (b) the simulation was done on a 1D grid. The maximum density was $n/n_c = 10^{-8}$. The laser rise and fall time was 500 ω_0^{-1}. The major (minor) radius of the ring corresponds to a "temperature" of 1 keV (20 eV). In (c) and (d) the simulation was done on a 2D grid (200 c/ω_0 x 125 c/ω_0). The peak density was 4×10^{-4} n_c. The laser beam was collimated and had a Gaussian transverse profile with a beam diameter of 30 c/ω_0. The peak field strength corresponded to 0.1 v_{osc}/c for both the 1D and 2D simulation. The transverse (longitudinal) temperature at T=1200 ω_0^{-1} is $\approx$ 500 eV (50 eV).

Simulations with a fully ionized density of 10^{-2} n_c and a laser rise time of 750 ω_0^{-1} were done to isolate the high frequency instabilities (SRS/SCS). In 1D, SRS was seen to grow to large levels ($\delta n/n = 0.3$) because of a very low initial $T_{\parallel}$ ($k\lambda_D \ll 1$), and saturate due to particle trapping. The incident and backscattered ω-spectrum is shown in Fig.(3.24).

(a)

ω mode number

(b)

ω mode number
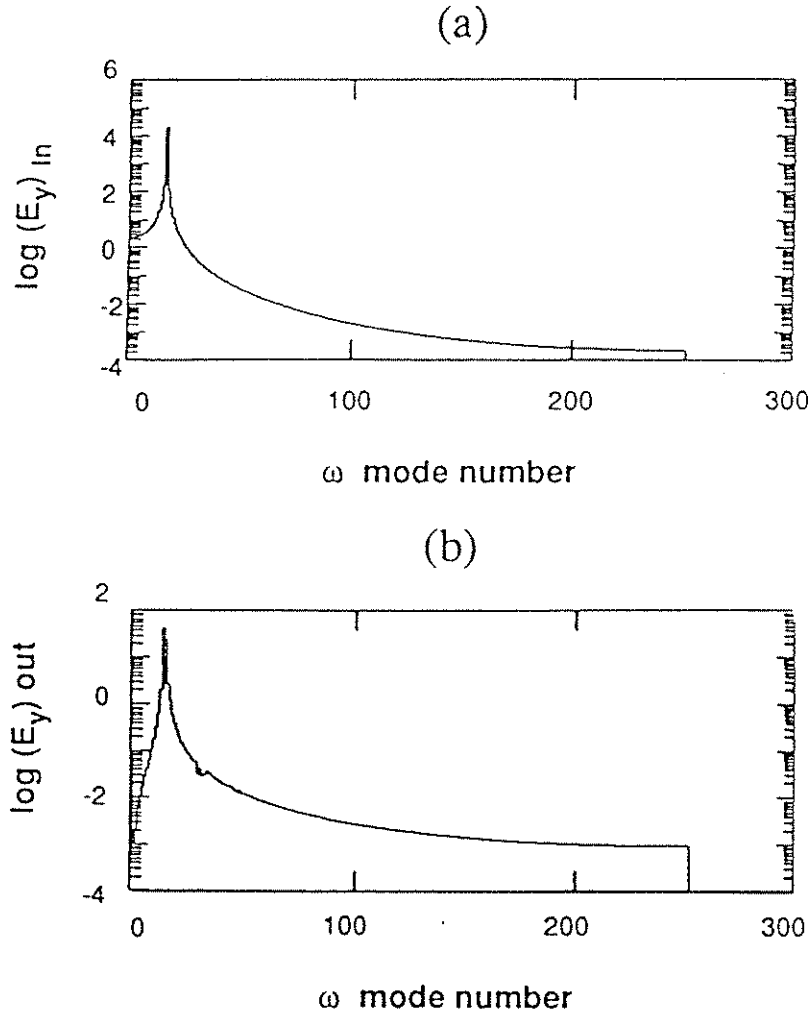
Figure 3.24: (a) ω spectrum of the incident electric field component E_y for a 1-D simulation. The plasma density at the end of the ionization was 10^{-2} n_c. The incident field strength was equivalent to $v_{osc}/c = 0.2$. (b) ω-spectrum of the backscattered electric field component E_y showing a narrow feature shifted by ω_{BG} [Eq.(2.1)].

In 2D however, where the beam was focused into the middle of the simulation box, SRS was suppressed because $T_{\parallel}$ at the end of the ionization was already large. Instead SCS occurred at a reduced level, consistent with experimental observations. This is shown in Fig.(3.25).

(a)

ω mode number

(b)

ω mode number
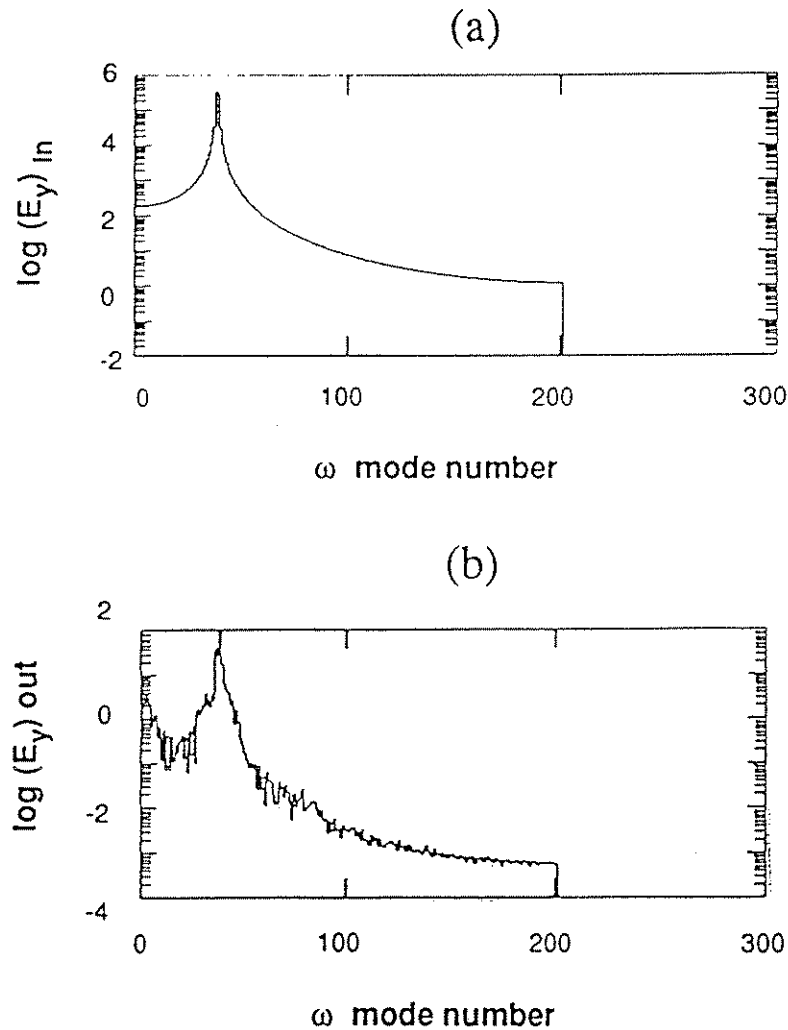
Figure 3.25: (a) ω spectrum of the incident electric field component E_y for a 2-D simulation. The plasma density at the end of the ionization was $4 \times 10^{-2} \, n_c$. The incident field strength was equivalent to $v_{osc}/c = 0.2$. (b) ω-spectrum of the backscattered electric field component E_y showing a broad spectral feature in contrast with the spectrum of Fig.(3.24).

A possible explanation for this high $T_\parallel$ at that time is that the electrons are born at positions where electric fields, for small f-number focusing and/or strong refraction, have a substantial longitudinal component. This in turn results in a significant longitudinal drift velocity component (i.e. $T_\parallel$) of the electrons. The variation of the field strength will result in broadening of the drift velocity distribution since particles born at different radial locations will end up with a different drift velocity. In addition, the electrons, retained by the ion space charge, continue to interact with both the applied electromagnetic fields and the space charge fields. Their phase averaged guiding center energy can increase in a stochastic fashion (Forslund et al. 1985, Bardsley et al. 1989, Mendonça 1985) leading to hotter plasmas with $T_\parallel$ scaling roughly as $mc^2\left(\frac{v_{osc}}{c}\right)^4$. In a 2D simulation with $n/n_c = 4 \times 10^{-4}$, too low for the parametric instabilities or refraction to occur, it was indeed found that at the end of the laser pulse, the plasma had a higher than expected $T_\parallel$ (50 eV vs 2 eV in the 1D computations) [Fig.(3.23 c,d)]. When the density was increased to $n/n_c = 0.1$, strong refraction of the beam was observed with the beam waist moving towards the laser leading to further stochastic heating.

3.4.3 Weibel Instability

To explain the further increase with time of $T_\parallel$ we considered the effect of the isotropization of the transverse distributions through the Weibel instability. Although it can be shown that the obtained distribution functions are stable to electrostatic perturbations along the x-direction using the Penrose criterion (Krall and Trivelpiece 1973), they are unstable to electromagnetic perturbations.In the previous section we

found that the transverse distribution function in a space-charge dominated plasma is much more filled in than the 1-D ring distribution obtained in the single particle regime. We will therefore use the expression for the maximum theoretical growth rate for the Weibel instability in a bi-maxwellian plasma, given by (Krall and Trivelpiece 1973)

$$\gamma_{Weibel} = \left(\frac{8}{27\pi}\right)^{1/2} \omega_p \left(\frac{kT_\parallel}{mc^2}\right)^{1/2} \frac{T_\parallel}{T_\perp}\left[\frac{T_\perp}{T_\parallel}-1\right]^{3/2} \tag{3.69}$$

The mode of the magnetic field with the maximum growth rate has a wavenumber k_B given by (Krall and Trivelpiece 1973)

$$k_B = \frac{\sqrt{3}}{3}\frac{\omega_p}{c}\left(\frac{T_\perp}{T_\parallel}-1\right)^{3/2} \tag{3.70}$$

The electron cyclotron frequency ω_{ce} corresponding to the saturation value of the magnetic field for the mode with the maximum growth rate, is given by (Estabrook 1978)

$$\omega_{ce} = 4\sqrt{\frac{3}{2}}\left(\frac{\gamma_{Weibel}}{\omega_p}\right)^2 \omega_p \tag{3.71}$$

In Fig.(3.26) we show the theoretical Weibel instability growth rate [Eq.(3.69)] as a function of $T_\perp$. In calculating this growth rate we have used the assumption from the tunneling model that the transverse drift velocities (v_y, v_z) and the longitudinal drift velocity $v_\parallel$ (and hence $T_\parallel$ and $T_\perp$) are related through

$$v_\parallel = \frac{v_y^2 + v_z^2}{2} \tag{3.72}$$

The isotropization of the electron distribution functions due to the Weibel instability was isolated by running a 1D simulation with $n/n_c = 5 \times 10^{-3}$ and a short laser pulse (1000 ω_0^{-1}) to suppress parametric instabilities. Both the measured growth rate of the long scale length magnetic field characteristic of the Weibel instability and the wavenumber of the mode were in reasonable agreement with the theoretical predictions

of $\gamma \approx 2 \times 10^{-3}\ \omega_O$ and $k_B \approx 0.2\ \omega_0/c$ respectively. The k-spectrum of the B_y component of the magnetic field is shown in Fig.(3.27).
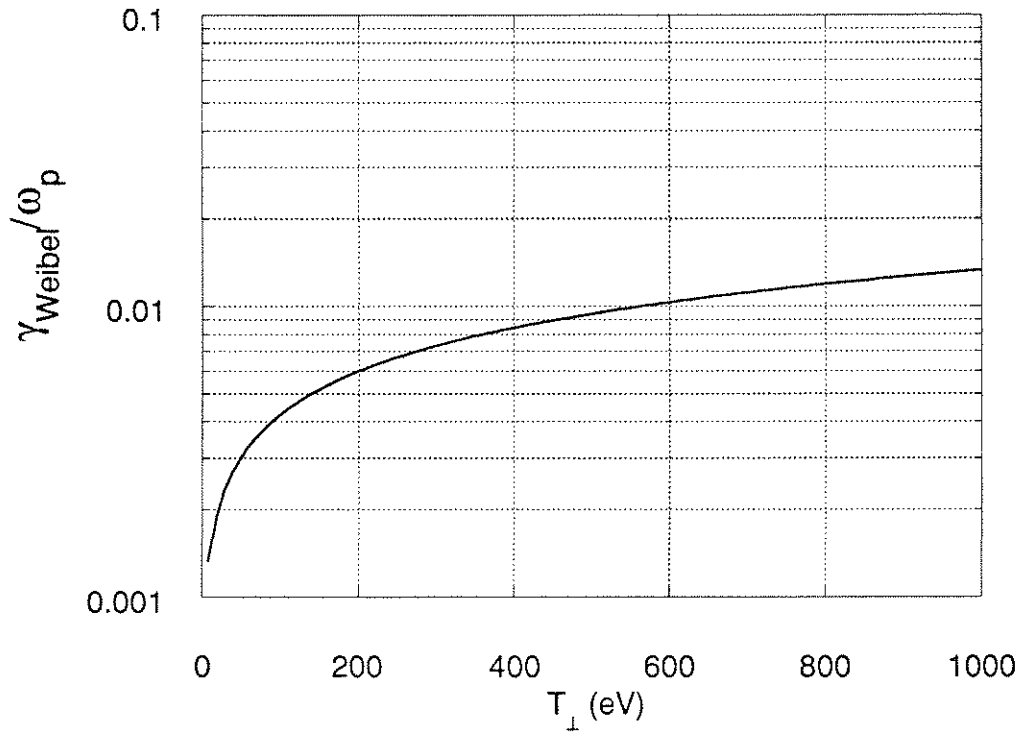
Figure 3.26: Theoretical Weibel instability growth rate as a function of $T_\perp$ for a tunneling ionization plasma.

However, temperature isotropization occurred over a slower time scale, $\tau \approx (\pi/2\omega_{ce})$, where ω_{ce} is given by Eq.(3.71). Using the theoretical growth rate for our experimental parameters we find that the Weibel instability will completely isotropize the electrons in roughly 75 ps (180 ps) for circular (linear) polarization. This is consistent with the observed broadening of the SCS spectrum [Fig.(3.6b)] discussed earlier (Section 3.3.2). Although the simulations discussed here were carried out with a circularly polarized beam, similar effects occur with a linearly polarized beam.

0

-2

$\log (B_y)$

-4

-6

0   100   200   300   400
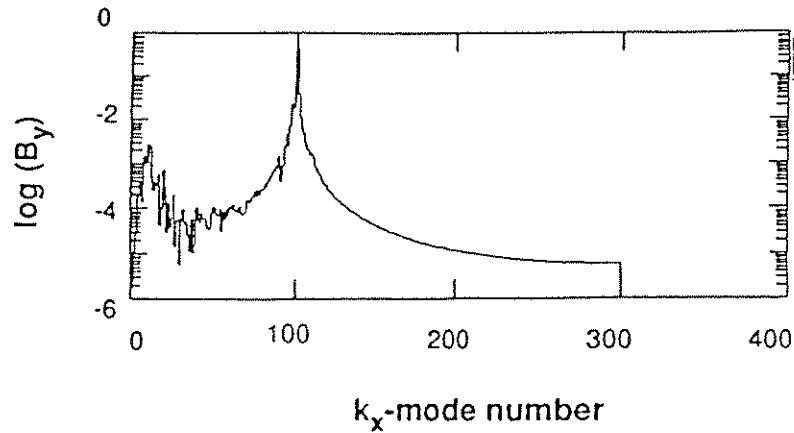
k_x-mode number

Figure 3.27: k_x - spectrum of the magnetic field in the y-direction at T=1950. The laser rise and fall time was T=500 and had a strength v_{osc}/c = 0.2. The final density was 5 x 10^{-3} n_c. The feature with mode number around 100 corresponds to the wavenumber k_0 of the laser. The feature with mode number around 20 , i.e. k_B = 0.2 k_0, is due to the Weibel instability.

3.5 Conclusion

The properties of tunnel-ionized plasmas have been studied through experiments and particle simulations. Odd harmonic emission characteristic of stepwise tunnel ionization, and density clamping due to ionization induced refraction were observed. Qualitative evidence for plasma temperature control by varying the laser polarization was obtained through measurements of the SCS instability spectra and X-ray emission. Furthermore, longitudinal temperatures were higher than those expected from a single particle model. Simulations indicated that stochastic heating and the Weibel instability play an important role in plasma heating and isotropization. The maximum obtainable

density was found to be limited by ionization induced refraction. A simple scaling law for the density clamping was derived by incorporating concepts from the paraxial ray approximation and Gaussian optics, and confirmed by simulations.

In the next chapter we present a theoretical study of the non-linear dynamics of beat excited plasma waves in a plasma with time varying conditions. As evidenced by the mode-coupled beat wave signature in the Thomson scattering data, we were able to excite such plasma waves in a tunnel ionization produced plasma. This possibility of creating plasmas with a controlled time varying density has led us to investigate the effect of both a time dependent density (and laser intensity) and the presence of short wavelength density modulations on the dynamics of beat wave generated plasma waves.

Chapter 4

Non-Linear Dynamics of Relativistic Plasma Waves

4.1 Introduction

In collinear optical mixing two laser beams with slightly different frequencies, ω_1 and ω_2, are injected into a plasma. If the difference frequency $\Delta\omega$ ($= \omega_1 - \omega_2$) is approximately equal to the plasma frequency, the ponderomotive force associated with the laser light will resonantly excite a longitudinal plasma oscillation. Energy and momentum conservation require

$$\omega_1 - \omega_2 = \omega_p \tag{4.1}$$

$$k_1 \pm k_2 = k_p \tag{4.2}$$

where the $\pm$ stands for co- or counterpropagating laser beams. The phase velocity of the plasma wave in the case of co-propagating beams equals the mean group velocity of the light waves which for an underdense plasma is almost the speed of light in vacuum. The feasibility of using these high phase velocity, large amplitude plasma waves for particle acceleration, known as the plasma beat wave accelerator (Tajima & Dawson 1979), is under investigation at UCLA (Clayton et al. 1985;1989), Rutherford Appleton

Laboratory (RAL), U.K., (Dangor et al. 1985), ILE, Japan (Kitagawa et al. 1988)and Ecole Polytechnique, France, (Amiranoff et al. 1991).

In order to achieve considerable acceleration gradients (i.e. large electric fields) inside the plasma one arranges the experiment so that the plasma density gives a plasma frequency equal to the beat frequency, i.e. $\frac{\omega_p}{\Delta\omega} \approx 1$, and large laser intensities are required. The laser intensity is so large that one can no longer neglect relativistic effects on the equation of motion for the plasma electrons, leading to the phenomenon of relativistic detuning of the plasma frequency (Rosenbluth & Liu 1972).

In practice the actually obtained plasma density can differ significantly from the resonant density and may be varying in time. Furthermore, in the process of building up the large amplitude plasma wave, competing instabilities such as stimulated Raman scattering (SRS) and stimulated Brillouin scattering (SBS) (Forslund et al. 1975, Rose et al. 1987) will scatter laser energy out of the plasma and create low phase velocity short wavelength electron plasma waves and ion waves. These waves represent in effect a spatial and temporal modulation of the plasma dielectric constant.

We will study the non-linear dynamics associated with generation of the plasma beat wave in such a spatio-temporally modulated plasma through numerical modelling. The goal is to determine the experimental conditions necessary to observe the different non-linear phenomena.

In section 4.2 we begin with a treatment of the problems associated with varying the plasma frequency in time and present the well known relativistic Lagrangean oscillator model (Tang et al. 1985, Horton & Tajima 1985) with the addition of a rippled component to the plasma density. The effective damping in the equation of motion of the fluid momentum will contain a contribution of the ionization rate which gives rise to the temporally varying plasma density.

The obtained equations are then solved numerically in section 4.3 giving the following results: the plasma wave exhibits hysteresis when, for a given damping rate, wavelength and amplitude of the plasma ripple, and laser intensity (plasma density), the plasma density (laser intensity) is varied in time. Furthermore, when the laser intensity is varied in time, regions in parameter space are found where the motion of the fluid element shows period doubling followed by chaotic motion (Feigenbaum 1978) or where an incomplete period doubling tree (Bier & Bountis 1984) is observed. However, reconstructing the waveform in the lab frame we find that wavebreaking occurs before the second bifurcation. The physical origin of the first bifurcation is analyzed by applying a perturbation technique to an equivalent generalized Mathieu's equation.

In section 4.4 results are shown from the fully relativistic, electromagnetic, particle-in-cell code WAVE (Morse & Nielson 1971) which has been used to verify the validity of the analytic model. It includes all the effects competing with the build up of a large amplitude plasma wave. We conclude with a summary of the obtained results.

4.2 Lagrangean Model of Relativistic Plasma Waves

4.2.1 Why a Lagrangean model?

The non-linear features of the plasma wave can be classified into two categories: bistability, with the associated hysteresis effect, and the existance of subharmonics with the possibility of a transition to chaos. Bistability and hysteresis have been discussed by Ma and Xu (Ma & Xu 1989) within the slowly varying envelope approximation. They studied the case where the time varying plasma frequency is very close to the resonance

frequency $\Delta\omega$, for $\alpha_1\alpha_2$ much less than one where α_i is the quiver velocity of the electron in the laser field normalized to the speed of light, v_{osc}/c. The damping in their model is dominated by collisional effects but they neglected any velocity dependence of the collision frequency. Furthermore, the assumption that the fluid element displacement is modeled by

$$\xi(\tau, w_0) = \varepsilon(\tau) \sin [\tau - w_0 + \Phi(\tau)] \tag{4.3}$$

where ε and Φ are the slowly varying amplitude and phase respectively, precludes the authors from observing subharmonics in the motion of the fluid elements.

The possibility of chaotic behavior of the plasma wave for large driver strengths has been discussed by Mendonça (Mendonça 1985). In this paper the analogy was used between the equation of motion of the longitudinal electric field, derived under the weakly relativistic approximation, and the Duffing equation (Duffing 1918). The weakly relativistic approximation is valid when α_i is much less than 1 and the amplitude of the plasma wave satisfies the condition $\frac{n_1}{n_0} \ll 1$ where n_1 is amplitude of the density modulation and n_0 is the background plasma density. The Duffing equation models the motion of a non-relativistic particle in an anharmonic potential. It has been shown (Holmes & Rand 1976, Huberman and Crutchfield 1979) that chaotic motion occurs for displacements which bring the oscillator close to the turning points of the potential.

First of all, as pointed out by Mori (Mori 1987) and McKinstrie and Forslund (McKinstrie & Forslund 1987), Mendonça erred in the sign of the frequency detuning of the plasma frequency, in the equation of motion of the longitudinal electric field. When deriving the equivalent potential from the restoring force terms in the equation of motion, this leads to the wrong shape of the anharmonic potential. Secondly, even for the correct shape of the potential we found that, analogous to Duffing oscillator, chaotic motion occurs for displacements which bring the oscillator close to the turning points of

the potential. However, when treating the relativistic terms exactly one arrives at a shape of the associated potential well which does not have any turning points. Indeed, in a Lagrangean frame it is straightforward to show that the equation of motion in the absence of damping for the momentum of relativistic plasma waves is given in it simplest form by

$$\frac{d^2p}{dt^2} + \omega_p^2 \frac{p}{\sqrt{1 + p^2}} = \frac{d}{dt} F_{NL} \tag{4.4}$$

where F_{NL} is the ponderomotive force. The restoring force can now be derived from a potential

$$V(p) = \sqrt{1 + p^2} - 1 \tag{4.5}$$

In Fig.(4.1) we show the exact potential as given by Eq.(4.5) and its Taylor expansion up to 2nd order which is equivalent to the anharmonic potential in the Duffing model. As can be seen from Fig.(4.1), the two potentials start differing significantly in shape beyond |p| = 1 and the use of the Taylor expansion for the potential is not justified for the large momentum regime for the following reasons: while the exact potential has only one stable equilibrium point and the radius of curvature of the potential never changes sign, its Taylor expansion has one stable and two unstable equilibrium points and clearly, the radius of curvature of this potential changes sign.

From non-linear dynamics it is well known that the existance of unstable equilibrium points changes the behavior of any system in a fundamental way. In particular for the Duffing oscillator it is found that a) it exhibits hysteresis and period doubling only for driver strengths that bring the oscillator close to these unstable points; b) when the amplitude exceeds momentarily the turning point limit, the oscillator is unstable and undergoes a jump to the lower amplitude branch or continues to roll down the potential towards infinity. From this we conclude that the rich non-linear behavior

(i.e. period doubling route to chaos and bistability) exhibited by the model-equation of the longitudinal electric field as obtained under the weakly relativistic approximation, is an artefact of this approximation. The details of the analysis are given in Appendix D.

However, it is well understood that the Duffing oscillator undergoes period doubling and shows hysteresis when the particle moves in an asymetric potential well. In practice such a situation can arise without the excursion of the fluid element becoming unreasonably large when the wave is excited in a plasma whose density is rippled. The background plasma can be rippled, for example, due to the presence of a slow phase velocity electron plasma wave due to stimulated Raman scattering or an ion wave due to stimulated Brillouin scattering.
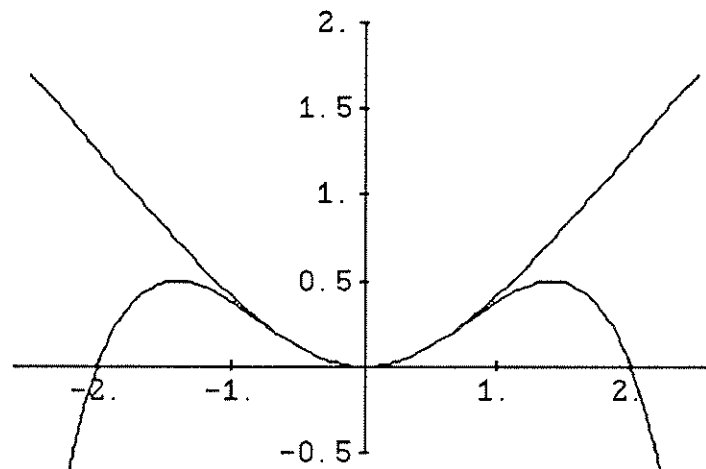

Figure 4.1: Plot of potential $V(p) = \sqrt{1+p^2} - 1$ and its Taylor expansion $\frac{p^2}{2} - \frac{p^4}{8}$

4.2.2 Fluid Equations for Ionizing Plasma

Since in the beat excitation of relativistic plasma waves the amplitude of the longitudinal electric field is critically dependent on the ratio $\frac{\omega_p}{\Delta\omega}$ it is necessary to study

the effect of detuning ($\Delta\omega \neq \omega_p$) caused by a time dependent plasma density. The main phenomenon leading to a time dependence of the bulk plasma density in the focal volume of the laser beam on a time scale relevant for the beat excitation is avalanche ionization (increase in plasma density) initiated, for example, by laser-induced (multiphoton) ionization (MPI) (Shen 1984, Dangor et al. 1987, Leemans et al. 1991c). Ponderomotive and/or thermal self-focussing (Max 1976, Kaw et al. 1973, Estabrook et al. 1985, Tripathi & Pitale 1977, Cohen & Max 1979) which decreases the plasma density, occurs on a time scale set by the ions and will not be included in our analytic model.

Two possible ways of dealing with this ionizing plasma are as follows: the first way is to treat each newly added amount of electrons and ions as a new species in the plasma. It starts out at rest and will move under the influence of the electromagnetic fields present inside the plasma. Thus it is necessary to solve a system of N-coupled second order non-linear differential equations, where N is the number of groups of plasma "species" one wishes to follow, which implies that a rigorous analytic treatment of this problem can not be done. The second way involves making the following approximation: we model the plasma using a one particle distribution function (Krall & Trivelpiece 1973). The momentum associated with an infinitely small fluid element is obtained by adding up the momentum vectors of each individual particle. So, when new particles which are initially at rest are added to a particular fluid element, its total density increases while its momentum is reduced.

The functional form describing the rate at which new plasma is being produced depends on the involved ionization proces. Consider therefore a beat wave excitation experiment using a CO_2 laser. As shown in Chapter 3 it is reasonable to assume that tunneling ionization is the dominant process in the plasma formation. Since the newly born electrons start out at rest the source of plasma can be modeled as:

$$S(r,p,t) = \lambda \, n(r,t) \, \delta(p) \qquad\qquad (4.6)$$

where λ is an effective ionization rate, r and p are respectively the position and momentum of the fluid element, t is the time and $n(r,t)$ is the plasma density. Taking moments of the Vlasov equation with this source term gives us the fluid equations. The details of this calculation can be found in Appendix C. The resulting equation of continuity is given by

$$\frac{\partial n(r,t)}{\partial t} + \frac{\partial}{\partial r} \cdot [\, n(r,t) \frac{P}{m_0 \gamma}\,] = \lambda \, n(r,t) \qquad\qquad (4.7)$$

while the equation of motion of the fluid element is found to be

$$\frac{\partial}{\partial t} [\, P(r,t)\,] + v \cdot \frac{\partial P(r,t)}{\partial r} - q \,[\, E + \frac{p \times B}{\gamma \, m_0 c}\,] + \lambda \, P(r,t) = 0 \qquad\qquad (4.8)$$

It is noticed that the global effects of injecting new plasma into an oscillating plasma are as follows: (a) the time-varying plasma density results in a time varying plasma frequency and (b) the ionization rate shows up as an effective damping for the single-fluid momentum. Using the analogy of a mass - spring system these effects can be easily understood: since the newly added mass is initially at rest, it slows down the oscillating mass and at the same time it changes the spring constant, i.e. the oscillation frequency. The obtained fluid Eqs. (4.7) and (4.8) complemented by Maxwell's equations are used to derive the equation of motion of the longitudinal fluid element displacement, driven by the ponderomotive force due to the beating of two transverse linearly polarized electromagnetic waves, in a plasma with a rippled density.

4.2.3 Equation of Motion

The equation of motion for a Lagrangean oscillator moving in a one-dimensional cold plasma in the electrostatic limit is given by (Dawson 1959, Richardson & Schram 1968)

$$\frac{\partial p_e}{\partial \tau} = -e\, E + F_{NL} - \lambda\, p_e \tag{4.9}$$

where we assumed that ions are immobile. F_{NL} is the ponderomotive force given by

$$F_{NL} = \frac{m_0}{\gamma}\, c\, \Delta \omega\, \frac{\alpha_1 \alpha_2}{2} \sin(\Delta k\, x - \Delta \omega\, \tau) \tag{4.10}$$

with γ the Lorentz factor, m_0 the electron rest mass, c the speed of light and $\alpha_{1,2}$ the quiver velocity of the electrons in the laser fields normalized to the speed of light.

So long as the Lagrangean fluid elements do not cross, the one-dimensional Gauss law can be integrated immediately to give the electric field, i. e.

$$E = 4\pi e \int_0^\xi N_i(x = x_0 + \xi')\, d\xi' \tag{4.11}$$

In the usual case N_i is uniform ($= N_e$), so one has $E = 4\pi N_e\, \xi$, whose simplicity accounts for the popularity of the model. Koch and Albritton (Koch & Albritton 1974) used the model in a ramp plasma ($N_c(x) = N_0(1 + x/L) = N_0(1 + x_0/l + x/L)$), to investigate wave breaking in plasma waves driven by so-called optical resonance. Here we are interested in a rippled plasma (Darrow et al. 1987)

$$n_i = N_0(1 + \varepsilon \sin k_i\, x) \tag{4.12}$$

or, substituting for $x = x_0 + \xi$

$$n_i = N_0 [1 + \varepsilon \sin k_i (x_0 + \xi)] \tag{4.13}$$

where ε is the ripple size. This type of density ripple is particularly interesting since such a ripple is easily excited under beat wave experimental conditions due to the cogeneration of low-frequency ($\omega_{ac} \ll \omega_p$) SBS-driven ion acoustic waves.

From Eq.(4.11) we then obtain for the electric field

$$E = 4 \pi e N_0 \int_0^\xi (1 + \varepsilon \sin k_i(x_0 + \xi')) \, d\xi' \tag{4.14}$$

or

$$E = 4 \pi e N_0 [\xi + \frac{\varepsilon}{k_i} (\cos k_i x_0 - \cos k_i (x_0 + \xi)) \tag{4.15}$$

Using

$$\frac{\partial p_e}{\partial \tau} = m_0 \gamma^3 \overset{\circ}{v}_e \tag{4.16}$$

and

$$\frac{\partial \xi}{\partial \tau} = v_e \tag{4.17}$$

Equation (4.9) becomes

$$\frac{\partial^2 \xi}{\partial \tau^2} + \frac{\lambda}{\gamma^2} \frac{\partial \xi}{\partial \tau} + \frac{\omega_p^2}{\gamma^3} [\xi + \frac{\varepsilon}{k_i} \cos(k_i x_0 - \cos k_i(x_0 + \xi))] =$$

$$\Delta\omega \frac{c}{\gamma^4} \frac{\alpha_1 \alpha_2}{2} \sin(\Delta k (x_0 + \xi) - \Delta\omega \tau) \tag{4.18}$$

where

$$\gamma = [1 - (\frac{\dot{\xi}^2 + v_\perp^2}{c^2})]^{-1/2} \tag{4.19}$$

with $(\frac{v_\perp}{c})^2 = \alpha_1 \alpha_2$, which depends on the laser intensities.

From the dispersion relation for electromagnetic waves in a plasma we also have

$$c \, \Delta k = c(k_1 - k_2) = \Delta\omega \, (1 + \frac{\omega_p^2}{2\omega_1\omega_2}) \tag{4.20}$$

and since typically $\omega_1, \omega_2 \gg \omega_p$ this reduces to $c \, \Delta k \approx \Delta\omega$.

We now have to distinguish between sweeping the plasma frequency through ionization and/or plasma blowout, and sweeping the driver frequency through, for example, chirping the laser beam. For the former we normalize time with respect to $\Delta\omega^{-1}$, space with respect to Δk^{-1} and obtain

$$\frac{\partial^2 u}{\partial \tau^2} + \frac{\lambda}{\gamma^2}\frac{\partial u}{\partial \tau} + \frac{\omega_p^2}{\gamma^3}\{u + \varepsilon\frac{\Delta k}{k_i}[\cos w_0 - \cos(w_0 + \frac{k_i}{\Delta k} u)]\} =$$

$$\frac{\Delta\omega^2}{\gamma^4}\frac{\alpha_1\alpha_2}{2}\sin[(w_0 + u) - \tau] \tag{4.21}$$

with $u = \Delta k \, \xi$, $w_0 = k_i x_0$, $\tau = \Delta\omega \, t$ and $\gamma = [1 - (\frac{\dot{u}}{\Delta\omega})^2 - \alpha_1\alpha_2]^{-1/2}$.

For the latter we normalize time with respect to ω_p^{-1}, space with respect to c/ω_p and obtain

$$\frac{\partial^2 \zeta}{\partial \eta^2} + \frac{\Gamma}{\gamma^2}\frac{\partial \zeta}{\partial \eta} + \frac{1}{\gamma^3}\{\zeta + \frac{\varepsilon}{\kappa}[\cos \kappa w_0 - \cos \kappa(w_0 + \zeta)]\} =$$

$$\frac{\Delta\omega}{\omega_p}\frac{1}{\gamma^4}\frac{\alpha_1\alpha_2}{2}\sin[\frac{\Delta\omega}{\omega_p}(w_0 + \zeta) - \frac{\Delta\omega}{\omega_p}\eta] \tag{4.22}$$

with $\zeta = \xi / \frac{c}{\omega_p}$, $w_0 = x_0 / \frac{c}{\omega_p}$, $\eta = \omega_p \tau$, $\Gamma = \frac{\lambda}{\omega_p}$, $\kappa = \frac{ck_i}{\omega_p}$

and $\gamma = [1 - (\dot{\zeta})^2 - \alpha_1\alpha_2]^{-1/2}$.

The obtained equation of motion given by Eqs. (4.21) and (4.22) have been solved numerically and the results are presented in the next section. Since the obtained results for sweeping ω_p or sweeping $\Delta\omega$ are very similar we will only discuss the case of the time varying plasma frequency in this chapter.

4.3 Numerical Results

In order to capture the full non-linear richness of the behavior of the plasma waves it is necessary to resort to a numerical integration of the relativistic equation of motion for the Lagrangean fluid element as given by Eqs. (4.21) and (4.22). Due to the high dimensionality of this parameter space we have limited ourselves to a subspace of experimentally accessible values. In principal the damping rate has contributions due to collisions, Landau damping (Chen 1984), ionization of the plasma, and mode coupling (Darrow et al. 1986) to slow phase velocity plasma waves. As pointed out by Matte and Martin (Matte & Martin 1988) collisional damping is negligible for the case of relatively large driver strengths (v_{osc}/c larger than 0.1) and plasma wave amplitudes. Landau damping is only important when the ratio of phase velocity of the waves to thermal velocity of the plasma electrons, $\frac{v_\phi}{v_{th}}$, is less than 4. Therefore as a direct damping mechanism for the high phase velocity waves it can be neglected. However, mode coupling establishes very efficient transfer (Kruer 1972, Kruer & Dawson 1970) between fast and slow electron plasma waves which can couple their energy to the plasma through Landau damping. Typically it is found that its contribution to the damping rate is on the order of a few percent. The contribution of the ionization process to the damping depends on the ionization rate which in this paper is assumed to be on

the order of 0.01 ω_p. Therefore the total damping rate is varied within the range 0.01 ω_p - 0.1 ω_p.

The range of wave number ratios is determined as follows: one mechanism for generating the density modulation is the generation of ion waves through stimulated Brillouin scattering. This produces ion waves with wave number $k_i = 2 k_0$, where k_0 is the wave number of the laser frequency. If we take the experimental conditions of the UCLA experiment (Clayton et al. 1985;1989), the ratio $k_i/\Delta k$ is typically on the order of 30. However this ratio can be as low as 2 if one considers the ion wave to be generated through the ion-acoustic decay instability.

We will consider for most cases that the driver strength is limited to $v_{osc}/c = 1$, while the detuning ratio $\omega_p/\Delta\omega$ is varied in the range 0.5 through 2. We have chosen to vary these two parameters as a function of time keeping the others constant.

4.3.1 Plasma Frequency or Laser Frequency Varying with Time.

For the case of an unrippled plasma density we have observed hysteresis loops in plotting the fluid element displacement vs. detuning ratio when $\dfrac{\omega_p}{\Delta\omega} \approx 1$. and $\dfrac{\omega_p}{\Delta\omega} \approx$ 0.5 for a range of driver strengths and damping coefficients. An example is shown in Fig.(4.2) for $\dfrac{v_{osc}}{c} = 0.2$ $\Gamma = 0.01$. The first, around $\dfrac{\omega_p}{\Delta\omega} \approx 1$., is the usual beat wave excitation which has at exact resonance a secular growth while the second, around $\dfrac{\omega_p}{\Delta\omega} \approx$ 0.5 , is a parametric amplifier (Rosenbluth & Liu 1972) with an exponential growth rate.

In the absence of the ion ripple period doubling was only observed for $\frac{\omega_p}{\Delta\omega} \approx 0.5$ and when the driver strength was extremely large so that $\frac{v_{osc}}{c}$ is on the order of a few times 1. At those driver strengths the Lagrangean fluid element makes excursions on the order of the plasma wave length and hence approaches the unstable points associated with the sinusoidaly varying ponderomotive potential. Of course one can no longer neglect either the coupling between transverse and longitudinal momentum for those ponderomotive forces or the, even more important, wave breaking effect which will be discussed in section 4.3.3.

In the presence of an ion ripple, however, we have observed period doubling for $\frac{v_{osc}}{c}$ varying between 0.1 and 1. Depending on the ripple size ε an incomplete Feigenbaum tree is observed ($0.12 < \varepsilon < 0.50$) or a complete period doubling cascade followed by windows of alternating chaotic and regular motion ($\varepsilon \approx 0.75$). Although the experimental realization of such large ripples is doubtful, the fact that this system can
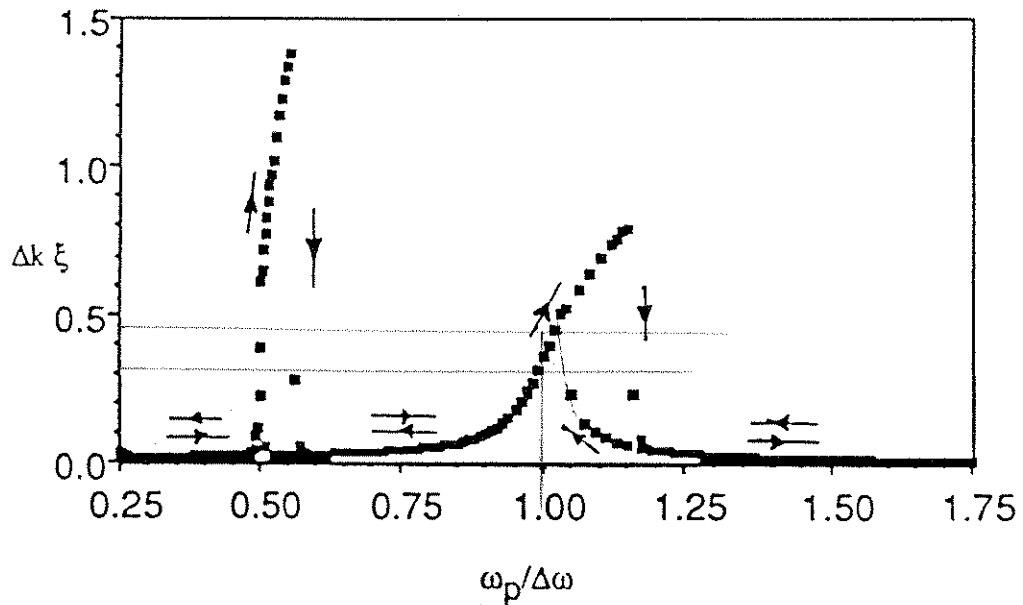

Figure 4.2: Detuning curve for a relativistic Lagrangean fluid element for $\frac{v_{osc}}{c} = 0.2$ and $\Gamma = 0.01$ in the absence of a density ripple. The arrows show the existence of hysteresis loops

show this rich behavior for certain parameters allows one to classify the obtained equations among the general class of equations exhibiting the Feigenbaum characteristics and hence apply the same universality principles ruling all such systems. This will be discussed more in detail in the next section.

4.3.2 Laser Intensity Varying in Time

To demonstrate the effect of a time varying driver strength on the motion of the Lagrangean oscillator, we show in Fig.(4.3) the amplitude of the fluid element excursion as a function of time for a laser intensity which has a Gaussian time dependence, i.e

$$I_l = I_0 \, e^{-(\frac{t-t_0}{\Delta t})^2} \qquad (4.23)$$

where I_0 is the peak laser intensity, t_0 is the time at which the laser intensity peaks and Δt is the paser pulse width. The oscillator is again moving in a rippled background and has a resonant frequency which differs considerably from the driver frequency. The numerical values used in this calculation are: damping rate $\Gamma = 0.03$, wave number ratio $k_i/\Delta k = 30.$, ripple size $\varepsilon = 0.75$ and detuning ratio $\omega_p/\Delta\omega = 1.9$

For very early times, not shown in the figures, the system behaves linearly: the homogeneous solution, oscillating at the natural frequency, is soon dominated by the driven solution. The amplitude grows approximately linearly. As shown in Fig.(4.3), as time goes on, the system develops higher harmonics indicating that it has entered the non-linear regime. The phase space plot shows an outward spiralling curve, because the driver strength is continuously increasing, and is egg shaped due to the harmonic content of the motion.

Figure 4.3a,b,c: Time series, phase space plot and spectrum of the displacement of a relativistic Lagrangean fluid element, moving in a rippled plasma. The driver strength has a Gaussian time dependence with $(\frac{v_{osc}}{c})_{peak} = 0.55$. The damping rate equals $\Gamma = 0.03\ \Delta\omega$, ripple size $\varepsilon = 0.75$, wave number ratio $\frac{k_i}{\Delta k} = 30$, and detuning ratio $\frac{\omega_p}{\Delta\omega} = 1.9$. The laser pulse has a full width at half maximum of $500\ \omega_p^{-1}$ and reaches its peak at $T = 1200\ \omega_p^{-1}$ in simulation units. In figure (a) - (f) the fluid element develops subharmonics up to eighth subharmonic and becomes chaotic; in figure (g) - (i) it goes from chaotic into periodic showing fifth followed by tenth subharmonic.
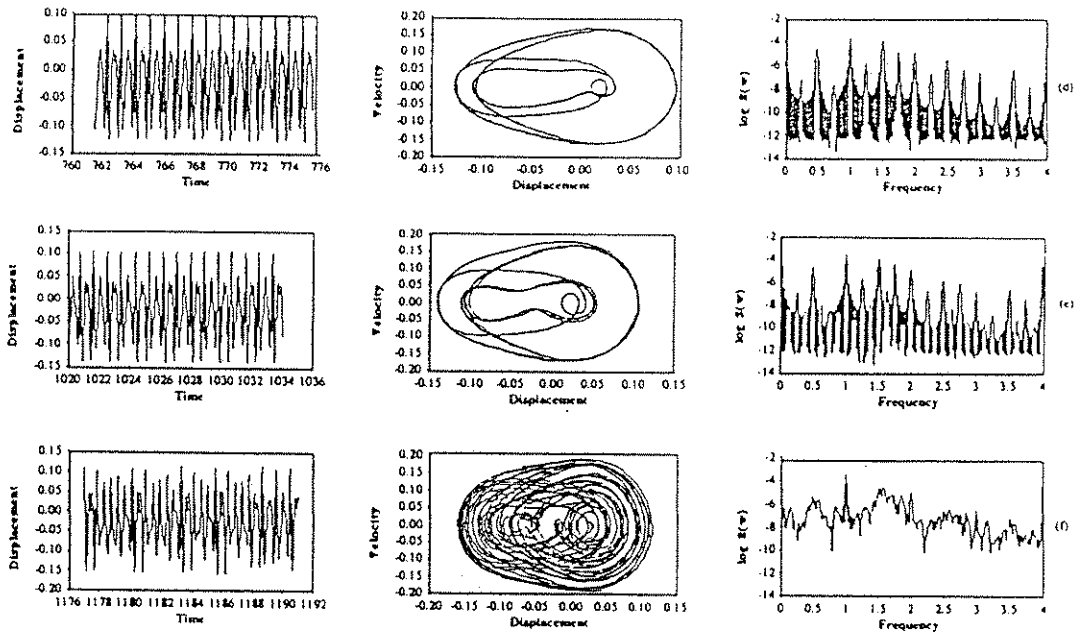
Figure 4.3d,e,f: Time series, phase space plot and spectrum of the displacement of a relativistic Lagrangean fluid element, moving in a rippled plasma for the same parameters as in Fig.4.3a,b,c.
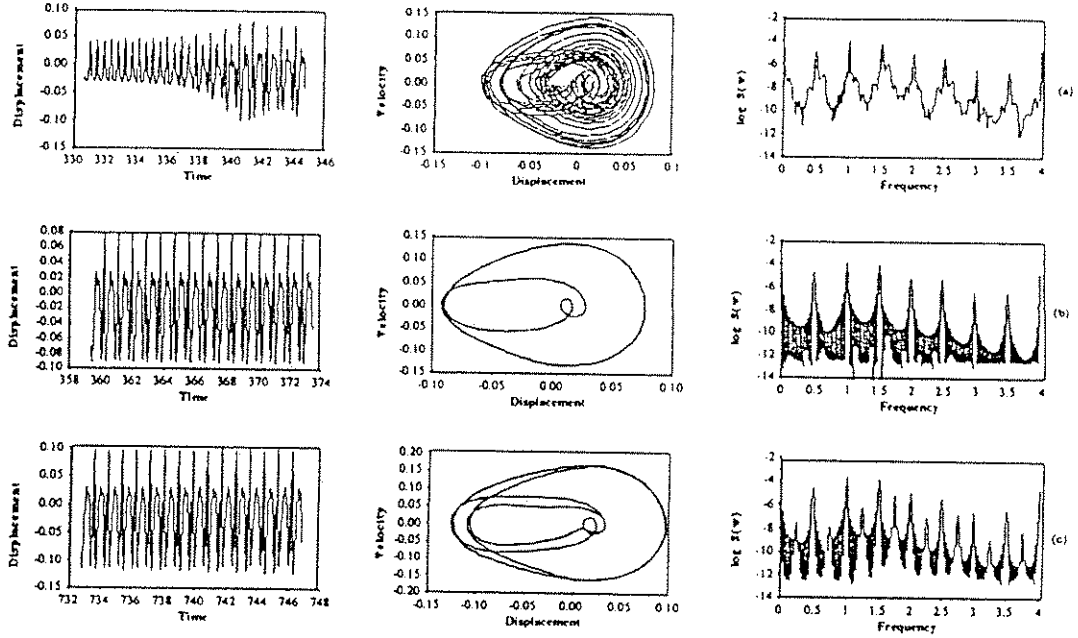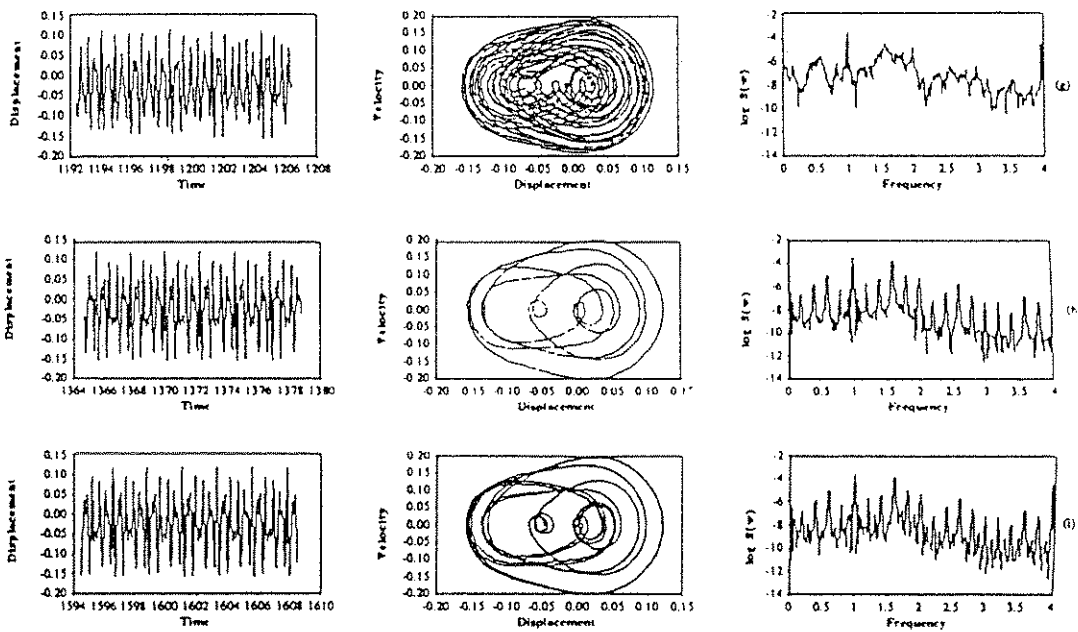
Figure 4.3g,h,i: Time series, phase space plot and spectrum of the displacement of a relativistic Lagrangean fluid element, moving in a rippled plasma for the same parameters as in Fig.4.3a,b,c.

Then, suddenly, at approximately $t = 340 \, \omega_p^{-1}$, the motion undergoes a first bifurcation: the frequency spectrum shows half harmonics while in phase space the limit cycle has split into two loops [Fig.(4.3a)]. As the intensity increases further one notices a few more bifurcations (up to the 1/16 th subharmonic) [Fig.(4.3b)-(4.3e)] followed by the onset of chaotic motion [Fig.(4.3f)-(4.3g)]. As the intensity reduces the system returns to a periodic motion with period five [Fig.(4.3h)], undergoes a bifurcation to produce period 10 subharmonic [Fig.(4.3i)], becomes chaotic again for a narrow range of driver strengths and undergoes eventually an inverse period doubling cascade to return to a regular periodic motion with decreasing amplitude.

To ascertain that the observed behavior can be classified as a period doubling route to chaos, we have constructed a Poincaré map (Moon 1987) by stroboscopically sampling the motion of the oscillator at a rate equal to the driver frequency. In Fig.(4.4) we show a bifurcation tree of the amplitude of the fluid element displacement as a function of the driver strength, for the same parameter values as in Fig.(4.3).
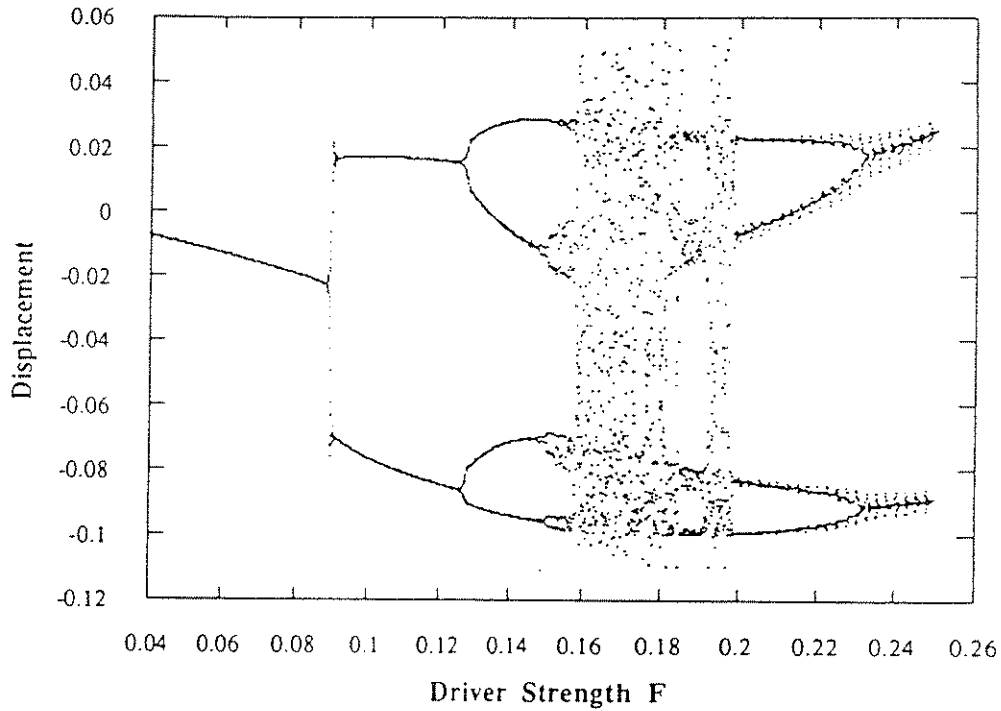
Figure 4.4: Bifurcation tree for the relativistic Lagrangean fluid element. The driver strength increases linearly with $(\frac{V_{osc}}{c})_{peak} = 0.7$. The damping rate equals $\Gamma = 0.03 \, \Delta\omega$, ripple size $\varepsilon = 0.75$, wave number ratio $\frac{k_i}{\Delta k} = 30$, and detuning ratio $\frac{\omega_p}{\Delta\omega} = 1.9$.

The first bifurcation is discontinuous followed by a series of continuous pitchfork bifurcations. The phase-plane Poincaré map for a driver strength value in the chaotic regime is shown in Fig.(4.5). Despite a low damping rate the map shows fractal-like structure of a strange attractor (Moon 1987).

In order to assess whether the Lagrangean fluid element undergoes the classical period doubling route to chaos, we compared the values of the following three important quantities with their theoretical values as obtained by Feigenbaum: a) the ratio δ_i of the control parameter values of F,

$$\delta_i = \frac{F_{i-1} - F_i}{F_i - F_{i+1}} \tag{4.24}$$
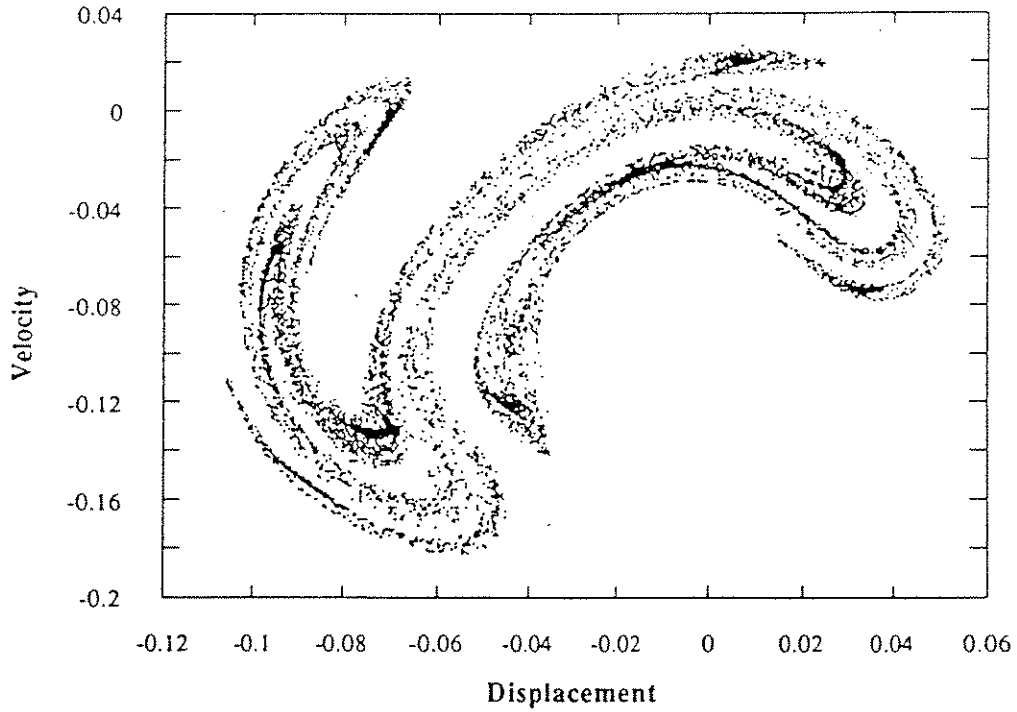
Figure 4.5: Poincaré Map associated with chaotic motion of the Lagrangean fluid element. The damping rate equals to $\Gamma = 0.03 \, \Delta\omega$, ripple size $\varepsilon = 0.75$, wave number ratio $\frac{k_i}{\Delta k} = 30$, and detuning ratio $\frac{\omega_p}{\Delta\omega} = 1.9$. The driver strength was fixed at $\frac{v_{osc}}{c} = 0.6$.

at which the bifurcations occur, b) the pitchfork rescaling parameter α, and c) the rate μ at which successive subharmonics in the power spectrum fall off. The theoretical values of those three parameters are: $\delta_\infty = 4.66920...$, $\alpha = 2.503...$ and $\mu = 4.58...$. Taking in consideration that the damping rate of the fluid element is low, we have found δ to converge fairly well to the limit ratio: $\delta_1 = 1.7$, $\delta_2 = 3.8$, $\delta_3 = 4.7$. The rescaling parameter $\alpha = 2.6$, as obtained from the second bifurcation in Fig.(4.5), is very close to the theoretical value, but the lower branch does not follow the same rescaling law. From the power spectrum it is seen that the subharmonics drop by a value μ close to the theoretical value only when one takes an average over a frequency range extending to $\omega = 4\,\Delta\omega$. We therefore conclude that a deeper investigation is needed into the mathematical origins of the bifurcations to ascertain that the classical period doubling route is followed by this system on its way to chaos.

For smaller ripple sizes ($\varepsilon < 0.5$) we have observed incomplete period-doubling cascades. Fig.(4.6) shows an incomplete bifurcation tree and the existence of hysteresis for a case where the ripple size $\varepsilon = 0.15$, wave number ratio $k_i/\Delta k = 30.$, and detuning parameter $\omega_p/\Delta\omega = 1.7$. In Fig.(4.7) a parameter space plot is shown for the driver strength as a function of plasma frequency detuning ratio. We have limited the driver strength to a value corresponding to $\frac{v_{osc}}{c} = 1.$ and varied the detuning ratio $\frac{\omega_p}{\Delta\omega}$ from 0.3 to 2.2. As the third parameter we have used the ripple amplitude. We notice two distinctly different regions for the detuning ratio: one cluster of data points is situated around $\frac{\omega_p}{\Delta\omega} \approx 1.8$ and one is situated around $\frac{\omega_p}{\Delta\omega} = 0.5$.

from observing this phenomenon in a laboratory experiment. Since the displacement of the fluid element will contain spatial frequencies at Δk_j, wavebreaking will occur when $\Delta k_j \xi > 1$. To verify whether the period doubling route can be completely modelled with the Lagrangean oscillator model we followed the motion of many oscillators (up to 1000 per ion wave length) starting out with different equilibrium positions. It was found that wavebreaking occurs before the second bifurcation takes place. This clearly limits the validity of our model for describing the period doubling route in this beatwave system. To assess whether even this first bifurcation could survive in a "real" plasma we resorted to particle-in-cell simulations, which are the subject of section 4.4. The origin of this first bifurcation is analyzed in the next section.

4.3.4 Origin of the First Bifurcation

The analysis is based on a theoretical study by Szemplinska-Stupnicka and Bajkowski (Szemplinska-Stupnicka & Bajkowski 1986) on the 1/2 subharmonic resonance and its transition to chaotic motion in a non-linear oscillator. The analysis proceeds as follows: first we reduce the driven relativistic Lagrangean oscillator equation to an equivalent driven Mathieu/Duffing equation. After solving for a steady state solution, oscillating at the driver frequency, the stability against half-harmonic perturbations is analyzed. For the case of zero ripple amplitude an analytical solution is found for the region in parameter space ($\frac{\Delta \omega}{\omega_p}$, F) which the steady state solution is unstable against perturbations at half the driver frequency. The boundary of this region is in excellent agreement with the Arnold-like tongue, obtained by solving the exact Lagrangean equation using a Runge-Kutta routine.

4.3.4.1 Steady State Solution of the Lagrangean Oscillator

We start from the driven relativistic Lagrangean oscillator equation [Eq.(4.21)] which models the behavior of a Langrangean fluid element moving in a plasma with a density ripple under the influence of the ponderomotive force:

$$\ddot{u} + \frac{\alpha}{\gamma^2}\dot{u} + \frac{\beta^2}{\gamma^3}[u + \delta \sin Ku] = -\frac{F}{\gamma^4}\cos(u - \tau) \tag{4.25}$$

We now assume that the longitudinal velocity $\dot{u}$ is small compared to the quiver velocity v_{osc} so that the Lorentz factor γ can be approximated as

$$\gamma \approx \left[1 - \left(\frac{v_{osc}}{c}\right)^2\right]^{-1/2} = \Gamma \tag{4.26}$$

Expanding the cosine function in Eq.(4.25) and using Eq.(4.26) we then obtain

$$\ddot{u} + \alpha_1(t)\dot{u} + \left(\alpha_2(t) + \alpha_3(t)\sin \tau\right)u + \alpha_4(t)\delta.\sin Ku = -\alpha_3(t)\cos \tau \tag{4.27}$$

where

$$\begin{cases} \alpha_1(t) = \dfrac{\alpha}{\Gamma^2} \\[2mm] \alpha_2(t) = \dfrac{\beta^2}{\Gamma^3} \\[2mm] \alpha_3(t) = \dfrac{F}{\Gamma^4} \end{cases} \tag{4.28}$$

We now write $v = K u$ so that Eq.(4.28) becomes

$$\ddot{v} + \alpha_1\dot{v} + \left(\alpha_2 + \alpha_3 \sin \tau\right)v + \alpha_2 K\delta \sin v = -K\alpha_3 \cos \tau \tag{4.29}$$

and will look for a steady state solution of Eq.(4.29) of the form

$$v = v_0(t) = C_0 + C_1 \cos(\tau + \theta) \tag{4.30}$$

Substituting Eq.(4.30) into Eq.(4.29), using the identities

$$\cos(a \cos \tau) = 2 \sum_{n=0}^{\infty} (-1)^n J_{2n}(a) \cos[2n\tau] - J_0(a) \tag{4.31}$$

$$\sin(a \cos \tau) = 2 \sum_{n=0}^{\infty} (-1)^n J_{2n+1}(a) \cos[(2n+1)\tau] \tag{4.32}$$

and grouping terms oscillating at the same frequency and phase we find

$$\text{D.C.-term:} \quad \alpha_2 C_0 - \frac{1}{2}\alpha_3 C_1 \sin\theta + \alpha_2 \delta \sin C_0 . J_0(C_1) = 0 \tag{4.33}$$

$$\cos(\tau+\theta)\text{-term:} \quad -C_1 + \alpha_2 C_1 - \alpha_3 C_0 \sin\theta + 2\alpha_2 \delta \cos C_0 J_1(C_1) = -K\alpha_3 \cos\theta \tag{4.34}$$

$$\sin(\tau+\theta)\text{-term:} \quad -\alpha_1 C_1 + \alpha_3 C_0 \cos\theta = -K\alpha_3 \sin\theta \tag{4.35}$$

From Eqs.(4.33)-(4.35) one can then find C_0, C_1 and θ to calculate the steady state solution v_0. We now perturb v_0, i.e. $v = v_0 + \delta v$, and substitute this into Eq.(4.29):

$$\delta \ddot{v} + \ddot{v}_0 + \alpha_1(\dot{v}_0 + \delta \dot{v}) + (\alpha_2 + \alpha_3 \sin\tau)(v_0 + \delta v) +$$
$$\alpha_2 \delta \sin(v_0 + \delta v) = -K\alpha_3 \cos\tau \tag{4.36}$$

Assuming that the amplitude of the perturbation δv is small such that $\cos \delta v \approx 1$ and $\sin \delta v \approx \delta v$, and realizing that v_0 is a solution of Eq.(4.29) we find

$$\delta \ddot{v} + \alpha_1 \delta \dot{v} + (\alpha_2 + \alpha_3 \sin\tau + \alpha_2 \delta . \cos v_0)\delta v = 0 \tag{4.37}$$

But $v_0 = C_0 + C_1 \cos(\nu\ t + \theta)$ and hence Eq.(13) becomes

$$\delta \ddot{v} + \alpha_1 \delta \dot{v} + (\alpha_2 + \alpha_3 \sin\tau + \alpha_2 \delta \cos[C_0 + C_1 \cos(\tau + \theta)])\delta v = 0 \tag{4.38}$$

100

Using the identities from Eqs.(4.31) and (4.38) we can write the cosine-function as

$$\cos\left[C_o + C_1 \cos(\tau + \theta)\right] = \cos C_o . \cos\left[C_1 \cos(\tau + \theta)\right] - \sin C_o \sin\left[C_1 \cos(\tau + \theta)\right]$$

$$= \cos C_o \left\{ 2\sum_{n=o}^{\infty}(-1)^n J_{2n}(C_1)\cos[2n(\tau + \theta)] - J_o(a) \right\} -$$

$$\sin C_o \left\{ 2\sum_{n=o}^{\infty}(-1)^n J_{2n-1}(C_1)\cos[(2n+1)(\tau + \theta)] \right\} (4.39)$$

and substituting Eq.(4.39) into Eq.(4.38) results in

$$\delta\ddot{v} + \alpha_1\delta\dot{v} + \left\{ \alpha_2\left[1 + \delta J_o(C_1)\right] + \alpha_3 \sin\tau - \right.$$

$$2\alpha_2\delta \ \sin C_o \sum_{n=o}^{\infty}(-1)^n J_{2n+1}(C_1).\cos[(2n+1)(\tau + \theta)] +$$

$$\left. \alpha_2\delta \cos C_o\left[2\sum_{n=1}^{\infty}(-1)^n J_{2n}(C_1)\cos[2n(\tau + \theta)]\right]\right\}\delta v = 0 \qquad (4.40)$$

Rewriting $\sin\tau$ as $\sin\tau = \sin(\tau + \theta)\cos\theta - \cos(\tau + \theta)\sin\theta$ and grouping terms, Eq.(4.40) becomes

$$\delta\ddot{v} + \alpha_1\delta\dot{v} + \left\{ \delta_1 + \alpha_3 \cos\theta\sin(\tau + \theta) - \left(\alpha_3 \sin\theta + 2\alpha_2\delta \ \sin C_o . J_1(C_1)\right)\cos(\tau + \theta)\right.$$

$$\left. +2\delta \ \alpha_2 \sum_{n=2}^{\infty}a_n(-1)^n \cos[n(\tau + \theta)]\right\}\delta v = 0 \qquad (4.41)$$

where $\delta_1 = \alpha_2\left[1 + \delta \ J_0(C_1)\right]$ and a_n is equal to $-\sin C_0$ ($\cos C_0$) for n odd (even). Eq.(4.41) is now in the form of Mathieu's equation which has been studied extensively. To study the stability of the Lagrangean oscillator equation [Eq.(4.25)] we now concentrate on the behaviour of the perturbation δv with time. According to the results

of studies by Hayashi (Hayashi 1964) and Szemplinska-Stupnicka and Bajkowski of the Mathieu equation, the lowest order unstable region occurs at a frequency close to

$$\sqrt{\delta_1} \cong \frac{1}{2} \tag{4.42}$$

and we therefore assume as approximate solution for the perturbation

$$\delta v(\tau) = e^{\varepsilon \tau} b_{1/2} \cos\left(\frac{1}{2}\tau + \phi\right) \tag{4.43}$$

where $\varepsilon > 0$ for an unstable region and ϕ is the phase with respect to the driver frequency. At the stability limit $\varepsilon = 0$ and hence

$$\delta v(\tau) = b_{1/2} \cos\left(\frac{1}{2}\tau + \phi\right) \tag{4.44}$$

Substituting Eq.(4.44) into Eq.(4.41) and grouping terms in cosine and sine we find the set of equations

$$\begin{cases} G\cos\theta\cos 2\phi + \left(\dfrac{\alpha_3}{2} + G\sin\theta\right)\sin 2\phi = \left(\delta_1 - \dfrac{1}{4}\right) \\ \left(\dfrac{\alpha_3}{2} - G\sin\theta\right)\cos 2\phi + G\cos\theta\sin 2\phi = -\dfrac{\alpha_1}{2} \end{cases} \tag{4.45}$$

where

$$G = \alpha_2 \delta \sin C_0 . J_o(C_1) \tag{4.46}$$

and C_0, C_1 and θ are the steady state solutions of Eq.(4.29). Solving Eq.(4.46) and using the fact that $\sin 2\phi$ and $\cos 2\phi$ are not independent we arrive at

$$\frac{\left(g_1 g_5 + g_3 g_4\right)^2 + \left(g_1 g_3 + g_2 g_4\right)^2}{\left(g_3^2 - g_2 g_5\right)^2} = 1 \tag{4.47}$$

where

102

$$
\begin{cases}
g_1 = \delta_1 - \dfrac{1}{4} \\[2ex]
g_2 = \dfrac{\alpha_3}{2} + G\sin\theta \\[2ex]
g_3 = G\cos\theta \\[2ex]
g_4 = \dfrac{\alpha_1}{2} \\[2ex]
g_5 = \dfrac{\alpha_3}{2} - G\sin\theta
\end{cases}
\tag{4.48}
$$

The boundaries of the unstable regions can then be determined by solving the coupled non-linear equations Eqs.(4.33)-(4.35) and (4.47)-(4.48) using numerical techniques. To illustrate the model we will analytically solve the case of zero ripple amplitude, i.e. $\delta = 0$. The set of equations (4.33)-(4.35) then simplifies to

$$
\begin{cases}
\alpha_3 C_o = \dfrac{1}{2}\alpha_3 C_1 \sin\theta \\[2ex]
C_1(1-\alpha_2) + \alpha_3 C_o \sin\theta = K\alpha_3 \cos\theta \\[2ex]
\alpha_1 C_1 - \alpha_3 C_o \cos\theta = K\alpha_3 \sin\theta
\end{cases}
\tag{4.49}
$$

from which one can obtain the amplitudes of C_o, C_1 and θ as a function of the ripple amplitude δ, the wavenumber of the ripple K, the driver strength F and the detuning ratio β:

$$
C_o = \frac{K\alpha_1\alpha_3^2}{2\alpha_2\left[\alpha_1^2 + (1-\alpha_2)^2 + \alpha_3^2(1-\alpha_2)\right]}
\tag{4.50}
$$

$$
C_1^2 = -\frac{2\alpha_2 C_o\left[C_o^2 + K^2\right]}{C_o(1-\alpha_2) - \alpha_1 K}
\tag{4.51}
$$

$$
\sin\theta = \frac{2\alpha_2 C_o}{\alpha_3 C_1}
\tag{4.52}
$$

From Eq.(4.46) we see that G = 0 for $\delta = 0$ and hence Eq.(4.47) reduces to

103

$$\left[2\left(\alpha_2 - \frac{1}{4}\right)\right]^2 + \alpha_1^2 = \alpha_3^2 \qquad (4.53)$$

Using Eq.(4.28) we finally obtain

$$\frac{\omega_p}{\Delta\omega} = \Gamma^{3/2}\left[\frac{1}{4} \pm \frac{1}{2}\left\{\left(\frac{F}{\Gamma^4}\right)^2 - \left(\frac{\alpha}{\Gamma^2}\right)^2\right\}^{1/2}\right]^{1/2} \qquad (4.54)$$

which describes the boundary of the parameter region for which the steady state solution of the oscillator is unstable to half-harmonic perturbations. Here, from Eq.(4.26), $\Gamma = (1 - 2F)^{-1/2}$. The boundary of this unstable region is shown in Fig.(4.8). Also, the half-harmonic resonance is consistent with the discontinuous first bifurcation (e.g. Fig.(4.4).
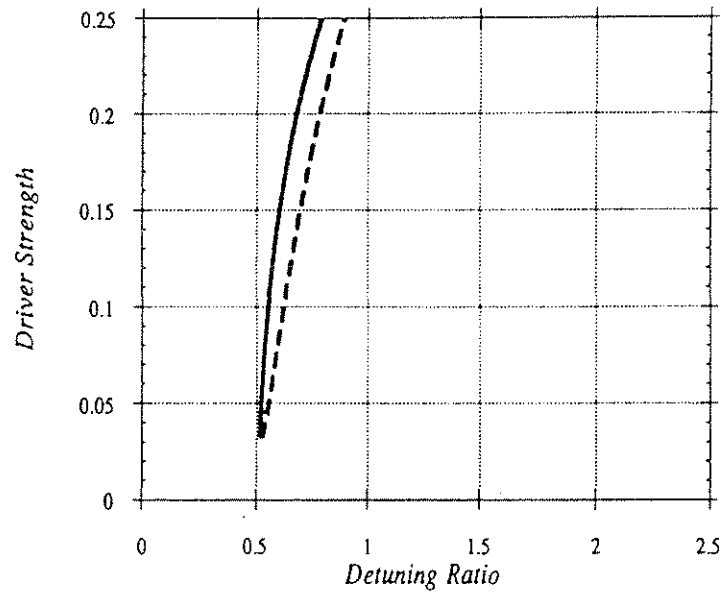

Figure 4.8.: Analytically calculated region in parameter space for which the Lagrangean oscillator equation, in the absence of a ripple, is unstable to half-harmonic perturbations.

4.4 PIC-Code Results

The object of the particle in cell simulations was to verify (using at times scaled parameters) that a period doubling (and if possible a route to chaos) can occur in the generation of relativistic plasma waves through collinear optical mixing even when competing effects are included.

In the simulations, the laser is incident from the left along the x-axis and is polarized along z. To reduce the amount of computing time we have kept the ions imobile. To model the density ripple the electrons and fixed ion background were initialized at time t = 0 with a sinusoidal ripple.

Frequencies are normalized to the background (excluding the ripple) plasma frequency ω_{p0}. Distances are normalized to the collisionless skin depth c/ω_{p0}. For display purposes the wavenumbers are given in units of "mode number", the number of wavelengths of a given sinusoidal mode that will fit within the simulation box: kx(m.n.) = $kL/2\pi$ where L is the length of the box, in this case 210 c/ω_{p0}, chosen to accomodate 20 waves with wavelength $2\pi/\Delta k$.

Three different simulations have been performed: a) rippled ion background at t = 0, b) no density ripple at t = 0 but with plasma temperature low enough so that the short wavelength plasma modes produced through SRS are not Landau damped and hence will produce a rippled plasma, and c) no density ripple at t = 0 and high plasma temperature so that the short wavelength plasma modes are Landau damped. We have chosen to use parameters in the PIC-simulation which have shown one bifurcation in the analytic model. The plasma frequency is equal to one in simulation units while the two laser frequencies are chosen to give a detuning ratio $\dfrac{\omega_p}{\Delta\omega}$ = 1.7: ω_1 = 5 and ω_2 = 4.411 in

ω_p units. In simulation units the dispersion relation for light waves in a plasma is given by

$$\omega^2_{1,2}= 1 + k^2_{1,2} \qquad\qquad (4.55)$$

The chosen laser frequencies give a plasma wave number $\Delta k = (24)^{1/2} - [(4.411)^2 - 1]^{1/2} = 0.602$. The ripple wavenumber is taken to be $\dfrac{k_i}{\Delta k} = 30$ and the ripple size $\varepsilon = 0.2$. The peak laser intensity results in a normalized quiver velocity $\dfrac{v_{osc}}{c} = 0.6$. The simulations were carried out in an essentially one-dimensional system on a 2 x 6000 grid of normalized dimension 1 x 210 (in c/ω_p units). This implies that the system can contain 20 plasma wavelengths oscillating at the beat frequency. A total of 120000 particles were used (10 particles per cell). The simulation was set up to record plasma parameters every $\Delta(\omega_p T) = 25$ (every 1000 time steps) except for the ω- spectrum which was recorded every 2000 time steps.

4.4.1 Observation of Half Harmonic

The main diagnostic consists of the k-spectrum of the transverse electric (E_z) field. Indeed, if spatial period doubling occurs in conjunction with temporal period doubling of the kind observed in the Lagrangean fluid model, the phase matching condition is satisfied for the laser frequencies to scatter from these subharmonics of the plasma wave. The k- spectrum of the transverse field should show Stokes and anti-Stokes lines of the laser frequencies which are shifted by subharmonics of the beat frequency.

At T = 0 the simulation was initialized with the above parameters. At T = 150, as shown in Fig.(4.9), the k-spectrum of the transverse electric field E_z contains Stokes and anti-Stokes lines shifted by subharmonics of the beat frequency. Since these

features will only show up in the electromagnetic spectrum when the phase matching conditions are met, this implies that temporal period doubling is coupled to spatial period doubling.
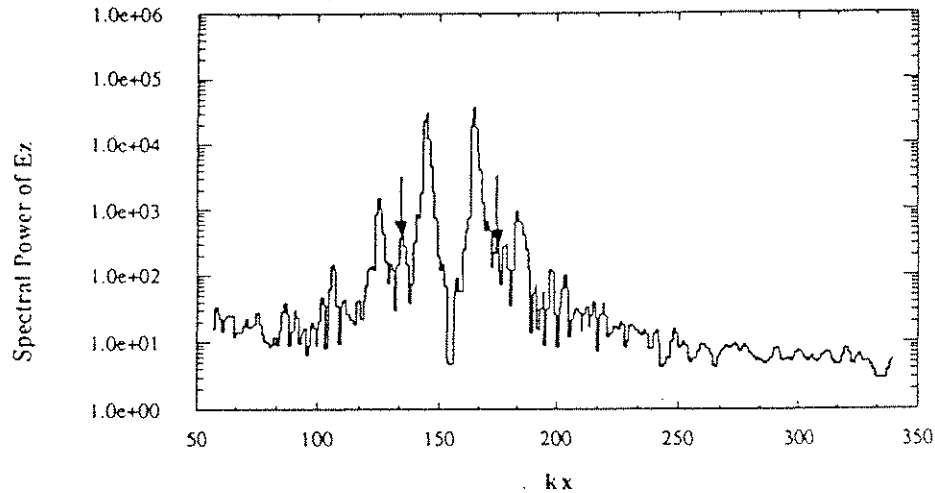
Figure 4.9: k-spectrum of the transverse electric field as obtained fromWAVE-simulation code at time step T= 150. The arrows denote the location of the half-harmonics.

4.4.2 Necessity of Short Wavelength Density Modulations

In the numerical model we have found that a range existed for density modulation wavelengths: $\frac{k_i}{\Delta k}$ had to be between 15 and 130 to observe period doubling. For the simulation parameters, plasma waves produced through Raman scattering or ion waves produced through SBS or the ion acoustic decay instability would result in density modulation with wavenumber ratio between 2 and 10. In order to verify that the observed subharmonics are caused by the short wavelength density modulations due to

107

the imposed ion ripple we have performed two null tests. While in both tests the initial ripple is absent, the thermal electron velocity at T = 0 was set equal to 0.025 c in the first test while in the second test it was set to 0.15 c. This higher plasma temperature resulted in Landau damping of the slow phase velocity plasma waves and no period doubling was observed. While SRS did modulate the density in the lower temperature case, the k was too low and no period doubling was observed here consistent with the analytic results.

4.5 Conclusion

A numerical study has been performed of the non-linear dynamics of the generation of a plasma wave through colinear optical mixing in a spatially and temporally modulated plasma. The numerical study was based upon the Lagrangean equation of motion for a fluid element moving under the influence of an intense laser pulse in the presence of an ion density modulation. The choice for working in a Lagrangean frame arose from the need to rigorously treat the relativistic mass increase of the fluid electrons for large laser intensities. It was shown that resorting to the weakly relativistic approximation in an Eulerian frame leads to the erroneous conclusion that beat-excitation of plasma waves can be modelled with a Duffing equation. The two non-linear phenomena on which we have concentrated are bistability with the associated hysteresis loops, and period doubling with the possibility of evolving into chaos. The parameters which determine the amplitude of the plasma wave were chosen to be the laser intensity, the plasma density, the damping rate, the wavelength and amplitude of the density modulation.

The obtained model-equation was solved numerically because the commonly used slowly varying amplitude approximation precludes one from observing subharmonics in the frequency spectrum of the wave amplitude. We find that in the absence of a density modulation, when the laser intensity or the plasma density is varied in time, the amplitude of the plasma wave as a function of either of these parameters shows hysteresis loops. A regime in which the motion of the fluid element would show spectral components at subharmonic frequencies of the driver frequency was not found. However, the presence of a short wavelength density modulation (spatial frequency typically more than 15 times the spatial frequency of the driver) considerably altered the behavior of the fluid element. In certain regions of parameter space it was found when sweeping the laser intensity in time two distinct regions exist: a) for relatively low amplitude density modulations the fluid element undergoes bifurcations leading to subharmonics in the spectrum followed by inverse bifurcations leading to a regular periodic motion oscillating at the driver frequency; b) for large density modulations a cascade of bifurcations occurred followed by a transition to chaos and consecutive periodic windows. Through stroboscopic sampling of the displacement and velocity of the fluid element the associated bifurcation trees and Poincare maps were generated. It was observed that the first bifurcation is discontinuous, followed by a period doubling route which seems closer to the classical route.

By following many Lagrangean oscillators simultaneously it is found that wavebreaking occurs before the second period doubling, thereby limiting the validity of the Lagrangean oscillator model. The origin of the first bifurcation is linked to the stability of an equivalent generalized Mathieu equation to $1/2$ subharmonic resonances.

Fully relativistic PIC-code simulations were carried out to further investigate the bifurcation behavior Through analysis of the k-spectrum of the transverse electric field E_z and magnetic field B_y it was found that spectral components exist at half the spatial

driver-frequency. Since these features will only show up in the electromagnetic spectrum when the phase matching conditions are met, we concluded that spatial period doubling must occur in conjunction with temporal period doubling. It needs to be mentioned however that for these simulations a very extensive amount of computer time was needed and that the ions had to be kept immobile. Future work should address the issue of self-consistent density modulation caused by finite mass ions and the resulting competition between this possible path to turbulence and phenomena such as Langmuir collapse.

Chapter 5

Conclusion

In this dissertation we have studied the interaction of a high power CO_2 - laser with preformed and tunnel-ionized plasmas. In the preformed plasma we have carried out experiments designed to isolate the stimulated Compton scattering instability. We have made the first detailed spectral measurements of stimulated Compton scattering from a pre-formed plasma using spectrally and temporally resolved Thomson scattering. For low density, the observed density fluctuation spectra were seen to convectively saturate. For higher density, an initially narrow spectrum was seen to saturate and evolve into broadband Compton scattering with frequency shifts once again near kv_e. Using the code WAVE as a guide, we suggested that the saturation is due to a reflectivity-induced modification of the electron distribution function. The implications of this work are that SCS can be a useful density and temperature diagnostic. The low reflectivity implies that this instability would not severly limit the coupling efficiency of laser power on to targets in laser-fusion experiments.

Through experiments and particle simulations we have then studied the plasma physics aspects of tunnel-ionized gases. Many experiments have been done using 1 μm lasers to understand the details of the process of optical induced ionization of single atoms and molecules. Using a 10.6 μm laser we have looked at the how the ionization physics would determine the plasma characteristics of macroscopic plasmas produced through tunneling ionization. The main predictions of the single particle tunneling

111

model are: (a) the tunneling ionization process generates odd harmonics of the laser frequency propagating in the direction of the laser; (b) fully ionized high density plasmas can be produced with temperatures that are controllable by varying the polarization of the laser and (c) the longitudinal temperature of the plasmas are much smaller than the transverse temperatures.

Experimentally both odd and even harmonics were observed. The measured level of the odd harmonics was found to be consistent with the theoretically expected value from the tunneling ionization model. By varying the laser polarization from linear to circular the odd harmonic emission was suppressed. However, the second harmonic was found to be polarization independent. It is believed to be generated through the steep radial density gradients of the tunnel ionization produced plasma.

The evolution of the plasma density and longitudinal temperature was measured using Thomson scattering of driven SCS fluctuations. In contrast to the predictions of the single particle tunneling model that high density plasmas can be produced with $T_{||} \ll$ 1 eV, the spectra of SCS induced fluctuations indicated that, at the time the SCS fluctuations have grown enough to become detectable, the longitudinal temperature was typically 75 eV and seemed to further increase with time. Furthermore instead of obtaining fully ionized plasmas, we found that the plasma densities were clamped below $\approx 10^{-3} \, n_c$.

As an independent density diagnostic we tried to resonantly excite a plasma wave using a two frequency CO_2 - laser beam. Only for a line pair requiring a resonant density less than $10^{-3} \, n_c$ were we able to drive a beat wave in this tunnel-ionized plasma, as witnessed by a SBS mode-coupled feature in the Thomson scattering data. This indicated again that the density was clamped to a lower than expected level. We then looked into the possibility of density clamping through ionization induced refraction. Experimentally we found that strong refraction of the laser beam occurred for fill

112

pressures corresponding to fully ionized plasma densities higher than 10^{-3} n_c. By incorporating concepts from the paraxial ray approximation into Gaussian optics we derived a scaling law for density clamping due to refraction, which was verified by self-consistent particle-in-cell simulations using WAVE.

To obtain an independent estimate of the plasma temperature and to explore the possibility of plasma temperature control through polarization of the ionizing laser light, soft X-ray emission above 800 eV was measured. The inferred temperatures were 450 ± 150 eV (180 ± 50 eV) for plasmas produced though a circularly (linearly) polarized laser beam. These temperatures are within a factor of two with what might be expected from a laser beam which has it's intensity clamped close to the ionization threshold due to refraction. To further verify the hypothesis of temperature control, we looked at SCS spectra for different ellipticities α of the polarization. It was found that for $\alpha > 0.6$ all high frequency electron fluctuations were suppressed. These observations are consistent with an increase in $T_\parallel$ in going from linear to circularly polarized light. However, the inferred values for $T_\parallel$ were still anomalously higher than the single-particle predictions.

The origin of the initial $T_\parallel$ and its further increase with time was studied through simulations. In the single particle regime ($n/n_c = 10^{-8}$) the code reproduced the same ring shaped electron drift velocity distributions as calculated from the tunneling model. For densities high enough for space charge effects to become important, 1-D simulations showed SRS to grow to large levels consistent with a low $T_\parallel$. In 2-D however SRS was suppressed because $T_\parallel$ at the end of the ionization phase was already large. Instead SCS occurred at a reduced level, consistent with experimental observations. We then put forward the idea of stochastic heating in these space-charge dominated plasmas to explain the large intial $T_\parallel$. 2-D simulations of space-charge dominated plasmas indeed

113

showed that, at the end of the ionization phase and after the laser pulse was gone, the transverse distribution functions were much more smeared out and $T_\parallel$ much higher.

To explain the further increase with time of $T_\parallel$ we considered the effect of the isotropization of the tranverse distributions through the Weibel instability and found that this effect could indeed account for our experimental observations.

Both the fact that the density is clamped due to refraction and the measured high plasma temperature could have significant implications for X-ray recombination laser schemes. However the scaling of our long wavelength laser parameters towards shorter wavelength lasers is not straightforward and needs to be looked into.

The possibility of exciting plasma waves in a plasma which has a time varying density and could have short scale length density modulations, led to a study of the non-linear dynamics of such waves. We numerically solved a relativistic Lagrangean oscillator equation which contained the essentail physics involved in the beat excitation process. The free parameters in this model were the amplitude and wavelength of the density modulation, the ponderomotive strength, the ratio of plasma frequency to beat frequency and a damping rate. A variety of non-linear phenomena were observed such as bistability and period doubling bifurcations in certain regions of parameter space. The phenomenon of wave breaking was found to invalidate the Lagrangean oscillator model beyond the first bifurcation but PIC-code simulations confirmed the possibility of the plasma wave to undergo a first bifurcation.

In future experiments with the CO_2-laser many aspects of the tunneling ionization of gases still remain to be studied. The main improvement in the experiments will come from the possibility of producing much higher densities. In fact gas-jet experiments are currently underway. Although we did attempt to measure thermal

spectra in the experiment, the low plasma density and the limited probe beam power precluded us from observing scattering from thermal fluctuations. At the higher plasma densities the light level in the themal spectra could possibly increase by two orders of magnitude. Since many of the experimentally studied phenomena depend on the detailed shape and evolution of the electron distribution functions, a simultaneous measurement of the Thomson scattering spectra from fluctuations driven through parametric instabilities and from thermal fluctuations could address the following issues:

* the self-induced modification of the longitudinal distribution function through the stimulated Compton scattering instability,

* the effects of a large quiver velocity on the thermal Thomson spectra,

* a direct measurement of the time evolution of the transverse and the longitudinal distribution functions and their dependence on laser polarization.

The higher plasma densities would also permit one to measure the rate of ionization by looking at the blue shifting of a probe beam due to a time varying plasma density (Wood 1988).

Harmonic generation due to $\chi^{(3)}$ could possibly increase many orders of magnitude since both the density and length of the gas medium can be optimized to get a higher efficiency. This could then allow one to look at the non-linear optical properties of atomic and molecular gases and verify if the excitation of atomic and molecular transitions could exhibit chaotic behavior and lead to supercontinuum generation (Alfano & Shapiro 1970a,b). The idea here is that, when molecules are excited by an intense laser, the displacement of the nuclei can become large enough for anharmonic terms to become important. The potential associated with this restoring force can be modelled as a Morse potential (Herzberg 1967) which can be reduced to a Duffing-like equation.

Finally, lasers able to generate ultra-high intensities ($v_{osc}/c \sim 0.5$) required for the experimental observation of subharmonic generation in the beatwave experiments already exist in several laboratories around the world. The more difficult condition to meet in order to see a period doubling cascade followed by chaos is not the intensity of the e.m.-waves but the large amplitude of the density modulation. If indeed the electron plasma wave can follow this route to turbulence, it could be an alternative for the well known theoretical Langmuir collapse scenario (Goldman 1984).

Appendix A

Experimental Set-Up

A.1 CO_2 -Laser System.

The CO_2 laser system is shown in Fig. A.1. The laser oscillator has a high pressure section (p = 24 psi) and a low pressure section (p = 50 Torr). This hybrid configuration allows control of the longitudinal modes on which the laser will oscillate. The laser can oscillate on different wavelengths (10.6μm, 10.3 μm and 9.6 μm) which are controlled (a) by moving the rear mirror with a piezo electric crystal to tune the cavity length and (b) by using an intra-cavity absorber cell. The output of the master oscillator is a 150 ns long pulse with a peak power of 1 MW. The pulse is shortened to about 70 ps using the free-induction technique. The key components here are (a) the atmospheric pressure sparker which chops off the back part of the pulse and (b) a tripple pased hot CO_2 absorber cell which absorbs the front part of the pulse, leaving a 70 ps short pulse with roughly the same peak power as the long pulse. The pulse passes then through a pre-amplifier followed by tripple passing a high pressure (24 psi), large aperture amplifier from here on refered to as the MARS laser. The output pulse has a rise time of 150 ps and a fall time of 350 ps and contains up to 100 J. The focusing optic is an f-10 off-axis parabola. The final spot size is about 340 μm diameter.

117

A.2 Thomson Scattering System.

The Thomson scattering equipment uses a frequency-doubled YAG laser at a wavelength of 532 nm which puts out about 170 mJ contained in a main pulse of 5 ns. The beam is focused onto the plasma using f-20 optics. The k-matching angle for diagnosing the 2 k_0 fluctuations driven by the CO_2 - laser is 6°. The scattered signal is spectrally resolved in a 64 cm spectrograph using a holographic 1800 grooves/mm grating, and time resolved with an IMACON 500 optical streak camera. The streak image is captured using a low noise cooled CCD-camera (576 x 384 pixels) and sent to a PC for image analysis. The spectral resolution is 0.2 Å/pixel and the temporal resolution is 2.5 ps/pixel. The synchronization of the YAG laser and the short pulse CO_2 pulse was done as follows: using a beam splitter at the exit plane of the hot CO_2 - cell, a small amount of the short pulse was sent to a room temperature Hg-Cd-Te detector (RADEC detector). The RADEC sent out an electrical pulse (200 mV peak) which was amplified with a low jitter (<100 ps) avalanche amplifier to 35 V and split into 4 channels. One of those channels triggered the Marx bank of the YAG laser Q-switch and two of the other channels where used to trigger the streak cameras. The final jitter was measured to be around 200 ps.
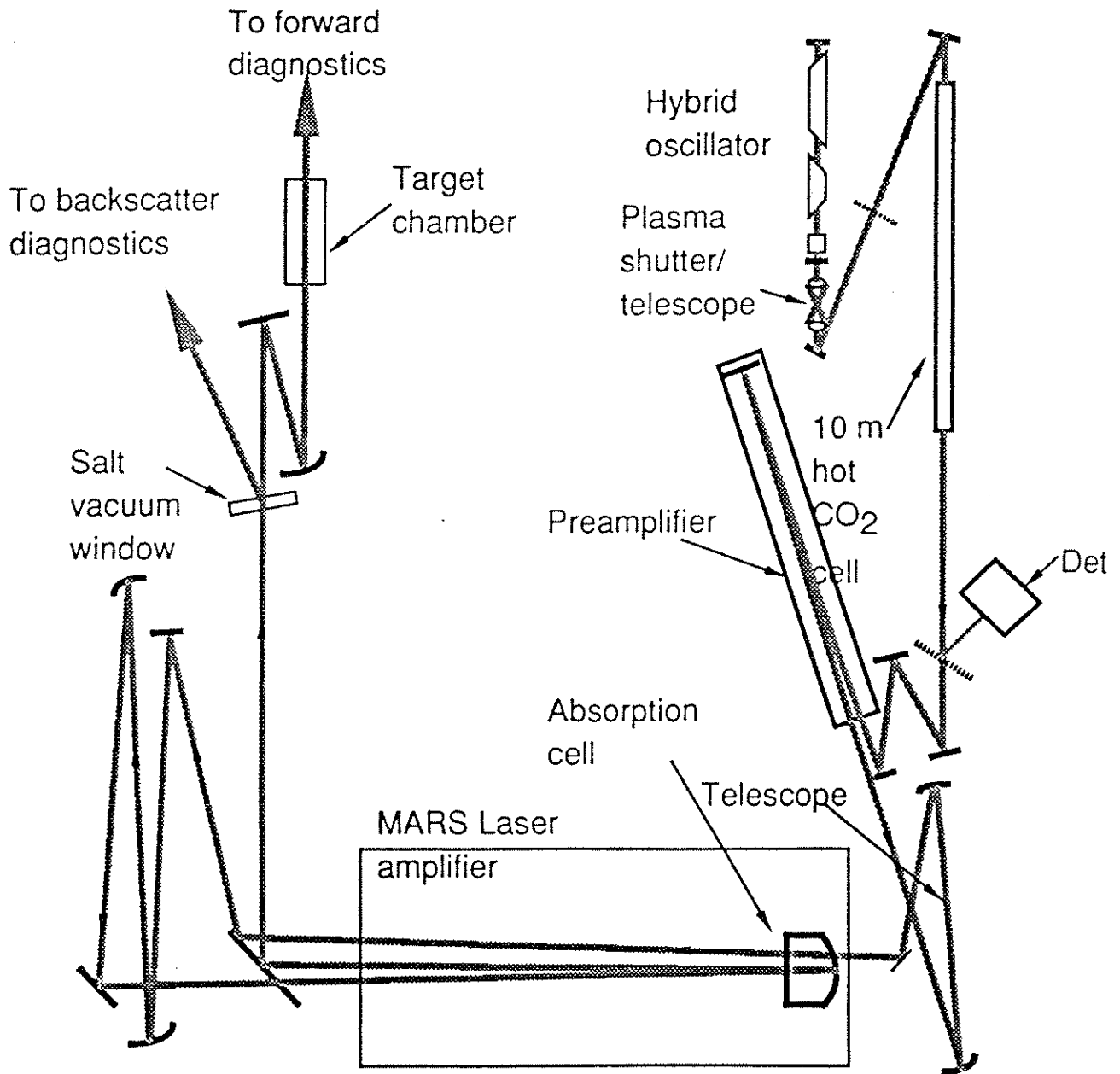
Figure A.1: CO_2 - laser system

Appendix B

Fluid Equations in an Ionizing Plasma

We start from the Vlasov equation for a one-particle distribution function to which a source term, $S(r,p,t)$, has been added to model the time varying plasma density, and the relativistic equation of motion of an electron:

$$\frac{\partial f}{\partial t} + \frac{p}{\gamma\, m_0} \cdot \frac{\partial f}{\partial r} + q\, (E + \frac{p\, x\, B}{\gamma\, m_0\, c})\cdot \frac{\partial f}{\partial p} = S(r,p,t) \qquad (B.1)$$

$$\dot{p} = q\, [\, E + \frac{v\, x\, B}{c}\,] = \frac{d}{dt}\,(m_0\gamma v) \qquad (B.2)$$

$$\dot{r} = v\, ,\quad v = \frac{p}{\gamma m_0}\, . \qquad (B.3)$$

where m_0 and q are respectively the rest mass and charge of an electron, γ is the Lorentz factor, f is the one particle distribution function, and E and B are the electric and magnetic field

Furthermore we assume the plasma to be perfectly cold , i.e.

$$f(r,p,t) = \bar{f}(r,t)\, \delta\, (p - P) \text{ where } P = P(r,t). \qquad (B.4)$$

To obtain fluid equations we take moments of Eq. (B.1).

The mean density and velocity are respectively defined as:

$$n = \int_{-\infty}^{+\infty} d^3p\ \ f \qquad (B.5)$$

and

$$v = \frac{1}{n} \int_{-\infty}^{+\infty} d^3p \frac{f(r,p,t)}{m_0\gamma} \tag{B.6}$$

Taking the zero[th] order moment and using Eqs. (B.5) and (B.6) we obtain the usual continuity equation with the inclusion of a source term:

$$\frac{\partial n(r,t)}{\partial t} + \nabla \cdot [\ n(r,t) \frac{P}{m_0\gamma}\ ] = \lambda\ n(r,t) \tag{B.7}$$

Taking the first order moment we find:

$$\frac{\partial}{\partial t} [\ P(r,t)\ n(r,t)\ ] + \frac{\partial}{\partial r} [\ \frac{P^2(r,t)}{\gamma\ m_0}\ n(r,t)] - q\ [\ E + \frac{p\ x\ B}{\gamma\ m_0 c}\ ]\ n(r,t) = 0 \tag{B.8}$$

But the first term in Eq. (B.8) can be written out as

$$\frac{\partial}{\partial t} [\ P\ n\ ] = n \frac{\partial P}{\partial t} + P \frac{\partial n}{\partial t} \tag{B.9}$$

Multiplying Eq. (B.7) by P and subtracting it from Eq. (B.8) we obtain as equation of motion:

$$\frac{\partial}{\partial t} [\ P(r,t)\ ] + v \frac{\partial P(r,t)}{\partial r} - q\ [\ E + \frac{p\ x\ B}{\gamma\ m_0 c}\ ]\ + \lambda\ P(r,t) = 0 \tag{B.10}$$

where we used the definitions of $\dot{r}$ and v given in Eq. (B.3).

Appendix C

Eulerian Analysis of Large Amplitude Relativistic Plasma Waves

We re-examine the consequences of making the weakly relativistic approximation when investigating chaotic solutions. We rederive an equation of motion for the longitudinal electric field using this weakly relativistic approximation and then make the connection with the well known Duffing equation (Duffing 1918) for a non-relativistic particle moving inside a potential well $V(\Psi) = \frac{\Psi 2}{2} - \frac{\Psi 4}{4}$, where Ψ is the amplitude of the displacement. Using a rotating Van der Pol plane (Thompson & Stewart 1986) we calculate the steady state amplitude of the displacement as a function of driving strength and detuning ratio. The Duffing like equation is then solved numerically and the results compared to the analytically obtained frequency response function. The validity of the Duffing model is then assessed and it is found that this model can not be used to study the interesting regime of large driving strengths where the non-linear dynamics dominate the system behavior.

C.1 Eulerian Analysis of Electron Plasma Waves

Consider the fluid equations for a plasma in which the density is changing in time due to collisional ionization at a rate λ. The equation of continuity and the equation of motion for a fluid element are respectively given by

$$\frac{\partial n(r,t)}{\partial t} + \nabla \cdot [\, n(r,t) \frac{P}{m_0 \gamma}\,] = \lambda \, n(r,t) \tag{C.1}$$

and

$$\frac{\partial}{\partial t} [\, P(r,t)\,] + v \frac{\partial P(r,t)}{\partial r} - q [\, E + \frac{p \times B}{\gamma \, m_0 c}\,] \, n(r,t) + \lambda \, P(r,t) = 0 \tag{C.2}.$$

The two fluid equations (C.1) and (C.2), complemented by the Maxwell's equations

$$\nabla \cdot E = -4\pi e \, (n_e - n_i) \tag{C.3}$$

$$\nabla \times B = \frac{1}{c} \frac{\partial E}{\partial t} - \frac{4\pi e}{c} (n_e v_e - n_i v_i) \tag{C.4}$$

$$\nabla \times E = -\frac{1}{c} \frac{\partial B}{\partial t} \tag{C.5}$$

are used to derive the equation which describes the evolution of the longitudinal electric field generated by beating two transverse linearly polarized electromagnetic waves in a plasma. In these equations n_e (n_i)and v_e (v_i) are the electron (ion) fluid density and velocity, p_e is the electron fluid momentum and all other quantities have their usual meaning.

Let us assume that the ions are immobile and analyze the set of equations in an Eulerian coordinate system. Combining equations (C.4) and (C.5) we obtain:

$$(\nabla^2 - \frac{1}{c^2} \frac{\partial^2}{\partial t^2} - \nabla\nabla \cdot) \, E = -\frac{4\pi e}{c^2} \frac{\partial}{\partial t} (N_e v_e) \tag{C.6}$$

We now define $N_e = N_0 + n_e$, where N_0 is a background steady state value and n_e is oscillatory. Equation (C.6) becomes

$$(\nabla^2 - \frac{1}{c^2} \frac{\partial^2}{\partial t^2} - \nabla\nabla \cdot) \, E = -\frac{4\pi e}{c^2} (N_0 \frac{\partial}{\partial t} v_e + \frac{\partial}{\partial t} (n_e v_e)) \tag{C.7}$$

From the equation of motion we obtain

$$\frac{\partial v_e}{\partial t} + v_e \cdot \nabla v_e = -\frac{e}{\gamma m_o} (\underline{\underline{I}} - \frac{v_e v_e}{c^2}) (E + \frac{v_e \times B}{c} - \lambda \gamma m_o v_e) \qquad (C.8)$$

where $\underline{\underline{I}}$ is the unit tensor.

Substituting equation (C.8) into equation (C.7) we find

$$(\nabla^2 - \frac{1}{c^2}\frac{\partial^2}{\partial t^2} - \nabla\nabla .) E = -\frac{4\pi e}{c^2} \{\frac{\partial}{\partial t}(n_e v_e) - N_0 v_e \cdot \nabla v_e -$$

$$\frac{N_{oj} e}{\gamma m_o} (\underline{\underline{I}} - \frac{v_e v_e}{c^2}) (E + \frac{v_e \times B}{c} - v \gamma m_o v_e) \} \qquad (C.9)$$

For the weakly relativistic case we expand γ^{-1}:

$$\gamma^{-1} = \sqrt{1 - (\frac{v}{c})^2} \approx 1 - \frac{1}{2}(\frac{v}{c})^2 \qquad (C.10)$$

The wave equation becomes

$$(\nabla^2 - \frac{1}{c^2}\frac{\partial^2}{\partial t^2} - \nabla\nabla .) E = -\frac{4\pi e}{c^2} \{\frac{\partial}{\partial t}(n_e v_e) - N_0 v_e \cdot \nabla v_e -$$

$$\frac{N_0 e}{\gamma m_o} \{ [(\underline{\underline{I}} - \frac{v_e v_e}{c^2})\frac{1}{2}(\frac{v}{c})^2 + \frac{v_e v_e}{c^2}] \cdot E - (1 - (\frac{v}{c})^2 \frac{v_e \times B}{c} \} +$$

$$\lambda N_0 e (\underline{\underline{I}} - \frac{v_e v_e}{c^2}v_e) \} \qquad (C.11)$$

The evolution of the longitudinal component of the electric field is then determined by

$$\{ \frac{\partial^2}{\partial t^2} + \omega_p^2 [1 - \frac{3}{2}(\frac{v_x}{c})^2 - \frac{1}{2}(\frac{v_z}{c})^2] \} E_x = 4\pi e \{ \frac{\partial}{\partial t}(n_e v_{ex}) -$$

$$N_0 v_e \cdot \nabla v_{ex} + \frac{N_0 e}{\gamma m_o} \frac{v_x v_z}{c^2} E_z - \frac{N_0 e}{\gamma m_o}(\frac{v_e \times B}{c})_x +$$

$$\lambda N_0 e v_{ex} (1 - \frac{v_x^2 + v_z^2}{c^2}) \} \qquad (C.12)$$

Following Mori's work (Mori 1987) we use the Mitropolsky-Bogoliubov perturbation technique to obtain an equation of motion for the longitudinal electric field value. The wave equation becomes:

124

$$\left\{\frac{\partial^2}{\partial t^2} + \left[\sigma + \lambda\left[1 - \frac{1}{4}\left(\frac{v_\phi}{c}\right)^2 |e_0|^2 - \frac{1}{2}(\alpha_1^2 + \alpha_2^2)\right]\right]\frac{\partial}{\partial t} + \right.$$

$$\left. \omega_p^2\left[1 - \frac{3}{8}\left(\frac{v_\phi}{c}\right)^2 |e_0|^2 - \frac{1}{4}(\alpha_1^2 + \alpha_2^2)\right]\right\} \mathcal{E}_0 =$$

$$\frac{c}{v_\phi}\frac{\alpha_1 + \alpha_2}{2}\omega_p^2 \sin(\Delta k\, x - \Delta\omega\tau) \qquad\qquad (C.13)$$

where v_ϕ is the phase velocity of the wave, $\alpha_i = \frac{v_{osc}}{c} = \frac{eE_i}{m\omega_i c}$ is the normalized non-relativistic oscillatory velocity of the electron in the laser field and σ is a phenomenological damping term to accommodate for such effects as mode coupling to slow waves. Equation (C.13) can be rewritten as :

$$\frac{\partial^2\Psi}{\partial t^2} + (c_1 + c_2 |\Psi|^2)\frac{\partial\Psi}{\partial t} + (c_3 + c_4 |\Psi|^2)\Psi = F\sin(\Delta k - \Delta\omega\,\tau) \quad (C.14)$$

with

$$c_1 = \sigma + \lambda\left(1 - \frac{1}{2}(\alpha_1^2 + \alpha_2^2)\right)$$

$$c_2 = -\lambda\frac{1}{4}\left(\frac{v_\phi}{c}\right)^2$$

$$c_3 = \omega_p^2\left[1 - \frac{1}{4}(\alpha_1^2 + \alpha_2^2)\right]$$

$$c_4 = \omega_p^2\left[\frac{3}{8}\left(\frac{v_\phi}{c}\right)^2 |e_0|^2\right]$$

Under this form one recognizes the equation of a driven oscillator with both non-linear damping (a Van der Pol type oscillator) and non-linear spring constant (a Duffing type oscillator). In the next section we focus on the case in which $\sigma \gg \lambda$, i.e. the Duffing oscillator.

C.2 Duffing Model of Electron Plasma Waves

It is well known that the Duffing equation exhibits the jump phenomenon and that a period doubling route to chaos can exist (Holmes & Rand 1976, Huberman & Crutchfield 1979). In order to verify that these same phenomena can be observed for large amplitude relativistic plasma waves in an actual collinear optical mixing experiment, we need to establish a parameter regime which is accessible in the laboratory. Therefore it is necessary to develop an understanding of the parameter space and fundamental characteristics of the canonical Duffing equation. Furthermore we have to ascertain that the aforementioned effects occur for weakly relativistic waves, as assumed in our derivation of the equation of motion, and for wave amplitudes less than the wave breaking limit.

In what follows we assume that the fluid element excursion is small compared to the beat-wave wavelength and apply a capacitor model for the driver term. The beat-wave equation can then be written under the standard Duffing form with a cosinusoidal driver term :

$$\frac{d^2\Psi}{dt^2} + \Gamma \frac{d\Psi}{dt} + \alpha \, \omega_p^2 \, \Psi + \beta \, \omega_p^2 \, \Psi^3 = F \cos \Omega t \qquad (C.15)$$

where all parameters are real and $\Gamma \equiv \sigma$. This equation models the motion of a particle with charge ω_p^2 moving in a potential of the form

$$V(\Psi) = \alpha \frac{\Psi^2}{2} + \beta \frac{\Psi^4}{4} \qquad (C.16)$$

The turning point of this potential is found from

$$\frac{dV}{d\Psi} = 0 \text{ or } \Psi_0 = \sqrt{\frac{-\alpha}{\beta}}$$

Renormalizing time with respect to $\sqrt{\alpha} \, \omega_p^2$ and space with respect to the turning point distance Ψ_0 we obtain

$$\frac{d^2\eta}{d\tau^2} + \Gamma \frac{d\eta}{d\tau} + \eta - 4\eta^3 = F \cos \omega\tau \qquad\qquad (C.17)$$

where $\eta = \dfrac{\Psi}{2\Psi_o}$ and $\tau = \omega_p t$.

We rewrite equation (C.17) as a set of first order non-linear differential equations where the position x_1, velocity x_2 and $\omega\tau$ are taken as the independent variables:

$$\overset{\circ}{x}_1 = x_2$$

$$\overset{\circ}{x}_2 = -x_1 + 4x_1^3 - \Gamma x_2 + F \cos \iota \qquad\qquad (C.18)$$

$$\overset{\circ}{\iota} = \Omega$$

where $|\lambda|$ is assumed small, $\lambda = (\Gamma, F, \rho)$; $\rho = 1 - \omega^2$ \qquad\qquad (C.19)

Let us first set F equal to zero so that equation (C.18) reduces to an autonomous equation. The fixed points are given by

$$x_{1s} = 0 , \ x_{2s} = 0 \ \text{and} \ x_{1s} = \pm \frac{1}{2} , \ x_{2s} = 0 \qquad\qquad (C.20).$$

Performing a local stability analysis it is straightforward to show that , for $\Gamma \geq 0$ the first fixed point is a sink while the two others are saddle points.

We now return to the non-autonomous equations: in case $|\lambda|$ small one can use the method of averaging to analyze the system.

Consider therefore a Van der Pol plane (z_1, z_2) rotating at the frequency ω (Thompson & Stewart 1986):

$$z_1 = x_1 \cos \omega\tau - \frac{x_2}{\omega} \sin \omega\tau$$

$$z_2 = -x_1 \sin \omega\tau - \frac{x_2}{\omega} \cos \omega\tau \qquad\qquad (C.21)$$

or equivalently

$$x_1 = z_1 \cos \omega\tau - z_2 \sin \omega\tau$$

$$x_2 = -\Omega [z_1 \sin \omega\tau + z_2 \cos \omega\tau] \tag{C.22}$$

Differentiating equation (C.21) with respect to time, substituting equations (C.18) and (C.22) and time averaging over one period, i.e $\tau = 0 \rightarrow \dfrac{2\pi}{\omega}$ results in

$$\overset{\circ}{z_1} = \frac{1}{2\omega} [-\rho\, z_2 - \Gamma\, \omega\, z_1 + 3\, z_2\, (z_1{}^2 + z_2{}^2)]$$

$$\overset{\circ}{z_2} = \frac{1}{2\omega} [\rho\, z_1 - \Gamma\, \omega\, z_2 - 3\, z_1\, (z_1{}^2 + z_2{}^2) - F] \tag{C.23}$$

Using a polar coordinate system

$$z_1 = r \cos\theta$$

$$z_2 = r \sin\theta \tag{C.24}$$

equation (C.23) becomes

$$\overset{\circ}{r} = \overset{\circ}{z_1} \cos\theta + \overset{\circ}{z_2} \sin\theta$$

$$= \frac{1}{2\Omega} (-\Gamma\, \omega\, r - F \sin\theta) \tag{C.25}$$

$$r\overset{\circ}{\theta} = -\overset{\circ}{z_1} \sin\theta + \overset{\circ}{z_2} \cos\theta$$

$$= \frac{1}{2\Omega} (\rho\, r + 3\, r^3 - F \cos\theta)$$

In order to find the steady state amplitude A and phase Φ of the oscillation we have to evaluate the fixed points of equations (C.25) :

$$\overset{\circ}{r} = 0 \quad \Rightarrow \quad F \sin\Phi = -\Gamma\, \omega\, A \tag{C.26}$$

$$r\overset{\circ}{\theta} = 0 \quad \Rightarrow \quad F \cos\Phi = \rho\, A - 3\, A^3$$

Therefore, the amplitude of the steady state oscillation is found from

$$A^6 + \frac{2}{3}\rho\, A^4 + \frac{1}{9} (\rho^2 + \Gamma^2\, \omega^2)\, A^2 - \frac{F^2}{9} = 0 \tag{C.27}.$$

and the phase with respect to the driver is given by

128

$$\tan \Phi = -\frac{\Gamma \omega}{\rho - 3 A^2} \tag{C.28}$$

The roots of this cubic polynomial in A^2 as a function of ω are plotted for $\Gamma = 0.4$ and F respectively equal to 0.10, 0.11, 0.12 in Fig.(C.1).

The upper branch is associated with a steady state motion around the points $x_1 = \pm\frac{1}{2}$ while the lower branch is associated with motion around the point $x_1 = 0$. As F increases for a given damping rate Γ we notice that the two branches connect allowing the steady state amplitude of a particle with equilibrium position around $x_1 = 0$ to build up to amplitudes close to the unstable points.

To study the detailed dynamics of the system, i.e. not just follow the motion of the particle with frequency equal to the driver frequency, we solved equation (C.22) using a fourth order Runge-Kutta methoC. As seen from Fig. C.1, for F=0.11, Γ=0.4 the two analytic steady state solution branches are not connected and in the numerical solution we did not observe any bistable behavior.

For larger driver strengths the two branches do connect and one is able to build up the amplitude of the oscillation to values close to the unstable limit. We observed period doubling when the amplitude of the displacement approached the turning point amplitude, for driver frequencies close to $\omega = 0.5$. To summarize, it is found that a hysterectic loop develops when the lower branch nearly touches the upper branch and that a period doubling route to chaos only develops when the branches are connected.
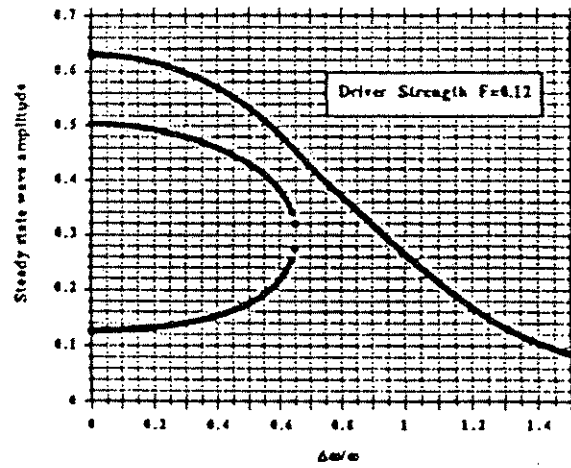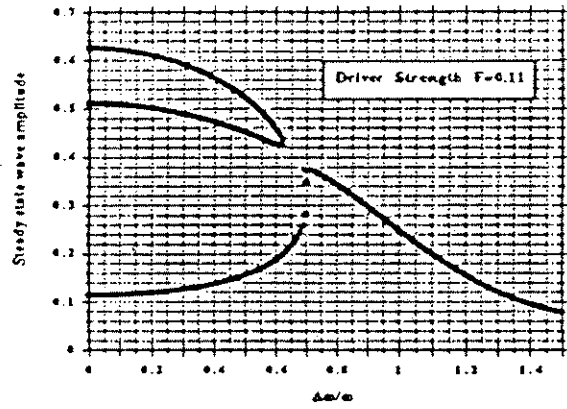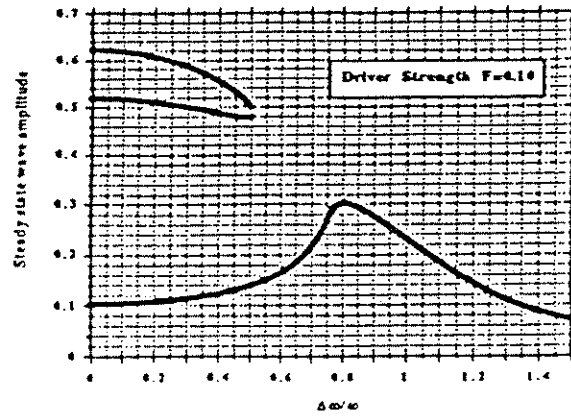
129

Figure C.1: Steady state amplitude versus frequency for driver strength F respectively 0.1, 0.11, 0.12 and damping $\Gamma=0.4$.

130

The amplitude associated with the onset of both phenomena is close to the turning point amplitude for this potential.

At this stage we will asses the validity of our model. The wave equation was derived in the weakly relativistic limit i.e. the Taylor expansion of the Lorentz factor was terminated after the second term. The resulting restoring force in the wave equation is then indeed equivalent to the restoring force for a softening spring. In a Lagrangean frame it is straightforward to show that the equation of motion in the absence of damping for the momentum of relativistic plasma waves is given in it simplest form by

$$\frac{d^2p}{dt^2} + \omega_p^2 \frac{p}{\sqrt{1 + p^2}} = \frac{d}{dt} F_{NL} \tag{C.29}$$

where F_{NL} is the ponderomotive force. The restoring force can now be derived from a potential

$$V(p) = \sqrt{1 + p^2} - 1 \tag{C.30}$$

In Fig. 4.1 we showed the exact potential as given by equation (C.29) and its Taylor expansion up to 2nd order. As can be seen from Fig.4.1, the two potentials start differing significantly beyond $|p| = 1$ and the dynamics associated with the two potentials is completely different : while the exact potential has only one stable equilibrium point, its Taylor expansion has one stable and two unstable equilibrium points. And, as seen from our previous analysis the period doubling occurs for amplitudes close to the unstable points.

To summarize, the rich non-linear behavior (i.e. period doubling route to chaos and bistability) exhibited by the Eulerian model-equation of the longitudinal electric field, is an artefact of the weakly relativistic approximation used in the derivation of equation (C.14).

131

References

Agostini, P. et al. 1979, *Phys. Rev. Lett.* **42**, 1127.

Akhiezer, A. I. & Polovin, R. V. 1956 *Sov. Phys. JETP* **3**, 696.

Albritton, J. R. 1975, *Phys. Fluids* **18**, 51.

Alfano, R. R. & Shapiro, S. L. 1970a, *Phys. Rev. Lett.* **24**, 584.

Alfano, R. R. & Shapiro, S. L. 1970b, *Phys. Rev. Lett.* **24**, 592.

Amendt, P. et al. 1991, *Phys. Rev. Lett.* **66**, 2589.

Amiranoff, F. 1991, private communication.

Bardsley, J. N. et al. 1989, *Phys. Rev. A* **40**, 3823.

Bernard, J. et al. 1989, *Phys. Rev. A* **39**, 2549.

Bier, M. & Bountis, C. 1984, *Phys. Lett.* **104A**, 239.

Brunel, F. 1990, *J. Opt. Soc. Am.* **7**, 521.

Burnett, N. H. & Corkum, P. B. 1989, *J. Opt. Soc. Am. B* **6**, 1195.

Burnett, N. H. & Enright G. D. 1990, *IEEE J. of Quantum Electronics* **26**, 1797.

Chen, F. F. 1984, *Introduction to Plasma Physics and Controlled Fusion*, 2nd edition, Plenum Press, New York.

Clayton, C. et al. 1985, *Phys. Rev Lett.* **54**, 2343.

Clayton, C. E. 1991, IEEE Trans. Plasma Sci., to be published.

Coffey, T. P. 1971, *Phys. Fluids* **14**, 1402.

Cohen, B. I. & Max, C. E. 1979, *Phys. Fluids* **30**, 1115.

Corkum, P. B. et al. 1989, *Phys. Rev Lett.* **62**, 1259.

Dangor, A. E. et al. 1985, *Laser Acceleration of Particles*, AIP Conf. Proc. No. 130 (Joshi, C. Katsouleas, T. Ed.) American Institute of Physics, New York.

Dangor, A. E. et al. 1987, *IEEE Trans. Plasma Sci.* **PS-2**, 161.

Darrow, C. B. et al. 1986, *Phys. Rev. Lett.* **56**, 2629.

Darrow, C. B. et al. 1987, *IEEE Trans Plasma Sci.* **PS-15**, 107-130.

Darrow, C. B. 1991, private communication.

Davidson, R. C. & Schram, P. C. 1968, *Nucl. Fusion* **8**,183.

Dawson, J. M. 1959, *Phys. Rev.* **113**, 383.

Downer, M. C. et al. 1990, *Phys. Rev. Lett.* **65**, 2832.

Drake, J. F. et al. 1974, *Phys. Fluids* **17**, 778.

Drake, R. P. et al. 1990, *Phys. Rev. Lett.* **64**, 423.

Duffing, G. 1918, *Erzwungene Schwingungen bei Veranderlicher Eigenfrequenz*. F. Vieweg u. Sohn: Braunschweig.

Estabrook, K. 1978, *Phys. Rev. Lett.* **41**, 1808.

Estabrook, K. et al. 1985, *Phys. Fluids* **28**, 19.

Feigenbaum, M. J. 1978, *J. Stat. Phys.* **19(1)**, 25.

Forslund, D.W. et al. 1975, *Phys. Fluids* **18**, 1002 and references therein.

Forslund, D. W. et al. 1985, *Phys. Rev. Lett.* **54**, 558.

Goldman, M. V. 1984, *Rev. Mod. Phys.* **56**, 709.

Hayashi, C. 1964, *Non-linear Oscillations in Physical Systems*, McGraw-Hill New York

Herzberg, G. 1967, *Molecular Spectra and Molecular Structure*, Prentice Hall New York.

Holmes, P. & Rand, D. 1976, *J. of Sound and Vibration* **44**, 237.

Horton, W., & Tajima, T. 1985, *Phys. Rev. A* **31**,3937.

Huberman, B. & Crutchfield, J. P. 1979, *Phys. Rev. Lett.* **43**, 1743.

133

Joshi, C. et al. 1984, *Nature (London)* **311**, 525.

Katsouleas, T. (Ed.) 1987, *IEEE Trans. on Plasma Science* **PS-15**, 192.

Katsouleas, T. & Mori, W. B. 1989, *Phys. Rev* **61**, 90.

Kaw, P. K. et al. 1973, *Phys. Fluids* **16**, 1522.

Kaw, P. K. & Kulsrud, R. M. 1973, *Phys. Fluids* **16**, 321.

Keldysh, L. V. 1965, *Sov. Phys. JETP* **20**, 1307.

Kitagawa, Y. et al. 1988 Conference on Lasers and Electro-Optics (CLEO), Anaheim, Ca., Technical Digest Series, 7, Optical Society of America, Washington, D. C..

Koch, P. & Albritton, J. 1974, *Phys. Rev. Letters* **32**, 1420.

Krall, N. A. & Trivelpiece, A. W. 1973, *Principles of Plasma Physics*, McGraw-Hill Book Company.

Kruer, W. L. & Dawson, J. M. 1970, *Phys. Rev. Lett.* **25**, 1174.

Kruer, W. 1972, *Phys. Fluids* **15**, 2423.

Landau, L. D. & Lifshitz, E. M. 1962, *The Classical Theory of Fields*, Pergamon Oxford.

Landau, L. D. & Lifshitz, E. M. 1978, *Quantum Mechanics* 3rd Ed., Pergamon London.

Leemans, W. P. et al. 1991a, *Phys. Rev. Lett.* to be published.

Leemans, W.P. et al. 1991b, *Proceedings of the Accelerator Conference*, San Francisco CA.

Leemans, W. P. et al 1991c, submitted to *Phys. Rev. Lett.* .

Lehmeier, H. J. et al. 1985, Optics Comm. **56**, 67.

l'Huillier, A. et al. 1983, *Phys. Rev. A.* **27**, 2503.

Lin, A. T. & Dawson, J. M. 1975, *Phys. Fluids* **18**, 201.

Litvak A. G. & Trakhtengerts, V. Yu. 1971, *Sov. Phys.–JETP* **33**, 921.

Ma, J. X. & Xu, Z. Z. 1989, *J. Appl. Phys.* **65** , 9.

Matte, J. P. & Martin, F. 1988, *Plasma Phys. and Controlled Fusion* **30**, 395.

Max, C. E. 1976, *Phys. Fluids* **19**, 74.

McKinstrie, C.J. & Forslund, D. W. 1987, *Phys. Fluids* **30**, 904.

Mendonça, J. T. 1983, *Phys. Rev. A* **28**, 3592.

Mendonça, J. T. 1985, *J. Plasma Physics* **34**, 115.

Meyer, J. & Zhu, Y. 1987, *Phys. Fluids* **30**, 890.

Moon, F. C. 1987, *Chaotic Vibrations*, J. Wiley & Sons.

Mori, W. B. 1987, *IEEE Trans-Plasma Sci.* **PS- 5(2)** 88-106 Appendix A.

Mori, W. B. 1987, *Ph. D. dissertation*, UCLA.

Mori, W. B. 1991, private communication.

Morse, R. L. & Nielson, C. W. 1971, *Phys. Fluids* **14**, 830.

Penetrante, B. M. & Bardsley J. N. 1991, *Phys. Rev. A* **43**, 3100.

Perry, M. D. et al. 1988, *Phys. Rev. Lett.* **60**, 1270.

Rose, H. A. et al. 1987, *Phys. Rev Lett.* **58**, 2547.

Rosenbluth, M. N. & Liu, C. S. 1972, *Phys. Rev. Lett.* **29**, 701.

Rosenbluth, M. N. 1972, *Phys. Rev. Lett.* **29**, 565.

Sheffield, J. 1975, *Plasma Scattering of Electromagnetic Radiation* (Academic Press, New York).

Shen, Y. R. 1984, *The Principles of Non-Linear Optics*, John Wiley & Sons.

Shkarofsky, I. P. et al. 1966, *The ParticleKinetics of the Plasmas*, Addison Wesley Pub. Co. .

Sprangle, P. et al. 1990, *Phys. Rev. A* **41**, 4463.

Szemplinska-Stupnicka, W. & Bajkowski, J. 1986, *Int. J. Non-Linear Mechanics* **21**, 401.

Tajima, T. & Dawson, J. M. 1979, *Phys. Rev. Lett.* **43**, 267.

Tang, C. M. et al. 1985, *Phys. Fluids* **28**, 1974.

Thompson, J. M. T. & Stewart, H. B. 1986, *Nonlinear Dynamics and Chaos*, J. Wiley & Sons Ltd.

Tripathi, V. K. & Pitale, L. A. 1977, *J. Appl. Phys.* **48**, 3288.

Yergeau, F. et al. 1987, *J. Phys. B. At. Mol. Phys.* **20**, 723.

Wallace, J. M. et al. 1991, *Phys. Fluids*, to be published.

Walsh, C. J. et al. 1984, *Phys. Rev. Lett.* **53**, 1445.

Ward, J. F. & New, G. H. C. 1969, *Phys. Rev.* **185**, 57.

Weber, M. J. (Ed.) 1982, *CRC Handbook of Laser Science and Technology*, CRC Press.

Weibel, E. S. 1959, *Phys. Rev. Lett.* **2**, 83.